Cycle-to-Cycle Variations in Dynamic Stall over a Pitching Airfoil

An Experimental Evaluation.

Master's Thesis

Martín Camus Amorós

Delft University of Technology

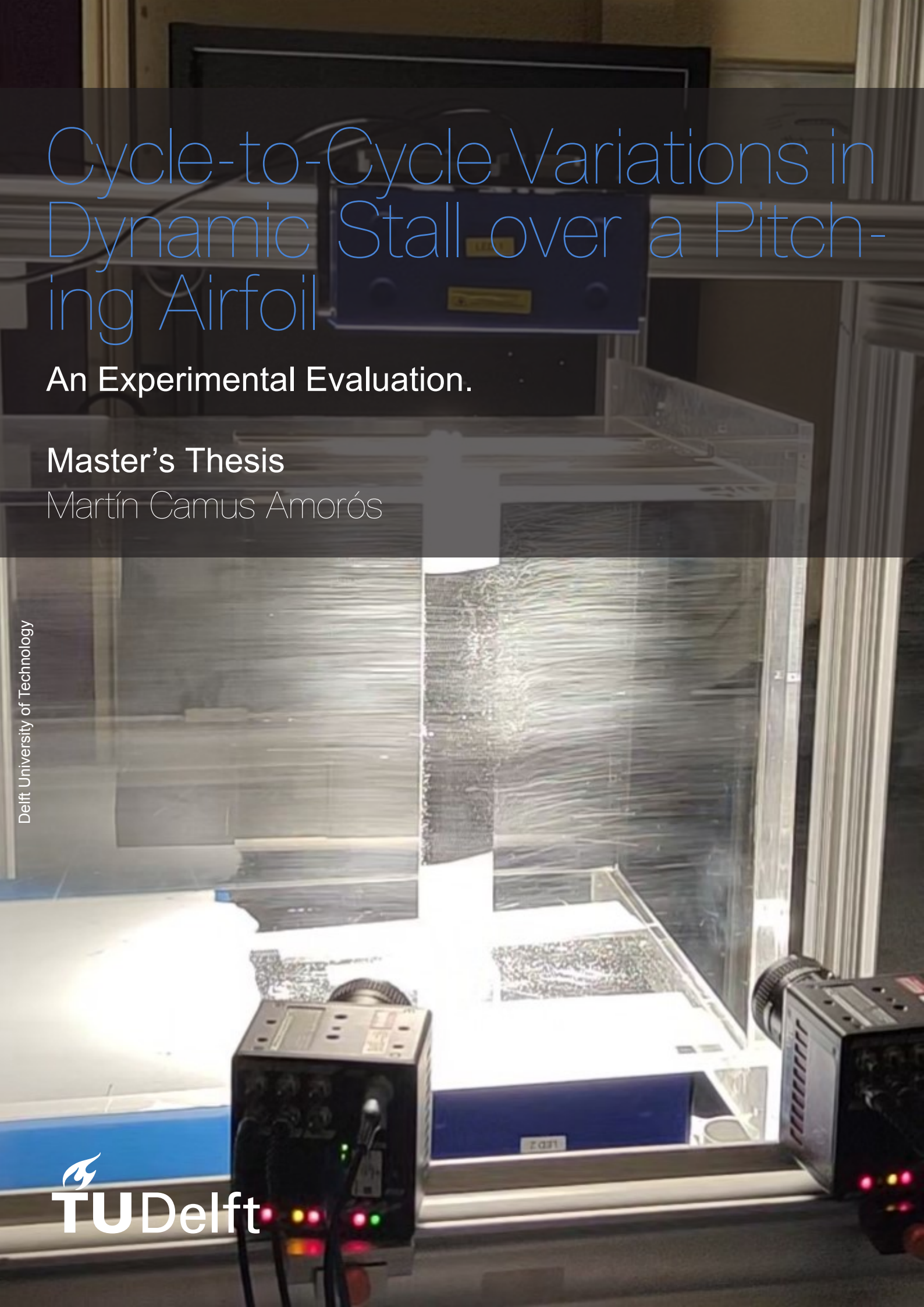

TU Delft

Master's Thesis

Cycle-to-Cycle Variations in Dynamic Stall over a Pitching Airfoil

Graduation Project

Student Name	*Student Number*
Martín Camus Amorós	4857127

Daily Supervisor: Morgan Li

Institution Delft University of Technology
Place Faculty of Aerospace Engineering, Delft

Date Monday 15th July, 2024

TU Delft

Preface

This thesis marks the end of my Master's degree, and the beginning of my new stage as a full-blown engineer. Despite the challenges and the tough times, this path has allowed me to grow professionally and as a human. In particular, this thesis project is what has inspired me to pursue a career in research as an experimental aerodynamicist.

It is therefore imperative for me to start by thanking my thesis supervisor Morgan Li, for her daily support, attention, experience, and inspiration. Without her, not only would this project not have been possible, but also, my future prospect would be significantly more unclear. I wish to mention the role that all the other professors played during my studies, in particular those of Fulvio Scarano and Andrea Sciacchitano, who were in charge of my favourite course of the Master's program at the time I took it, and inspired me to pursue a thesis related to flow measurement techniques.

Next, I must mention the individuals that made the true efforts and are behind all the best decisions I could have taken throughout the years, my parents and my sister. They have supported me not only with huge financial effort by a humble family from the outskirts of my beautiful Madrid, but also with their trust, and their support for my personal decisions. It even goes back to when I was a little kid, as they taught me to think for myself, with critical reasoning, and educated me in the ideals that I value so much in myself today. *Gracias papá, mamá, y Paula. Me habéis llevado hasta aquí, y aunque siempre he sido consciente del esfuerzo y lo he agradecido internamente, era importante para mí mencionaros en este último proyecto. Os quiero mucho, gracias por todo.* I am also grateful for other members of my family who always stand up for me and show unconditional love, trust, and support. I want to mention my *abuela*, and my *tía Carmen*, whom I am lucky to call my family, but also all the other family members who show true interest and support.

It is difficult to put in words how important my friends are. They are the ones who know all my secrets, and who, without being my blood family, will always have my back, no matter how many mistakes I make along the road. My chosen family. To the ones I see every day, the ones I only text with every now and then, and the ones I only speak to when I go back home, but are always there waiting for me to come back. To everyone, thank you. All the best.

With this report, my student life comes to an end. I have been extremely lucky to study what I study, work on what I want to work, and be where I want to be. I am particularly proud of this graduation project, since I feel like I have really built this up the way I wanted, and managed to get results that are very exciting. Again, huge thanks to the people along the way, and I hope you enjoy reading the thesis.

Abstract

An experimental campaign on dynamic stall was performed, in which a volume over a pitching wing was measured under different conditions, using three-dimensional Particle Tracking Velocimetry (PTV), with Helium Filled Soap Bubbles (HFSB) as tracers. The objective was to investigate to what extent the spanwise 3D effects over the wing were contributing to the cycle-to-cycle variations in dynamic stall, commonly studied using single-point or planar measurements. The results were clear in showing that these cycle-to-cycle variations are a manifestation of spanwise variations of the flow structures. These structures exhibited a tendency towards a certain state or mode, and the points close to the limit of the separation bubble were shown to take either a separated or an attached state, depending on the cycle and the spanwise location, leading to a 'bi-state' distribution of single-point statistics. Regarding the different cases examined, it was concluded that the pitch rate was a dominating factor for dynamic stall and spanwise variations, since a faster rate led to a later separation, but more violent and with higher variations in the DSV core once stalled. Other studied parameters like the reduced frequency or the airfoil thickness further showed that the variations are dominated by changes in the DSV core along the span. Recommendations for further research include monitoring the inflow conditions and limiting the accumulation of HFSB over the airfoil surface.

Contents

Nomenclature

Abbreviations

Abbreviation	Definition
CAD	Computer Aided Design
CCD	Charge-Coupled Device
CMOS	Complementary Metal Oxide Semiconductor
CFD	Computational Fluid Dynamics
DSV	Dynamic Stall Vortex
fps	Frames Per Second
HFSB	Helium Filled Soap Bubbles
JPDF	Joint Probability Density Function
LE	Leading Edge
PDF	Probability Density Function
PIV	Particle Image Velocimetry
POD	Proper Orthogonal Decomposition
PTV	Particle Tracking Velocimetry
rms	Root Mean Squared
STB	Shake-The-Box
TE	Trailing Edge
UAV	Unmanned Aerial Vehicle
URANS	Unsteady Reynolds-Averaged Navier-Stokes
voxel	Volume Pixel

Symbols

Symbol	Definition	Unit
C_l	Airfoil lift coefficient	[-]
C_d	Airfoil drag coefficient	[-]
C_m	Airfoil moment coefficient	[-]
c	Chord length	[-]
D	Drag	[kg m/s^2]
d	Diameter	[m]
f	Frequency	[Hz]
g	Acceleration of gravity	[m/s^2]
k	Reduced frequency	[-]
L	Length	[m]
m	Mass	[kg]
M	Mach number	[-]
N	Newtons	[kg m/s^2]
Q	Q-criterion	[s^{-2}]
R	Radius	[m]
S	Surface	[m^2]
S_k	Stokes number	[-]
u	Velocity in the x direction	[m/s]
V	Velocity	[m/s]
$\mathbf{V}$	Velocity vector	[m/s]
V_∞	Freestream velocity	[m/s]
x	Coordinate in the x direction	[m]
x	Value of the distance in the x direction	[m]
y	Coordinate in the y direction	[m]
y	Value of the distance in the y direction	[m]

Symbol	Definition	Unit
z	Coordinate in the z direction	[m]
z	Value of the distance in the z direction	[m]
α	Angle of attack	[º]
α_{ss}	Static stall angle of attack	[º]
δ_{99}	Boundary layer thickness	[m]
ρ	Density	[kg/m^3]
μ	Static friction coefficient	[-]
μ	Dynamic viscosity	[-]
$\mu(x)$	Average of the variable x	[x_{units}]
$\sigma^2(x)$	Variance of the variable x	[$x_{units}{}^2$]
θ	Phase	[rad]
ω	Circular frequency	[rad/s]
ω_y	Vorticity in y	[s^{-1}]

1. Introduction

Dynamic stall is a phenomenon present in a wide range of moving wings for different applications. While mostly seen in rotating wings, such as helicopter blades or wind turbines, dynamic stall is also present on flapping wings, gathering increasing interest, specially with the zenith of Unmanned Aerial Vehicles (UAVs). The physics are somewhat similar to static stall, but its dynamic nature proposes a more unsteady framework, increasing its complexity. Despite having been a topic for investigation since the 1980s [1], leading to extensive research on it, dynamic stall is still not a fully characterized physical phenomenon.

In particular, there is one aspect of dynamic stall that has captured the attention of researchers in the last decade, being the cycle-to-cycle variations. It was observed that for every dynamic stall cycle on a pitching wing, there were significant differences between each of them, and therefore, the classical approach of phase-averaging the measurement results from multiple cycles was not accurate enough. Cycle-to-cycle variations can cause a cycle to reach up to an 18% increase in load with respect to the phase average, and up to 40% increase in the moment coefficient with respect to the phase average [2]. However, the reason why these cycle-to-cycle variations exist has not been completely uncovered. In fact, one of the reasons behind the challenging modelling of dynamic stall through simulations, could be behind these cycle-to-cycle variations [3]. Therefore, characterizing them and finding their origin could lead to significant improvements in future development of dynamic stall simulations. In practice, more accurate simulations, means faster and more advanced development, and more efficient engineering systems as a result.

In order to tackle this problem, an experimental campaign using state-of-the-art measurement techniques was performed with the aim of characterising cycle-to-cycle variations in dynamic stall of a pitching wing, using three-dimensional, time-resolved and phase-locked measurements. The objective was to discover to what extent 3D effects are one of the reasons behind cycle-to-cycle variations in dynamic stall. In particular, the degree to which 3D effects would cause spanwise variations leading to changes in the separation point location along the span, and if the Dynamic Stall Vortex (DSV) evolves in the spanwise direction, was to be found. In addition to that, and for the sake of completion of the cycle-to-cycle variations characterization, the effect of reduced frequency, motion amplitude, and airfoil thickness, on the variations, was to be investigated.

The report is structured as follows. Chapter 2 provides the necessary background on dynamic stall and cycle-to-cycle variations through a literature study. The current knowledge on these topics is summarized here. Since the research is built around an experimental campaign, the measurement techniques used, as well as the set-up, are explained in Chapter 3. The wind tunnel configuration, as well as the measured cases, and the post-processing operations, are also given here. The main body of the report is included in Chapter 4. This chapter encompasses all the analyses performed on the measurements taken and provides the main takeaways of the project. Next, recommendations for further research on dynamic stall are given in Chapter 5. Finally, the main takeaways are summarized in Chapter 6, where recommendations for future research on dynamic stall are also given.

2. Background Information

This chapter is a literature study in which the fundamental aspects of the relevant physical phenomena are discussed. Dynamic stall is explained in Section 2.1, while the problematic with cycle-to-cycle variations is exposed in Section 2.2. The chapter closes with the research questions derived from this literature study.

2.1. Dynamic Stall

In this section the fundamental phenomenon being studied for this research, the dynamic stall, is explained. Dynamic stall impacts the performance of wind turbines, helicopter blades, propellers, and any kind of rotating wing. Therefore, studying its physics and measuring its consequences is important for improving the efficiency of rotors. Section 2.1.2 explains the basic concepts of flow separation. Section 2.1.3 goes through the dynamic stall cycle, explaining its stages with a focus on the physical phenomena behind every process. Section 2.1.4 explains the distinction between deep and light dynamic stall, providing a physical reasoning behind that characterization.

2.1.1. Definition

In order to understand cycle-to-cycle variations in dynamic stall, it is important to know what this phenomenon means both in terms of its aerodynamic structures and its performance. Just like static stall, in dynamic stall, the flow separates from the suction side of the airfoil, leading to a drop in lift and moment coefficient, and an increase in drag. The physical definition of the mechanisms involving flow separation are given in Section 2.1.2. Dynamic stall takes place in rotating wings, which are often modelled as a 2D wing undergoing pitching motion. On a pitching airfoil, dynamic stall takes place past the angle of attack that static stall would take place for the non-pitching case. This is because of the relative incidence angle that the airfoil experiences when pitching up. However, despite the stall starting later, the phenomenon is usually more dramatic and persistent than static stall, and shows hysteresis [1].

2.1.2. Separation

Dynamic stall is a phenomenon that is closely linked to the concept of flow separation, and is therefore inherently viscous. In order to discuss flow separation, it is interesting to first define what a boundary layer is. For simplicity, the following definitions will be limited to two-dimensional flows. Ludwig Prandtl defined the boundary layer as the region of flow affected by viscosity, in which the flow transitions from the no-slip condition (meaning that the flow velocity is zero) at a surface, to the flow at external conditions (unaffected by viscosity) [4]. This region becomes thinner the higher the Reynolds number (Re), defined in Equation 2.1, where ρ is the flow density, V_∞ is the freestream flow velocity, L is the characteristic length of the flow, and μ is the dynamic viscosity of the fluid. The boundary layer can consist both of laminar or turbulent flow. As originally explored by Osborne Reynolds [5], in laminar flow there is little to no movement of particles perpendicular to the flow direction, while turbulent flow experiences random motion in all directions [6].

$$Re = \frac{\rho V_\infty L}{\mu} \tag{2.1}$$

Flow separation occurs when the boundary layer of a flow detaches from the surface. A detached boundary layer means that the flow at the surface has locally decreased its velocity so much that its direction with respect to the wall reverses, leading to the so called reverse flow, shown graphically in Figure 2.1, which gives a schematic drawing of the velocity gradients over a separating airfoil. The flow reversal is caused by an increase in pressure as the flow advances, usually referred to as adverse pressure gradient [7]. This adverse pressure gradient can be obtained from inducing a pressure gradient in space, through the so-called pressure-induced separation, but can also take place by physically inducing the separation with an obstacle in the flow, referred to as fixed-separation [8].

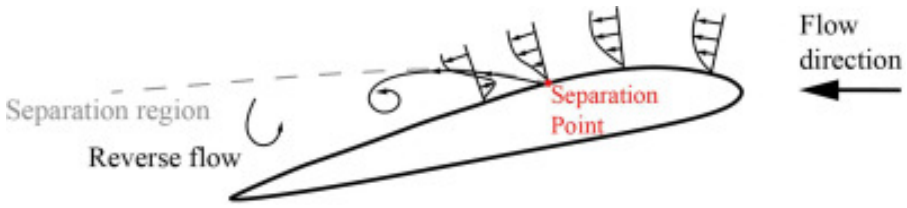

Figure 2.1: Diagram of flow reversal and separation [9].

Downstream of the separation point, the flow may encounter a decrease in pressure, usually called favourable pressure gradient, which is the opposite of an adverse pressure gradient. A favourable pressure gradient may lead to re-attachment, meaning that the flow is not reversed anymore. The region of reverse flow between the separation point, and the re-attachment point, is often referred to as separation bubble, shown schematically in Figure 2.2. A characteristic of separation bubbles is that regardless of whether the flow is laminar or turbulent upstream of the separation point, after re-attachment the flow becomes fully turbulent [10].

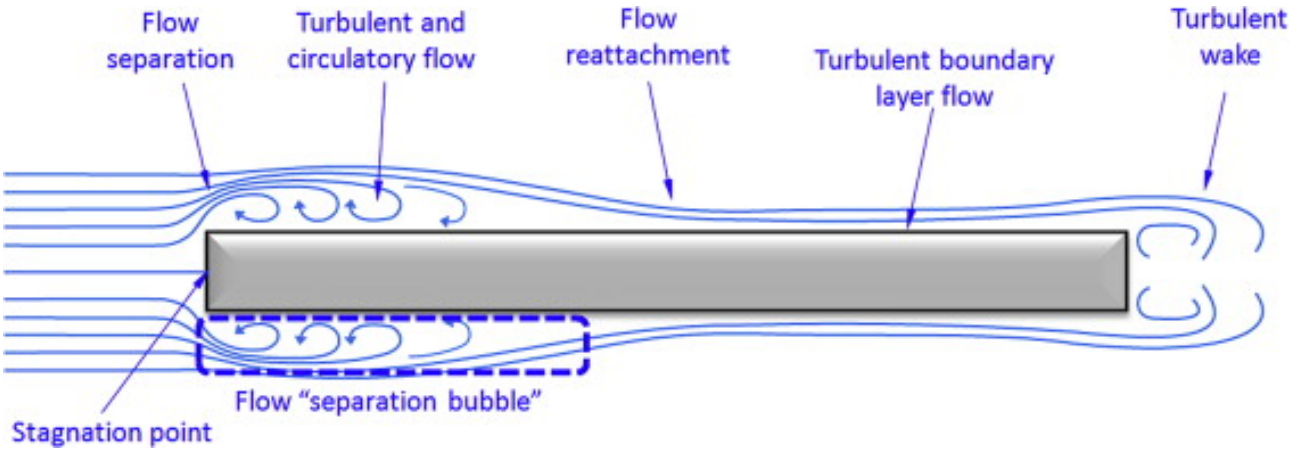

Figure 2.2: Separation bubble over a flat plate [11].

With turbulence being inherently unsteady, it is reasonable to realize that separation bubbles are an unsteady phenomenon. Not only they are unsteady due to the turbulence that they experience, but also, the size and shape of separation bubbles are not constant over time. This leads to changes over time for the airfoil air loads, as the pressure distribution over the airfoil changes with the separation bubble.

These changes over time on pressure-induced separation bubbles have been found to be characterized by two separate physical phenomena [8]. The first one is a low frequency mode in which the bubble experiences a contraction-expansion movement, a so-called "breathing" motion. This motion appears at the separation and re-attachment points, with these changing over time. This mode has a Strouhal number, defined in Equation 2.2, between 0.08 and 0.2. For this case, in Equation 2.2, f is the frequency of the phenomena, the reference length L is the re-attachment length, and V_∞ is the freestream velocity. In fixed-separation bubbles, a similar phenomenon is observed, which is referred to as "flapping" motion. According to Hudy et al [12], the re-circulating flow inside the bubble induces an oscillation that leads to the expansion and contraction of the bubble. However, for pressure-induced separation bubbles, there is no agreement on the physical mechanism behind the breathing motion. Kiya and Sasaki [13] proposed the existence of a secondary vortex shedding on top of the usual vortex shedding of the bubble, with larger scale vortices that shed at a lower frequency, and originated from the merging of vortices from within the bubble. These larger scale structures were observed computationally by Yang and Yoke [14], although they explain the origin of these vortices with the existence of "small bubbles" inside the separation bubble, that merged into the large scale vortices. Cherry et al [15] mentioned the similarity between the frequency of the breathing motion and the frequency of the shear layer change between shedding cycles. Eaton and Johnston [16] observed an imbalance between the inflow in the reversed flow area and the outflow at the re-attachment point, and proposed it as the mechanism for the breathing motion.

$$St = \frac{fL}{V_\infty} \tag{2.2}$$

The second change over time in separation bubbles is a higher frequency mode related to the shedding of vorticity downstream of the separation bubble. The Strouhal number of this mode is usually between 0.5 and 1.0.

This so-called shedding mode has been explained in the past through two possible mechanisms. Historically, it has been related to separation of the boundary layer, leading to a thin shear layer. This layer is rolled up through Kevin-Helmholtz instabilities to form small scale structures with a thickness similar to that of the shear layer. These vortices merge as they move downstream, forming larger scale structures, and are shed downstream of the re-attachment point [17] [18]. More recently, another mechanism was proposed by Wee et al [19], in which the merging of the vortices occurs at a fixed position before being shed downstream, in a similar fashion to the wake of a blunt body. This ”wake mode” has been suggested to take place only under 2D conditions [20], and therefore has only been observed computationally. These mechanisms seem to be shared for the case of pressure-induced separation.

All these effects in the boundary layer demonstrate the unsteadiness and complexity of the topic studied here. These aerodynamic mechanisms will take place also in cycle-to-cycle variations of dynamic stall, and therefore its acknowledgement is relevant for this study.

2.1.3. Stages and Onset

Originally, the onset of the dynamic stall was defined by the airloads experienced by the airfoil [21]. Some of these are shown in Figure 2.3, in which the changing rate in loads such as the moment or drag coefficients are used as indicators of the stall onset.

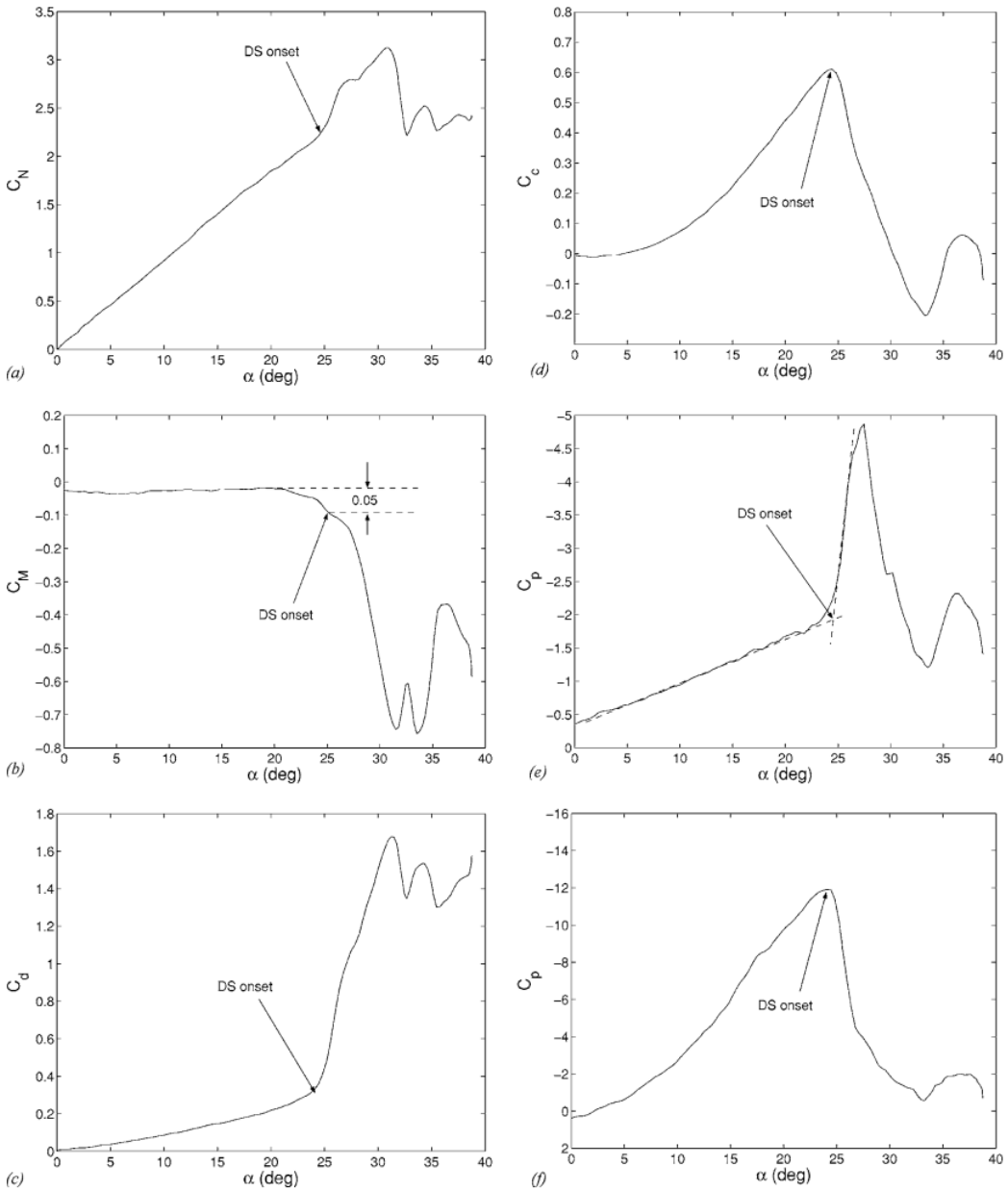

Figure 2.3: Point of stall onset based on **a)** Normal Coefficient, **b)** Moment Coefficient, **c)** Drag Coefficient, **d)** Chord-wise Force Coefficient **e)** Pressure Coefficient at the Quarter Chord, **f)** Pressure Coefficient at the Leading Edge [21].

More recently, another definition for the onset of dynamic stall has been used. Instead of being based on the loads over the airfoil, the flow structures and their evolution during dynamic stall are used to describe the onset. Mulleners and Raffel [22] define the following four stages for a dynamic stall cycle:

1. Attached flow stage.
2. Stall development stage.
3. Stall onset.
4. Flow re-attachment.

Figure 2.4 shows PIV slices at the middle span of an airfoil undergoing dynamic stall [22]. The attached flow stage is considered to match the part of the cycle from the lowest angle of incidence, until the angle of attack at which the airfoil experiences static stall (α_{ss}). During this stage, corresponding to plots **a)** and **b)** of Figure 2.4, the airloads follow the usual trend of C_l, C_d and C_m, with a suction peak near the leading edge, and with the flow attached to the surface.

Once the static stall angle of incidence is surpassed, the stall development stage starts. In this stage, corresponding to plots **c)** to **f)** in Figure 2.4, on the suction side of the airfoil, the ramping adverse pressure gradient increases its peak value, creating a region of reverse flow. This forms a shear layer between the freestream and the recirculating region, which is considered to be the primary instability of the flow, leading to the formation of individual vortices travelling downstream. These are small-scale structures, that are clockwise rotating for the case shown in Figure 2.4, and that experience little interaction with each other while convecting. While this happens, in terms of loads, the lift keeps increasing, as the external flow is barely affected by this primary instability, albeit slower than before due to the reverse flow occupying most of the suction side of the airfoil. As the angle of incidence increases, the vorticity interaction becomes stronger, and vortex merging starts occurring. These vortices eventually merge into one coherent structure known as the primary dynamic stall vortex (DSV). The DSV, being a low pressure region, creates a region of increased suction, and leads to the lift overshoot observed in Figure 2.3. While this happens, the merging small-scale structures that lead to the formation of the primary DSV, go onto creating counter-rotating secondary instabilities in the shear layer, as seen in image **d)** of Figure 2.4. These structures are then forced towards the LE of the airfoil by the clockwise rotating primary DSV. Once they reach the LE of the airfoil, the DSV detaches by vortex induced separation [23]. This is considered the onset of the dynamic stall [22], and takes place around plot **g)** from Figure 2.4. Vortex induced separation seems to behave similarly at both low and high Reynolds numbers (Re), differing in that at low Re the secondary instability in dynamic stall consists of a single region that detaches the DSV, while at higher Re the region is formed by multiple recirculating eddies that merge into a single larger scale structure [24].

Once the primary DSV detaches, it is convected downstream into the wake, and the stalled stage starts, corresponding to plots **g)** to **k)**. At this stage, flow starts recirculating ahead of the DSV, forming a secondary DSV. This vortex is also convected downstream, forming a new recirculating region upstream of it, and the cycle goes on. In this separated state, there is a shear layer around the recirculating region and the vortices. While the airfoil is pitching down, this process keeps occurring, with the consequent drop in lift and unsteadiness of the aerodynamic loads.

As the pitching down of the airfoil comes to an end, the flow re-attaches, going back to the initial stage of the cycle both in terms of flow-field features and airloads. This starts taking place around plot **l)** from Figure 2.4. In conclusion, Figure 2.4 shows the whole dynamic stall cycle, starting from the attached phase stage, then going through the aforementioned stall development process, and showing the onste of dynamic stall and the high vorticity of the stall stage, to end with the initial part of the reattachment.

In order to further analyze the aforementioned aerodynamic mechanisms, Mulleners and Raffel [22] performed a proper orthogonal decomposition (POD) on the PIV data used. This analysis gives the most energetic components of the flow for a certain data set, and in this case it gave three dominant modes. Firstly, the two most energetic modes, shown in Figure 2.7 **a)** and **b)**, give the fully attached and the fully separated flow cases. This makes sense, as within a cycle, a fully attached flow, separates in the upstroke, and then re-attaches again at the end of the downstroke, starting the cycle again (under the effects of hysteresis). This can be seen in Figure 2.7 **c)**, which shows how the two most energetic modes alternate within a cycle.

The third most energetic mode within the POD, shown in Figure 2.5, contains a coherent structure over the suction surface of the airfoil. This is the dynamic stall vortex, therefore showing the relevance of this structure for dynamic stall. As shown in Figure 2.6, this mode takes place between the fully attached and fully separated states, peaking before the flow is fully separated. Therefore, within a cycle of dynamic stall it can be said that the attached flow separates, undergoing a transitional mode in between dominated by a coherent structure.

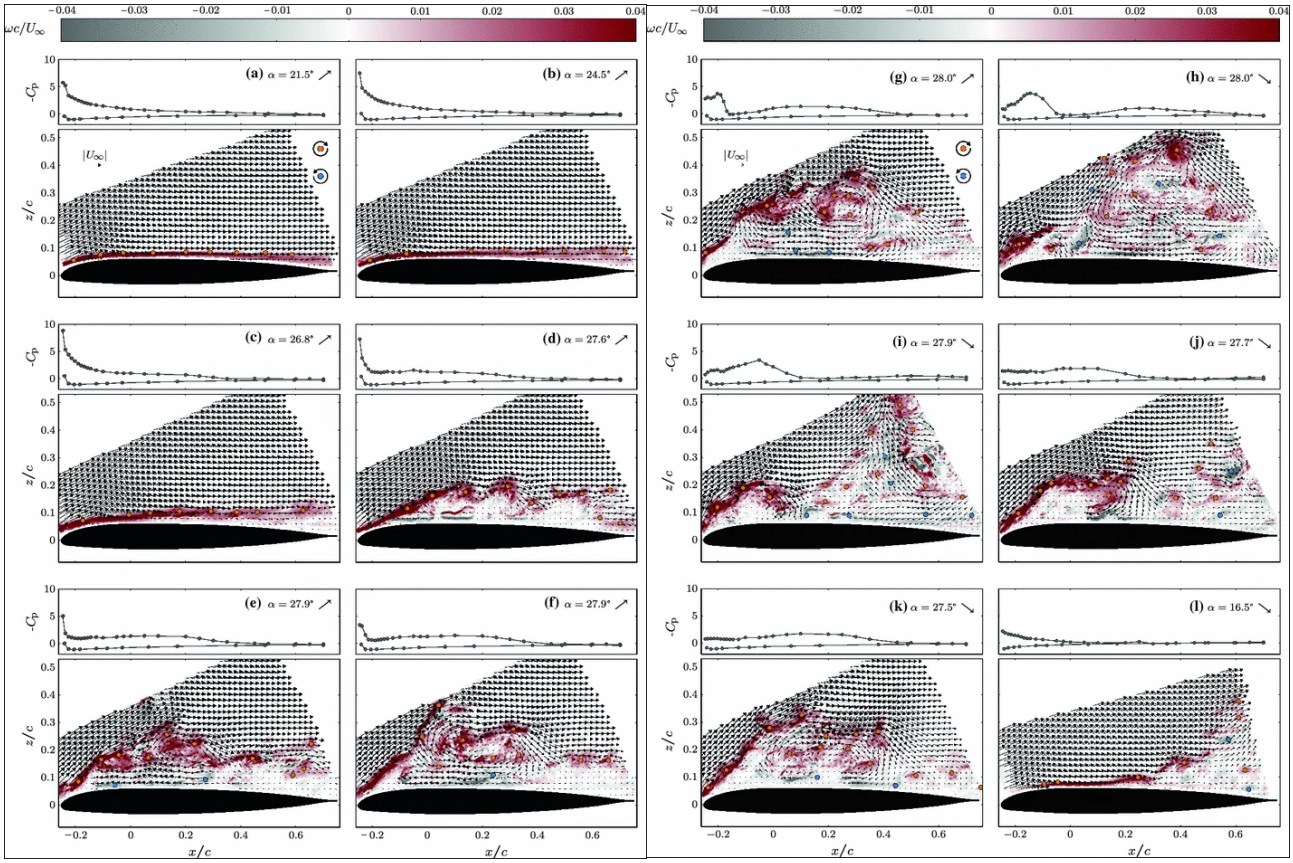

Figure 2.4: PIV images of the vorticity within a cycle [22].

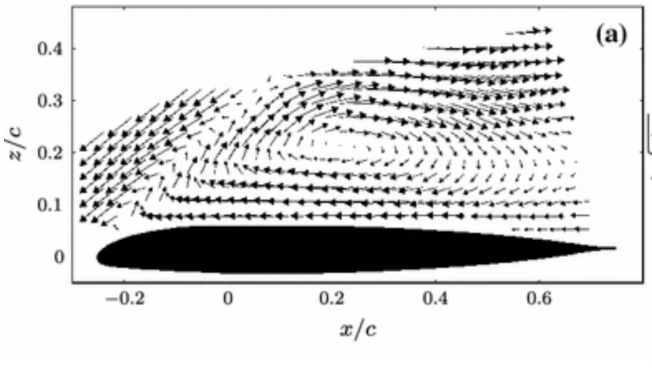

Figure 2.5: 3rd most energetic POD mode: Coherent structure [22].

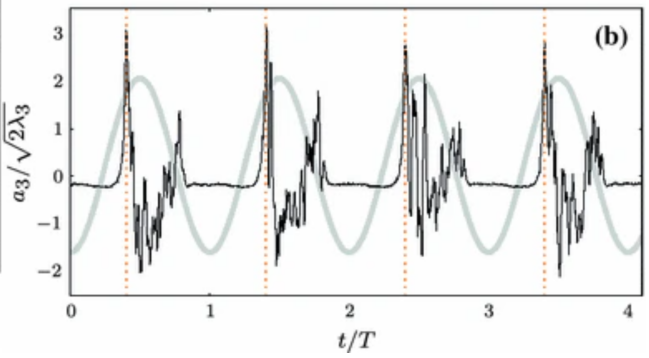

Figure 2.6: Distribution of the third mode over time [22].

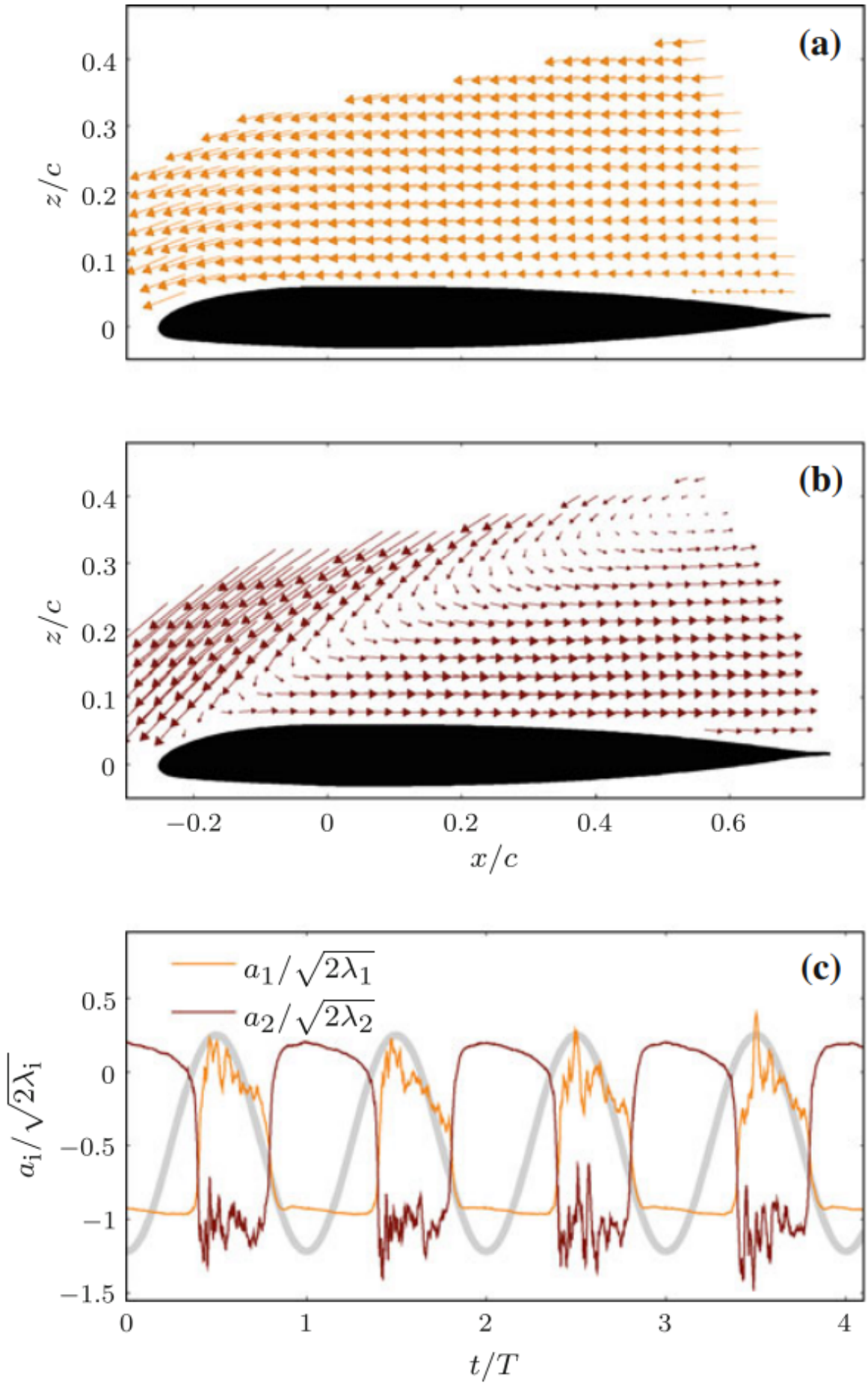

Figure 2.7: a) Most energetic POD mode: Fully attached flow. **b)** 2nd most energetic POD mode: Fully separated flow. **c)** Distribution of the first two modes over time [22].

2.1.4. Characterization of Dynamic Stall

Dynamic stall is often divided in literature into light and deep stall, based on the gravity of the flow separation as it is seen in Figure 2.8. Mulleners and Raffel [22] further define the distinction between light and deep stall using aerodynamic structures. They observed that in the light stall case, the primary DSV is not fully developed when the pitch down part of the cycle starts, while in the deep stall case the vortex detaches before completing the upstroke. This means that the separation in light stall occurs only when this downstroke starts, as a consequence of the change in the pitching direction. Therefore it can be said that the distinction between light and deep stall is originated from how the stall onset (DSV detachment) occurs.

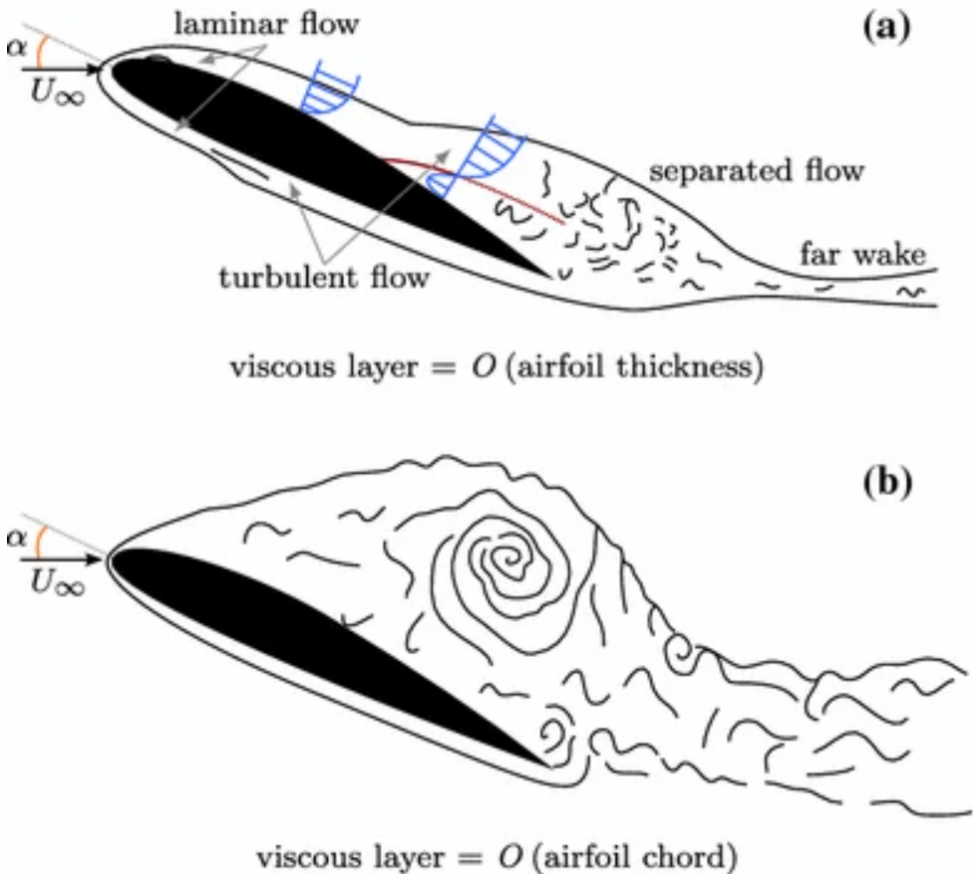

Figure 2.8: Light (**a)**) and deep (**b)**) stall comparison [25].

Now that the distinction between light and deep dynamic stall is established, both regimes can be characterized [1]. Light stall takes place for lower maximum angles of incidence, and is known to share some features with static stall, in particular in terms of airloads, as a drop in lift, drag increase, and pitch down moment. The phenomenon also exhibits considerable phase lag and hysteresis, in particular when it comes to the separation and re-attachment of the flow, as well as the airloads. Furthermore, light stall is known to be sensitive to the airfoil geometry, in particular to the nose radius, as this will determine whether the airfoil will experience LE or TE stall, consequently affecting the gravity of the stall, since LE stall is usually deeper. While in light stall the thickness of the wake is in the order of the airfoil thickness, deep stall encounters a viscous zone with a thickness in the order of the airfoil chord, as well as a stronger vorticity within it. This stronger vorticity contributes to the lift overshoot during the stall development, and therefore in deep stall the lift peak is higher than in light and static stall. Deep stall also experiences substantial hysteresis, which is the main defining factor for its quantitative characteristics.

2.2. Cycle-to-cycle Variations of Dynamic Stall

This chapter covers the specific object of study of the project, cycle-to-cycle variations in dynamic stall. These have been observed both in experiments and simulations, and are considered to be one of the reasons behind the disagreement of wind tunnel measurements and CFD simulations. This is due to the fact that simulations have traditionally been tuned to match phase averaged wind tunnel results, which do not take into account the variations between dynamic stall cycles, that have been proven significant in the study of rotating wings. Examples of these variations and their non-negligible effect on dynamic stall studies are given as motivation for the research in Section 2.2.1. Section 2.2.2 dives into the physical explanations that have been given to this cycle-to-cycle variations in the past, and the new hypotheses proposed by this study that might contribute to the phenomenon are given. Section 2.2.3 explains the effects that relevant parameters in the study of dynamic stall might have on cycle-to-cycle variations.

2.2.1. Motivation

In the study of dynamic stall, phase averages and standard deviations of the experimental data have traditionally been the chosen way of representing the data. However, this method of grouping the data has been proven inadequate by multiple authors. Harms et al [26] used Joint Probability Density Functions (JPDFs) to represent different dynamic stall cycles and analyze them. It was shown that there were significant differences between the phase averaged values of quantities like the pressure coefficient or the airloads, and the peaks of these quantities for certain cycles. It is important to note, that the cycle-to-cycle variations did not take place or were significant for the whole part of the cycle, or over the whole airfoil. The variations take place during the separation and re-attachment stages of the cycle, and therefore around 75% of the dynamic stall cycle is not affected by this phenomenon. Furthermore, the cycle-to-cycle variations do not take place along the whole airfoil, as the taps on the pressure surface, and closer to the trailing edge of the suction surface, do not show variations between cycles. Therefore, Harms et al [26] only considered a few pressure taps shown in Figure 2.9, that are located on the suction side of the airfoil, near the leading edge, for individual cycle analysis.

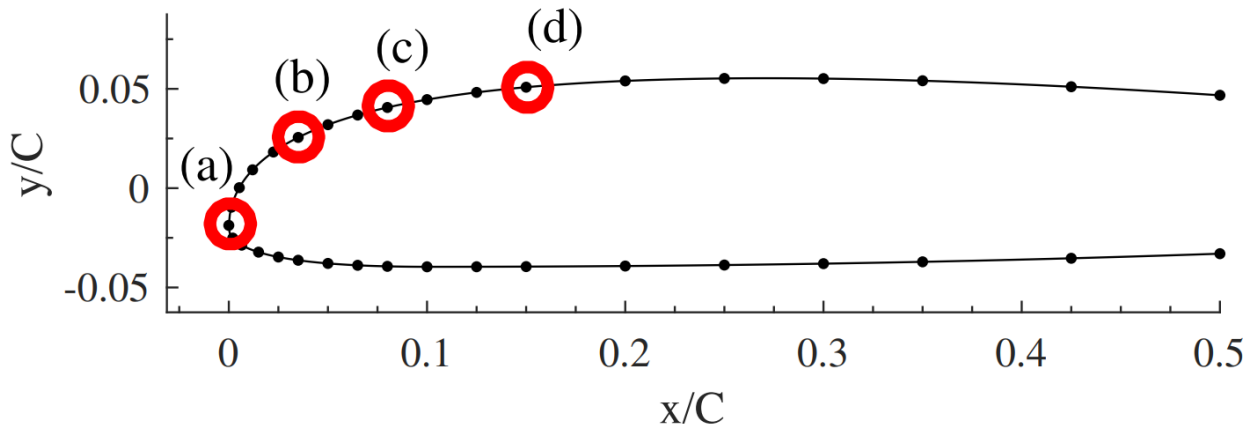

Figure 2.9: Pressure taps considered for individual cycle analysis: **a)**: x/c = 0 **b)**: x/c = 0.035 **c)**: x/c = 0.08 **d)**: x/c = 0.15 [26]

It is important to note that these cycle-to-cycle variations can take place at the operation conditions that the airfoil runs in a full-scale scenario. For example, Harms et al used a constant mean angle of 8.5° during their experiments [26], which is around the incidence under which the SC1094R8 airfoil usually operates. Ramasamy et al [2] found a 0.5° scatter in the angle of incidence at which the lift coefficient peaks between cycles, and this peak was in average around 8% higher for an individual cycle than for the phase average, and went up to 18% for some cycles. For the moment coefficient, the average of the peaks was around 10% larger for individual cycles than the phase averaged peak, with some cycles becoming up to 40% larger. These variations showed independently of the airfoil geometry, as the air load peaks were noticeably higher for both of the tested airfoils.

The consequences of these inaccuracies are that aeroelastic effects like flutter [27], which are common to happen under dynamic stall, can cause a larger mechanical deterioration or failure, as the loads on the blades are underestimated [2]. Besides the increased fatigue, as explained in Section 2.1, dynamic stall causes a drag increase, which is even larger when the air load peaks increase, decreasing the efficiency of the blades [26].

2.2.2. Definition

Despite dynamic stall being a known phenomenon that has already been studied for half a century, its understanding, and in particular, its computational modelling, has been a complicated topic. This happens as the CFD simulations of dynamic stall struggle to have significant agreement with experimental results. Computational simulations are usually accurate when modelling the ascending stroke of the dynamic stall cycle, and therefore when the flow remains fully attached. It is when the flow separates that the simulations lack agreement with experimental data. Holierhoek et al [28] did a comparison of different computational dynamic stall models, and concluded that none of them was able to accurately capture the phenomena. A similar conclusion was obtained by Nguyen et al [29], as they emphasized how in both 2D and 3D simulations, the stall peak pitching moment of the airfoil was consistently miscalculated. As explained in Section 2.2.1, one of the reasons behind this mismatch has been identified to be the fact that these simulations use phase averaged data from the experiments to model dynamic stall. Using these phase averages therefore becomes problematic if the phenomenon being modelled experiences significant changes each time it takes place. In this report, these changes are referred to as cycle-to-cycle variations [26].

As shown in Figure 2.10, the individual cycles, in blue, do not follow the phase averaged path, plotted in red, for a section of the cycle. Note that this is actually for the section of the cycle that corresponds to the separation and re-attachment phases of the dynamic stall cycles, while during the attached section of the cycle the agreement between the phase average and the individual cycles is better. When the phase average of the pressure is plotted, it is assumed that the actual pressure throughout a cycle will follow the plotted path. However, this is not the case in dynamic stall, depending on the flow conditions and the phase of the flow.

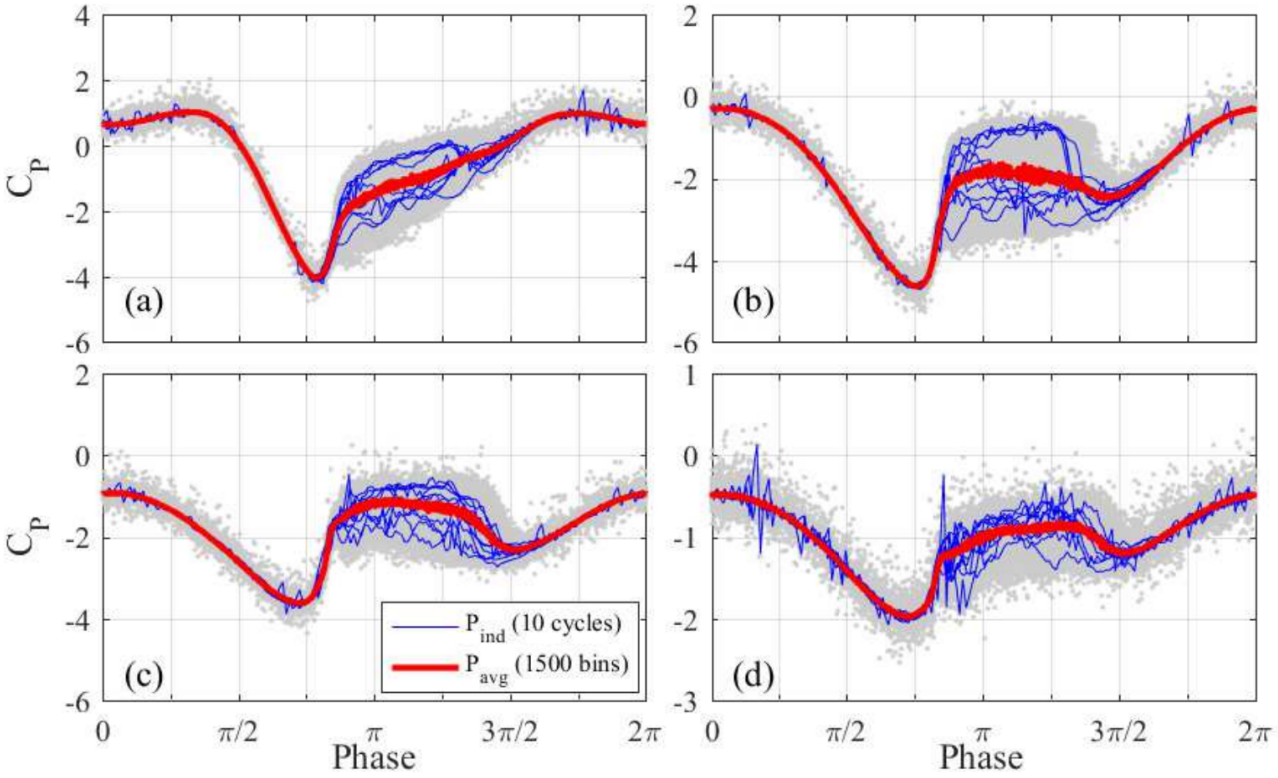

Figure 2.10: Comparison of the phase average path of the pressure with individual cycles at different chord-wise positions for a $k = 0.055$ and $\alpha = 8.5° \pm 9°$: a): $x/\bar{c} = 0$, b): $x/\bar{c} = 0.035$, c): $x/\bar{c} = 0.08$, d): $x/\bar{c} = 0.15$ [26].

This illustrates the differences between individual cycles and the phase averaged results that the airfoil experiences under dynamic stall. Harms et al used Joint Probability Density Functions (JPDFs) for the representation of cycle-to-cycle variations, which show the probability that the pressure has of following a certain path [30]. An example of this is shown in Figure 2.11, where the JPDF shows the values that the pressure is most likely to take, while the phase averaged result only shows a path that is not really close to what the individual cycles experience during separation.

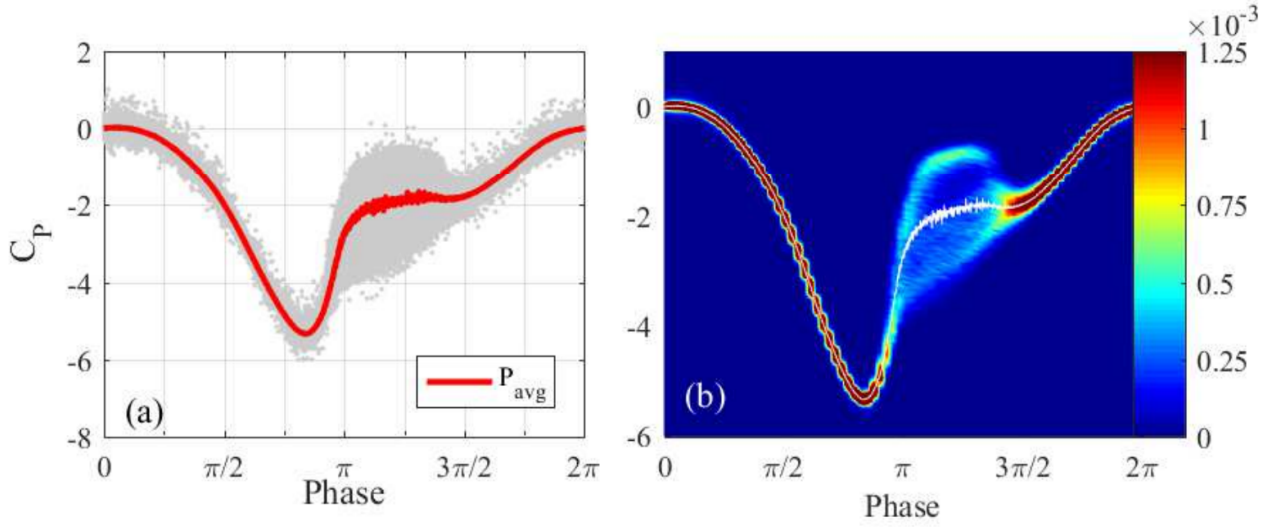

Figure 2.11: Comparison of the phase average (**a)**) representation of the pressure and the corresponding JPDF (**b)**) for a $k = 0.099$ and $\alpha = 8.5° \pm 9°$ [26].

From the JPDF Figure 2.11 it can also be seen that the pressure divides into two possible paths during the separation. This is referred to in this report as bifurcation. This means that each individual cycle is most likely to follow one of those two paths, with one of the paths being a separated state, while the other corresponding to an attached state. Ramasamay et al [3] performed a study in order to cluster each individual cycle to one of the possible paths, and developed an algorithm to define the number of bifurcations (clusters) present in each case. This one is based on Proper Orthogonal Decomposition (POD), and therefore the criterion to allocate an individual cycle to a cluster uses the most energetic flow structures to do so. This also allowed them to identify some of the flow features that differ between clusters and might contribute to the existence of these cycle-to-cycle variations. These are whether the stall is light or deep (refer to Section 2.1.4 for more information), whether there is leading edge or trailing edge separation, the separation location, and the location and size of the dynamic stall vortex, as it leads to significant variations in the air loads. The separation location stands out as one of the aerodynamic mechanisms behind cycle-to-cycle variations, and has been consistently proposed as such in studies before [2, 3, 31, 32]. These studies that have identified the separation location as one of the reasons behind the variations, have determined this through 2D PIV, observing changes in the separation location using a 2D PIV plane. Another possible contribution to this, is the breathing mode experienced in separated flows, as described in Section 2.1.2. Further proposed contributions to the cycle-to-cycle variations have been variations in the inflow conditions [33] and hysteresis between cycles [26].

In terms of forces, the impact that the study of cycle-to-cycle variations can have on the performance of rotating wings is significant, as the phase averaged air loads differ significantly from the loads in individual cycles, as can be seen from Figure 2.12. It is noteworthy that the cycles where the C_l peak takes place at an earlier phase, experience deeper stall. The opposite also holds, as the cycles that peak later, suffer from a lighter stall. Furthermore, the phase at which the lift coefficient peaks is different between cycles, and all these peaks experience a higher C_l than the averaged C_l peak, being up to 18% higher. The same happens with moment coefficient peaks, where this is most extreme, as the individual C_m peaks were up to 40% higher than the phase averaged C_m peaks.

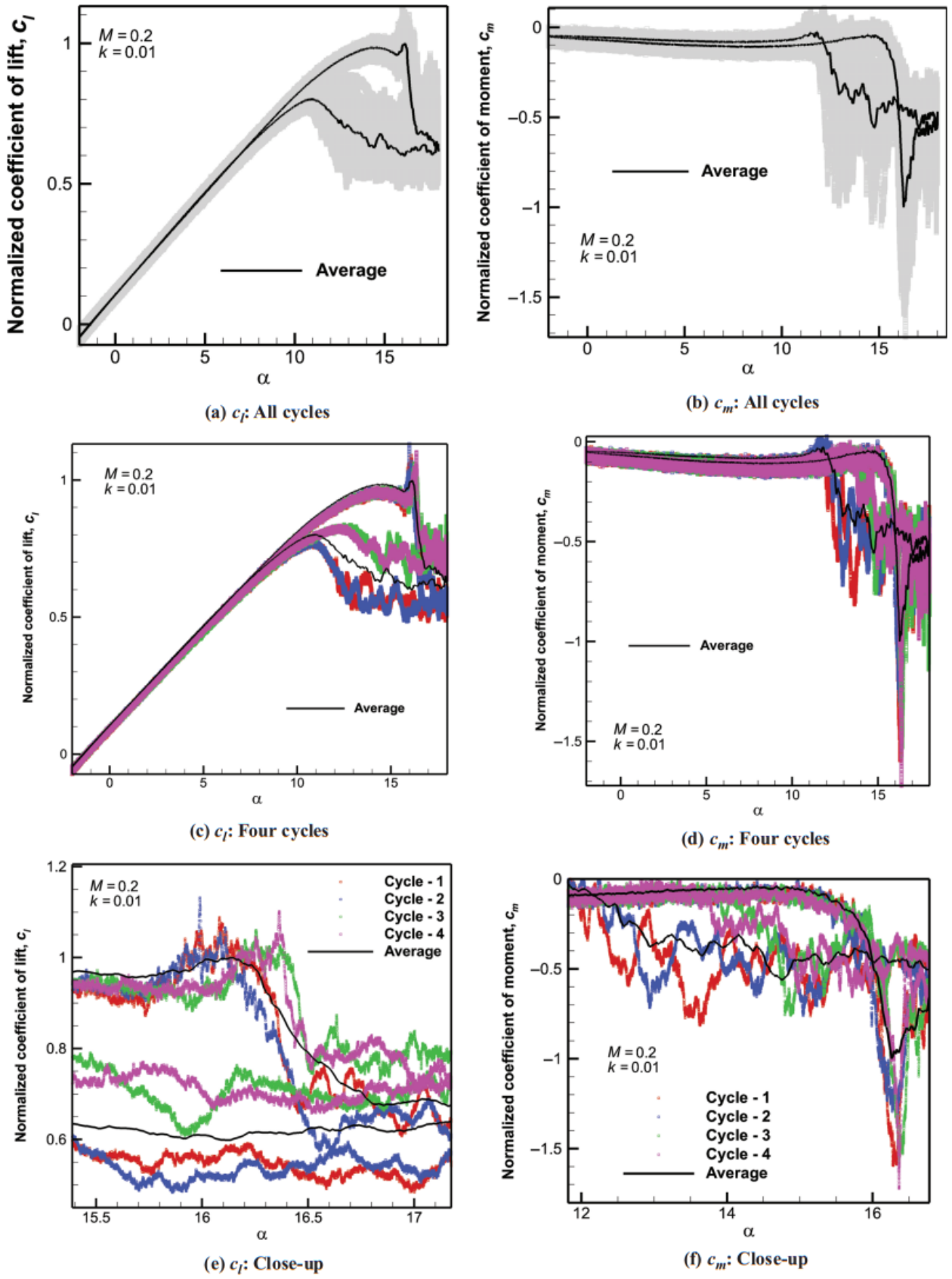

Figure 2.12: Individual cycles vs phase average for the lift coefficient (**a**), **c**,**e**)) and the moment coefficient (**b**), **d**,**f**)) [2].

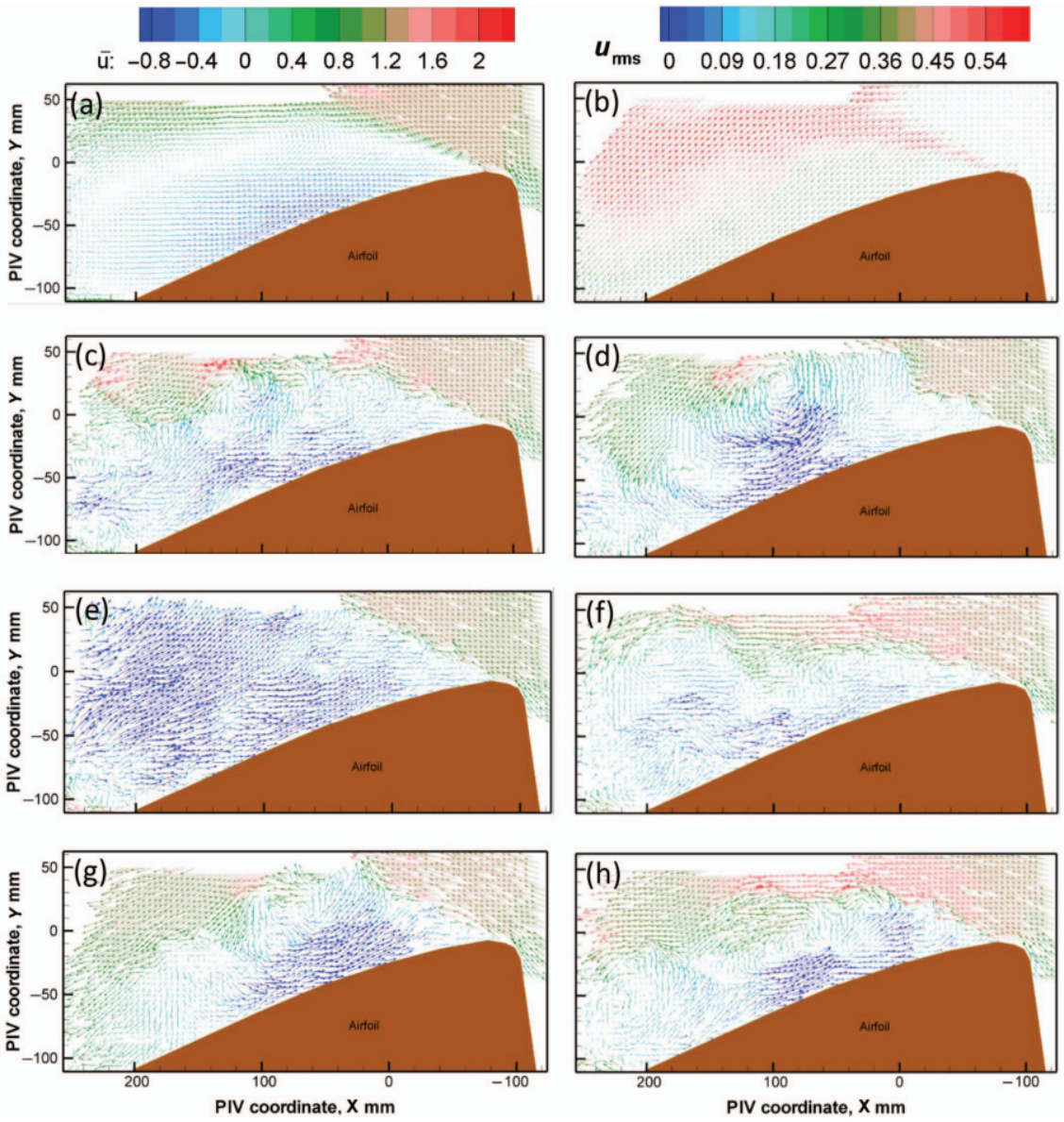

Figure 2.13: Velocity field of a dynamically stalled airfoil for $M = 0.3$, $k = 0.01$, α = 16.5º where: **a)**: phase average, **b)**: root mean square (rms), **c)-h)**: individual cycles [2].

Figure 2.13 further illustrates the cycle-to-cycle variations, this time using flow field data. Figure 2.13 **a)** shows the phase average of the flow field, which represents a separated airfoil with a single vortex-like structure over the surface, while Figure 2.13 **b)** shows the root mean squared, which shows large variations between cycles in the velocity field far from the airfoil surface. When looking at the individual snapshots, each of them actually shows different structures in the flow, like shear layer vortices in Figure 2.13 **c)**, a dynamic stall vortex in Figure 2.13 **d)**, or highly reversed flow in Figure 2.13 **e)**. All these properties are lost in the phase average, showing the inadequacy of this representation. These variations in the flow field had previously been shown by Wernert et al [34], who argue that the flow field around an airfoil undergoing dynamic stall is non-reproducible, and propose the inflow conditions as one of the reasons behind cycle-to-cycle variations.

2.2.3. Effect of various parameters

Despite the physics behind the cycle-to-cycle not being fully characterized yet, past studies have been able to observe how some of the relevant parameters in the study of dynamic stall affect these variations. This section is therefore looking into how cycle-to-cycle variations are affected by the reduced frequency (k), and the amplitude of the oscillation.

The reduced frequency is one of the most important parameters in dynamic stall studies, as it gives the frequency at which the full-scale rotating wing is performing. It is defined in Equation 2.3, where ω is the circular frequency, c is the chord length, and V_∞ is the freestream air speed.

$$k = \frac{\omega \frac{c}{2}}{V_\infty} \tag{2.3}$$

The reduced frequency has a direct effect on the cycle-to-cycle variations, as the bifurcation becomes more severe for the lower frequencies [26]. This means that, the higher the reduced frequency, the smaller the variations between dynamic stall cycles, to the point that there will be no cycle-to-cycle variations for very high reduced frequencies. This is illustrated by figure Figure 2.14, where the cases with the lower reduced frequency exhibit the most bifurcation. Furthermore, as explained in Section 2.1.3, in dynamic stall, the lift generated by the pitching wing under dynamic stall, overshoots the lift that the same wing generates in static conditions. This peak in suction also has a dependency on reduced frequency, as for higher reduced frequencies, the suction peak is also higher. Effectively this means that the phase at which the flow detaches is later than for the lower frequencies, or that the flow stays attached for a longer part of the cycle. A consequence of this is that the re-attachment is also delayed, so that for the higher frequencies, the flow only re-attaches by the end of the downstroke [26].

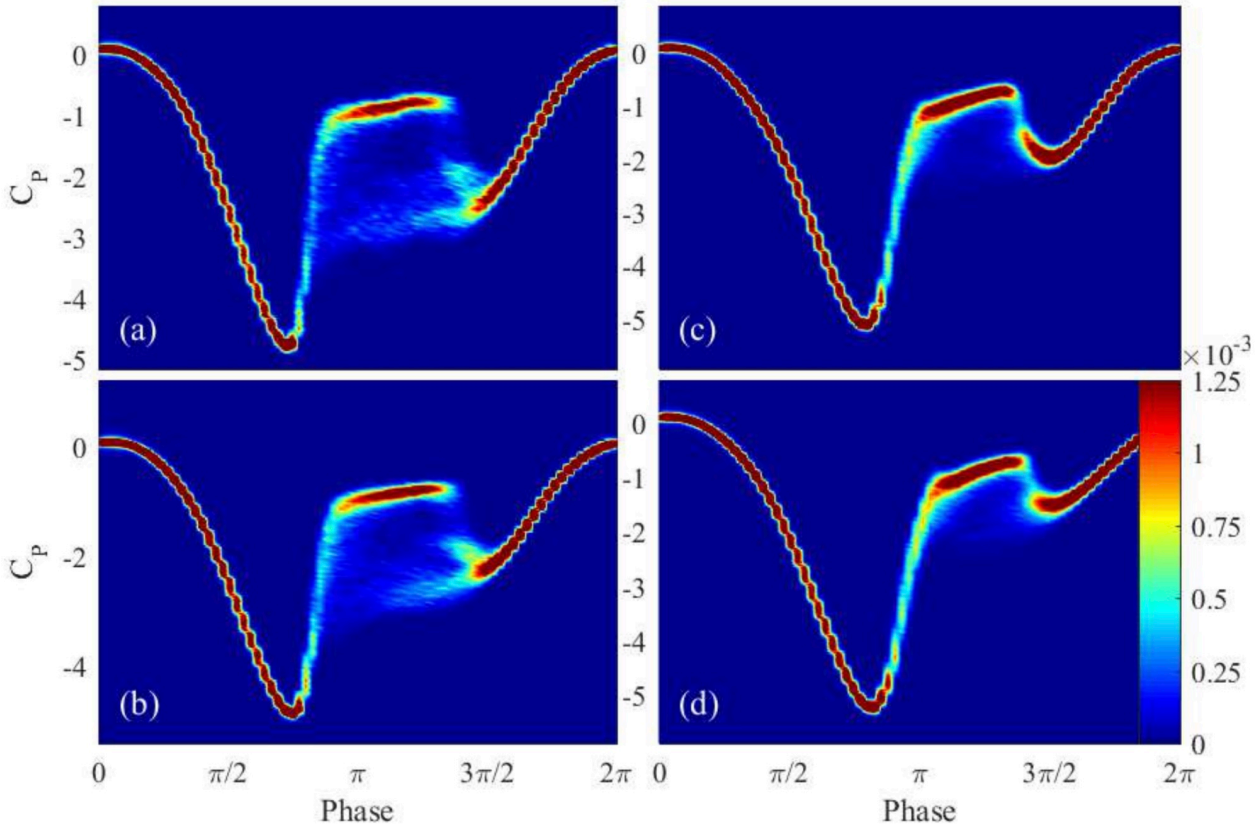

Figure 2.14: JPDFs of the pressure coefficient for the airfoil at $\alpha_m = 8.5$ and $\Delta\alpha = 11°$ and varying k: a): $k = 0.055$, b): $k = 0.067$, c): $k = 0.099$, d): $k = 0.121$ [26].

Other relevant parameters in dynamic stall are the mean angle of attack α_m and the amplitude of the oscillation $\Delta\alpha$. The mean angle of attack is the angle of incidence around which the airfoil pitches, the mid point between the minimum angle of incidence, and the maximum. On the other hand, the amplitude $\Delta\alpha$ is the angle that the airfoil undergoes while going from the mean angle of attack, to the maximum angle of incidence. These are shown graphically in Figure 2.15.

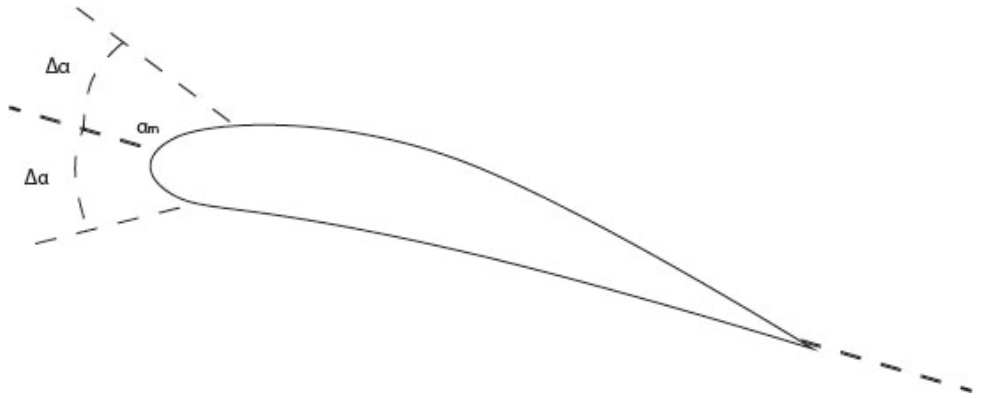

Figure 2.15: Definition of α_m and $\Delta\alpha$

Usually, the mean angle of attack determines whether the airfoil is under deep or light dynamic stall. Moreover, for the same α_m, the cases with a higher amplitude will experience a more serious dynamic stall [1]. The changes in bifurcation of the pressure data shown in Figure 2.16 show a dependency of the cycle-to-cycle variations on the amplitude of the motion. It can be seen that around the $\Delta\alpha = 13°$ case, the bifurcation does not take place anymore when increasing the amplitude. Similarly, for low amplitudes, like for $\Delta\alpha = 7°$, the bifurcation, while present, is minimal [26].

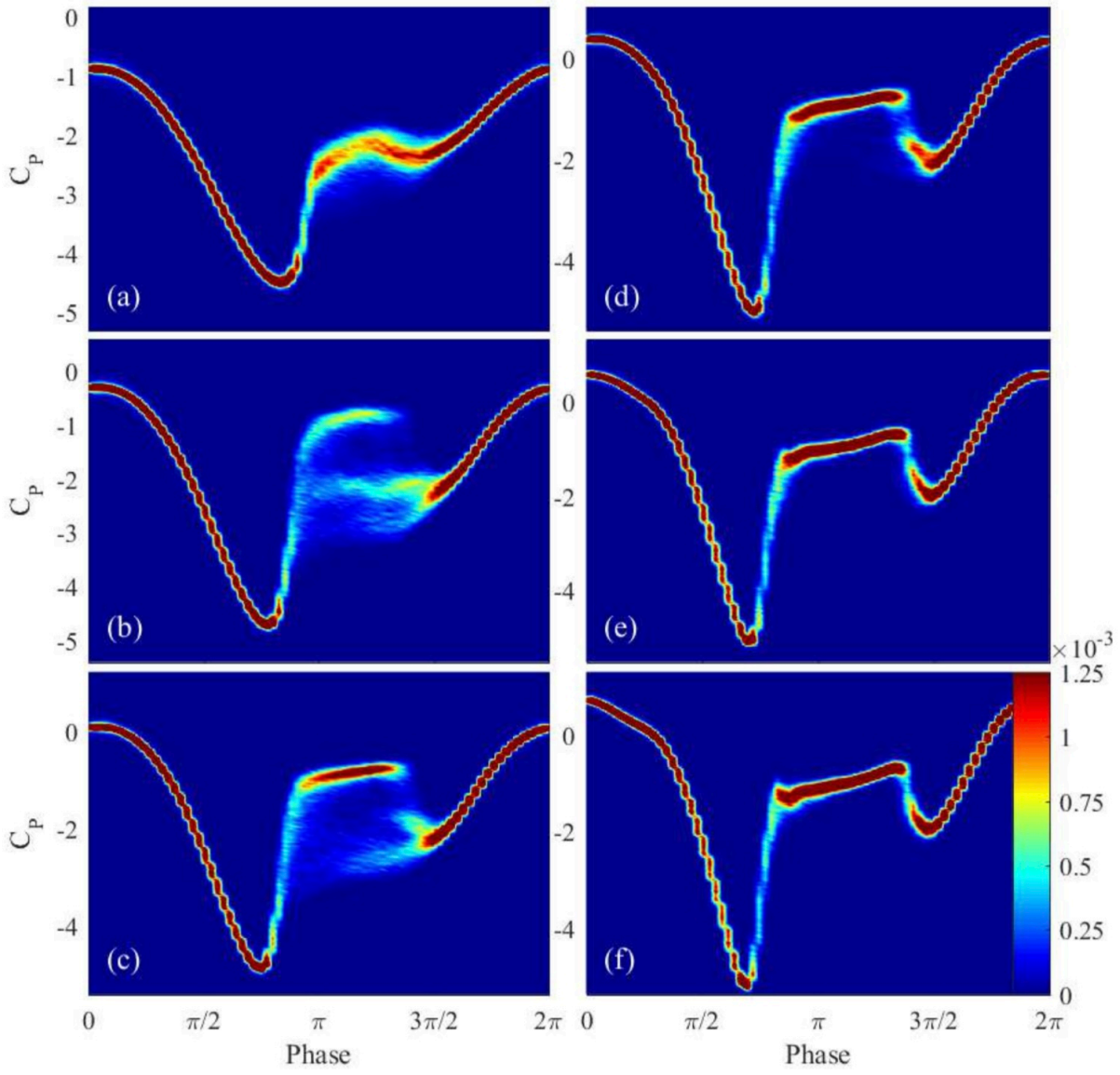

Figure 2.16: JPDFs of the pressure coefficient for the airfoil at $\alpha_m = 8.5$ and $k = 0.067$ and varying $\Delta\alpha$: a): $\Delta\alpha = 7°$, b): $\Delta\alpha = 9°$, c): $\Delta\alpha = 11°$, d): $\Delta\alpha = 13°$, e): $\Delta\alpha = 15°$, f): $\Delta\alpha = 17°$ [26].

While the geometry of the airfoil does not seem to have a big impact on the cycle-to-cycle variations [2], it affects the performance of dynamic stall in general [1]. However, the available data on the correlation between airfoil geometry and cycle-to-cycle variations is quite limited, and therefore further research on the relationship between airfoil geometry and cycle-to-cycle variations is required. On the topic of dynamic stall, the performance seems to be mainly affected by the LE radius. An airfoil with a sharper LE radius usually implies leading edge stall, which is more abrupt and has more unsteady airloads. Blunt noses usually experience TE stall, which is more gradual [1]. However, under deep dynamic stall, both types of dynamic stall perform similarly. As stated before, further research on airfoil geometry and cycle-to-cycle variations is required.

Mach number does not seem to have a big impact on the cycle-to-cycle variations, but it does change the amount of cycles that go into each side of the bifurcation [3]. On the other hand, the averaged peaks of air loads have been higher for increasing Mach number. However, the range of air speeds tested was not big [31], and therefore further study on the dependency of the variations with Mach/Re numbers would be useful.

2.3. Research Questions

Having looked into the existing literature for dynamic stall and cycle-to-cycle variations, a set of questions to be answered through the present text is to be presented. The research questions and sub-questions are the following.

- To what extent are 3D effects one of the reasons behind cycle-to-cycle variations in dynamic stall?
  - To what degree do 3D effects cause spanwise variations leading to changes in the separation point location along the span?
  - To what extent does the DSV evolve in the spanwise direction?
- What is the effect of the reduced frequency on the cycle-to-cycle variations?
- What is the effect of the motion amplitude on the cycle-to-cycle variations?
- What is the effect of the airfoil thickness on the cycle-to-cycle variations?

The first research question is the foundation of the project, and looks into the fundamental physical origin of the cycle-to-cycle variations. Its sub-questions look into aerodynamic structures, namely the separation line and the DSV, to build towards the main research question. The rest of the research questions look into the effect that different parameters of the motion have on the cycle-to-cycle variation, completing the project.

3. Experimental Set-up

As the research project is designed around a experimental campaign, in this chapter the measurement techniques, as well as the wind tunnel used, the cases being measured, and the post-processing operations, are given. Section 3.1 dives into the Particle Tracking Velocimetry technique used, while Section 3.2 gives the details on the wind tunnel being used and the test configuration. Section 3.3 provides the matrix used for the planning of the measurements, and Section 3.4 goes into the post-processing activities.

3.1. Particle Image Velocimetry

Particle Image Velocimetry (PIV) is a measurement technique that allows to obtain the velocity field of the flow. It provides flow visualization from the actual flow quantities, allowing for quantitative aerodynamic analysis. In order to perform PIV, there are three fundamental elements that are needed, tracer particles, illumination, and imaging. The flow is infused with tracer particles, which scatter the light using an illumination source. The scattered light is then captured by cameras (imaging), from where the data is sent to a computer for processing. These elements are shown schematically in Figure 3.1. In the upcoming section, each of the elements required for PIV will be discussed.

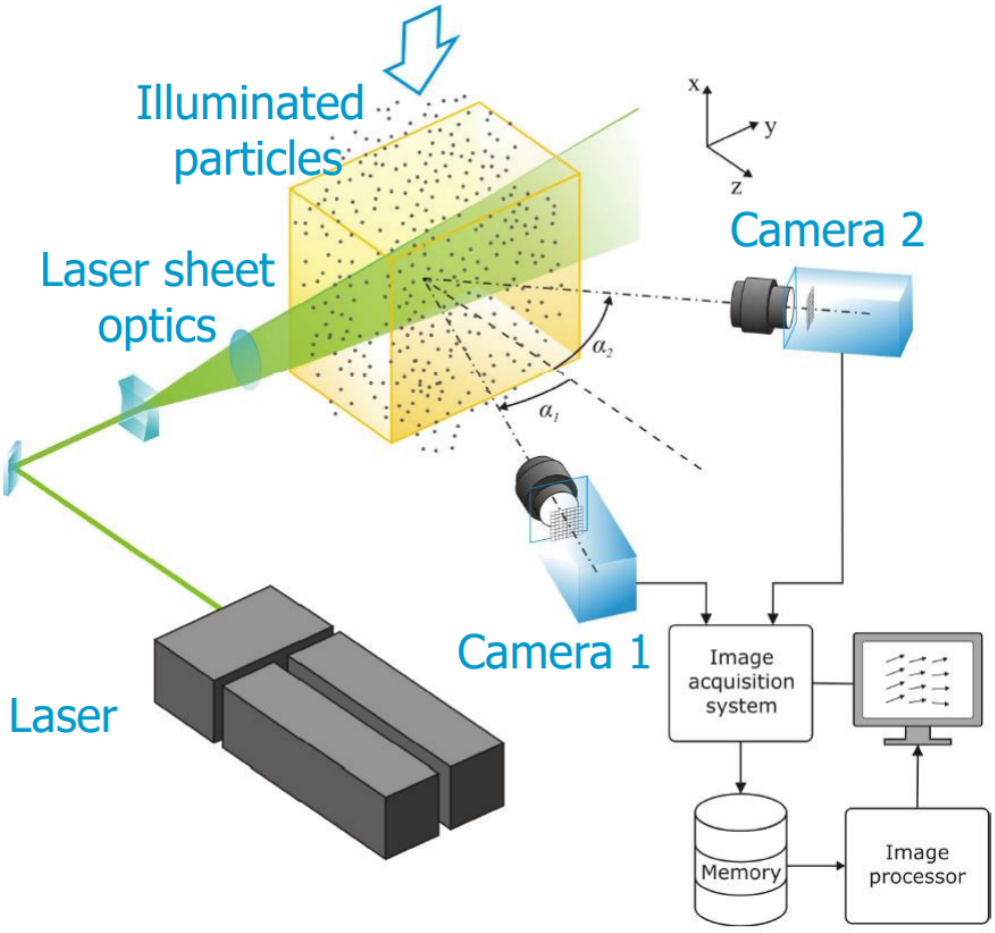

Figure 3.1: PIV set-up giving all three velocity components in a plane [35].

There are several variations of this technique, and for the present study, the choice is to use 3D Particle Tracking Velocimetry (PTV). The choice of a 3D technique is due to the research questions (Section 2.3) being related to the separation line shape and location of the flow features over the airfoil in dynamic stall. A three dimensional domain will allow to study how this separation location changes in space, and the structures that are causing this. PTV is chosen over tomographic PIV due to its lower computational cost and simpler experimental set-

up. It can also provide time-resolved results, so while PTV data has a lower resolution, as it will be explained in Section 3.1.1, time-resolved data and lower computational cost have been considered more valuable in measurements for an unsteady problem like cycle-to-cycle variations in dynamic stall [36].

3.1.1. Tracer Particles

The transparency of the air makes imaging of aerodynamic properties a challenging task. In order to be able to optically obtain aerodynamic properties, the experimental domain can be infused with the so called tracer particles. These are not only used for PIV, but also for other techniques like laser Doppler anemometry [37]. PIV particles have a set of requirements in order to be adequate for aerodynamic measurements [35]:

- Tracers must follow the flow.
- Tracers must scatter the light.
- Tracers must be non-toxic, non-hazardous, non-corrosive, and non-reactive.
- Tracers should naturally evaporate in order to avoid contamination of the experimental facility.

Focusing on the first requirement, the tracers having to follow the flow, has to do with the mechanical properties of these. A particle immersed in a flow experiences several forces such as an inertial force or the acceleration of gravity, but for a small tracer, the dominating force should be the Stokes drag. In order to determine whether a particle is suitable for tracing or not, the Stokes number is used. This number is the ratio of the particle response time and the flow characteristic time, as shown in Equation 3.1, and therefore indicates the effectiveness of the tracking using a certain type of particle. The smaller the particle response time, and therefore the Stokes number, the better the particle will be at following the flow, and usually a Stokes number below 0.1 is considered good for flow tracking [36]. Equation 3.2 gives a formulation for the particle response time, which indicates how fast a particle responds to a change in velocity, and is derived from the solution of the expression from the slip velocity given in Equation 3.3 for an accelerated flow. In Equation 3.2, d_p is the particle diameter, ρ_p is the particle density, ρ_f is the flow density, and μ is the dynamic viscosity of the fluid. The characteristic time of the flow, shown in Equation 3.4 is approximated from dimensional analysis by dividing a length scale of the flow with a characteristic velocity, like for the case of a turbulent boundary layer, given in Equation 3.5. In this case, the boundary layer thickness (δ_{99}) is divided by the freestream velocity (V_∞). For the current experiment, the length scale is the airfoil chord, which is 10 cm, and the characteristic velocity is the freestream velocity in the tunnel, around 5 m/s.

$$S_k = \frac{\tau_p}{\tau_f} \tag{3.1}$$

$$\tau_p = \frac{d_p^2}{18}\frac{\rho_p - \rho_f}{\mu} \tag{3.2}$$

$$V - U = -\frac{d_p^2}{18}\frac{\rho_p - \rho_f}{\mu}\frac{dV}{dt} \tag{3.3}$$

$$\tau_f \approx \frac{L_f}{\Delta V} \tag{3.4}$$

$$\tau_f \approx \frac{\delta_{99}}{V_\infty} \tag{3.5}$$

In the present study, the particles to be used are helium filled soap bubbles (HFSB), which have been shown to fulfill the first requirement for PIV particles [38]. The particle response time is around ten micro seconds, meaning that the particles are in the Stokes regime.

Another requirement for the tracer particles is that they must scatter the light. The light scattering depends mostly on the particle diameter, but also on the laser light wavelength and the ratio of refractive indices of the particle and the fluid [35]. It is in this requirement that the HFSB excel, as due to their larger diameter, they scatter a lot of light, allowing for time-resolved, 3D PTV experiments to be performed [38]. However, one of the drawbacks of this seeding, is that it provides lower resolution than standard PIV particles. This is not only because the particles are larger, but also because the PTV algorithm, explained in Section 3.1.4, is more limited in the amount of particles that can be traced.

3.1.2. Illumination

As the PIV system works by capturing the light scattered by the tracer particles, it is necessary to have a source of light that goes through the particles. Lasers play a crucial role in Particle Image Velocimetry (PIV) due to their ability to emit monochromatic light with high energy density. A typical laser configuration comprises three main components: laser material (atomic or molecular gas, semiconductor, or solid material), pump source (providing energy to excite the laser material), and a mirror arrangement (a resonator allowing oscillation within the laser material). Quantum mechanics principles explain the energy states of atoms in a laser, involving spontaneous emission and stimulated emission processes [36].

Despite lasers being the most widely used illumination devices for PIV, for the HFSB technique, the high energy density they provide is not needed, as the light scattered by HFSB, thanks to their large particle diameter, is enough already. Therefore, LED illumination is used instead. This has the advantages of being simpler to operate and robust, have lag-free pulses, no speckle, and reduced safety risks. However, the light is harder to collimate, which for a 3D domain like the one being proposed is not an issue, and may have lower pulse energy, which, as stated before, is not a problem due to the large particle diameter of HFSB [36], which is enough to scatter the light.

3.1.3. Imaging

In order to capture the scattered light from the particles into a usable signal that can be interpreted by a computer, cameras with adequate sensors are needed. For PIV, the most widely used type of sensors are Charge-Couple Device (CCD sensors) and Complementary Metal Oxide Semiconductor (CMOS), with the latter ones being used in high speed flows and time-resolved experiments, like the one treated in this text [39]. CCD sensors are devices that can convert light into electric charge, or photons into electrons. A CCD sensor is usually comprised of an array of multiple CCDs, often in a line or rectangular set up. Each of the individual CCDs is a pixel [36]. The normal sampling rate of a CCD sensor is in the order of 10 Hz, which is too slow for PIV. Therefore, a method called frame-straddling technique is usually applied, in which images can be obtained with a separation of just 100 ms [40]. On the other hand, for the current experiment, Photron high-speed CMOS cameras will be used, which are more suitable as they can capture images separated by 0.5 ms [41], at 2000 fps in this case.

In order to obtain an image from the imaging sensor, a system of lenses is to be used. This will determine the focal length of the lens, and the aperture. The aperture is usually described using the f-stop, defined by the ratio of the focal length and the aperture. This f-stop dictates the depth of field, which is the distance between the nearest and the farthest points that are in focus in an image, and the brightness of the image. A lower f-stop will give a brighter image with a smaller depth of field, while a higher f-stop gives darker images with a large depth of field [35].

3.1.4. Particle Tracking Velocimetry

For this experiment, an algorithm that gives the trajectory of the tracer particles is used, allowing to obtain time-resolved results by predicting the particle distribution of each subsequent time-step. The errors from this prediction are corrected using a technique called ‘Shake-The-Box’ (STB), an image matching technique. This provides high spatial accuracy thanks to being able to get rid of ghost particles. This Lagrangian tracking method allows to track densely seeded flows, and compared to tomographic PIV improves the local accuracy, the completeness of the solution, the spatial resolution, the temporal coherence, the computational effort, and the occurrence of ghost particles [42]. This technique does not use correlation functions the way standard PIV does.

In order to apply the Shake-The-Box technique, the process of evaluation of images is reversed. With this algorithm, the tracking process is performed first by predicting the positions of the particles at a certain time-step $k+1$. This is done using a Wiener filter [43] and the previous k positions of the particles. Next, the particles are ‘shaken’ in order to correct for the error of the prediction. ‘Shaking’ the particles means to move slightly the particle in all directions and choose the best position based on the location that gives the smaller residual. Once this is done, the new particles entering the volume are found on the residual images, and all the particles are ‘shaken’ again. Finally the particles leaving the volume are removed. The finding of new particles, their ‘shaking’, and the elimination of gone particles, is iterated if necessary, and new tracks for all the new particles are added for every consecutive four time-steps [42].

This ‘shaking’ correction is a position refinement, since the predicted positions are already quite accurate. ‘Shaking’ is an technique that attempts to minimize the residual image by moving the particle in space using small steps and calculating their residual with respect to the image k, looking for the minimum [44]. This process is applied independently to all particles, moving them in all three spatial directions, typically with a step size of 0.1 pixels [42].

3.2. Wind Tunnel Configuration

3.2.1. Wind Tunnel

The experimental campaign is designed to be performed in the W-tunnel, located in the High Speed Laboratory of the Delft University of Technology in the Netherlands. This is an open-return wind tunnel, with an exchangeable test section that can be made open or closed depending on the experiment. The contraction of the tunnel can also be changed, having exit sections of 400x400 mm^2, 500x500 mm^2, and 600x600 mm^2. The maximum airspeed that can be achieved (with the 400x400 mm^2 exit section) is around 35 m/s, and the minimum turbulence level is about 0.5%, depending on the flow velocity [45].

The tunnel configuration used for this campaign is the closed test section, with the 600x600 mm^2 contraction. The airspeed can be controlled by changing the revolutions per minute of the fan, located after the plenum. After the plenum and the centrifugal fan, the flow is directed through the diffuser, and then enters the settling chamber. This is where the PIV seeding is introduced using an in-house designed seeder that fills the soap bubbles with a mixture of Helium and air. Next, the seeded flow enters the contraction, then a short straight tunnel nozzle, and finally the 600x600 mm^2 closed test section.

3.2.2. Test Configuration

The experimental campaign consists of a series of PIV measurements on a pitching wing. In order to perform PIV on a volume, four cameras are used. These are Photron high speed cameras, that can record at 4000 fps, although the configuration chosen uses 2000 fps, with a resolution of 1024 x 1024 pixels. The main limiting factor regarding time management during the campaign, is the internal recording memory of the cameras, of 16 GB [41]. After filling the whole memory, the images have to be saved to the acquisition PC, taking most of the available tunnel time. The selected lenses are 60 mm, allowing to focus the field of view in the center of the wing, avoiding capturing the part of the wing most affected by wall effects.

As explained in Section 3.1.2, HFSB use LED lights for PIV illumination, being shown in Figure 3.2. These are coordinated with the cameras through the PTU (Programmable Timing Unit), which is in charge of triggering the cameras and the lights adequately from the angle of attack input. During time-based acquisition, the recording starts directly after the PTU receives the trigger signal. In cyclic acquisition, the trigger signal is received to start taking pictures, but the cameras only save a determined number of images, starting from a specified amount of pictures taken after the trigger signal. For example, if 20 images are desired, starting from image number 100 after the trigger signal, the cameras will start shooting at the trigger signal, but only the 20 pictures taken after the first 100 will be stored in the memory. This allows to take multiple cycles of images at the same phase after the trigger signal.

In order to generate a trigger signal, the rotating stage is attached to an encoder. This one registers the angle of attack of the wing, and a software is used to send the trigger signal to the PTU when the stage reaches a certain angle of attack. As it will be discussed in Section 3.3, the mean angle of attack is kept at 15° for the whole campaign, and therefore this angle is chosen as the trigger point, the phase at which measurements start.

The wing model is actuated using a Zaber Rotary Stage X-RSB120AT-E08. It is a continuous, 360° stage, that can reach up to 600 rpm, with an accuracy of 0.28°. It is equipped with the encoder that registers the angle that the stage is at any point in time, and how it changes [46]. The stage is actuated using a custom made Python script that signals the device to perform a sinusoidal motion in which the mean angle of attack, amplitude, and frequency can be used. This code uses the control Python library from Zaber, it was written by Octavian Soare and Pere Valls Badia, and it can be found in Appendix A.

Figure 3.3 overlays the coordinate system used on top of the wind tunnel set-up. The x-coordinate is aligned with the flow direction, being positive when pointing downstream. The y-coordinate is aligned with the span of the airfoil model, and being defined as positive upwards, and to complete the right-handed coordinate system, the z-coordinate is perpendicular to the surface of the airfoil and the flow direction, being positive towards the cameras.

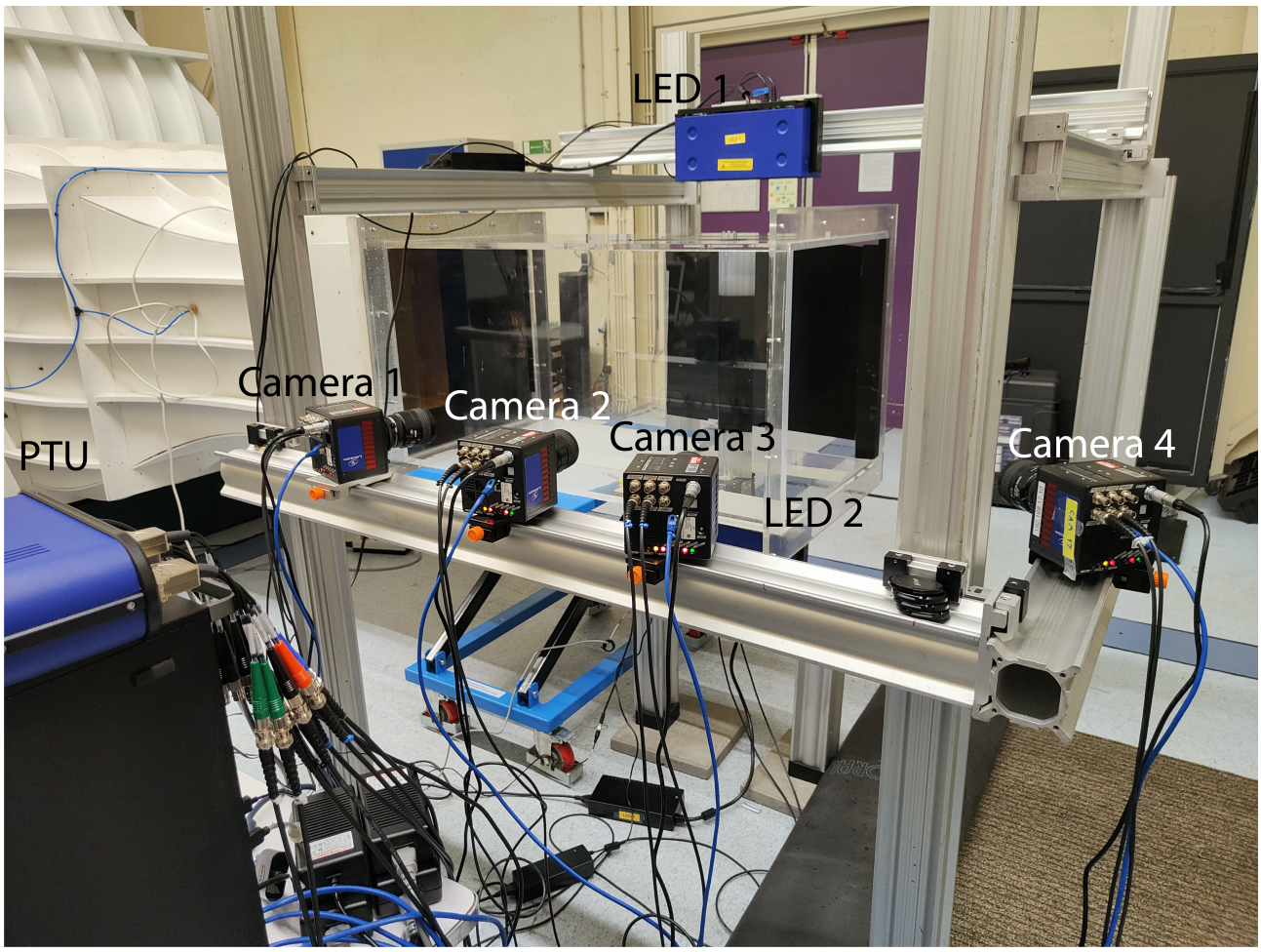

Figure 3.2: Arrangement of cameras, PTU and LEDs used during the campaign.

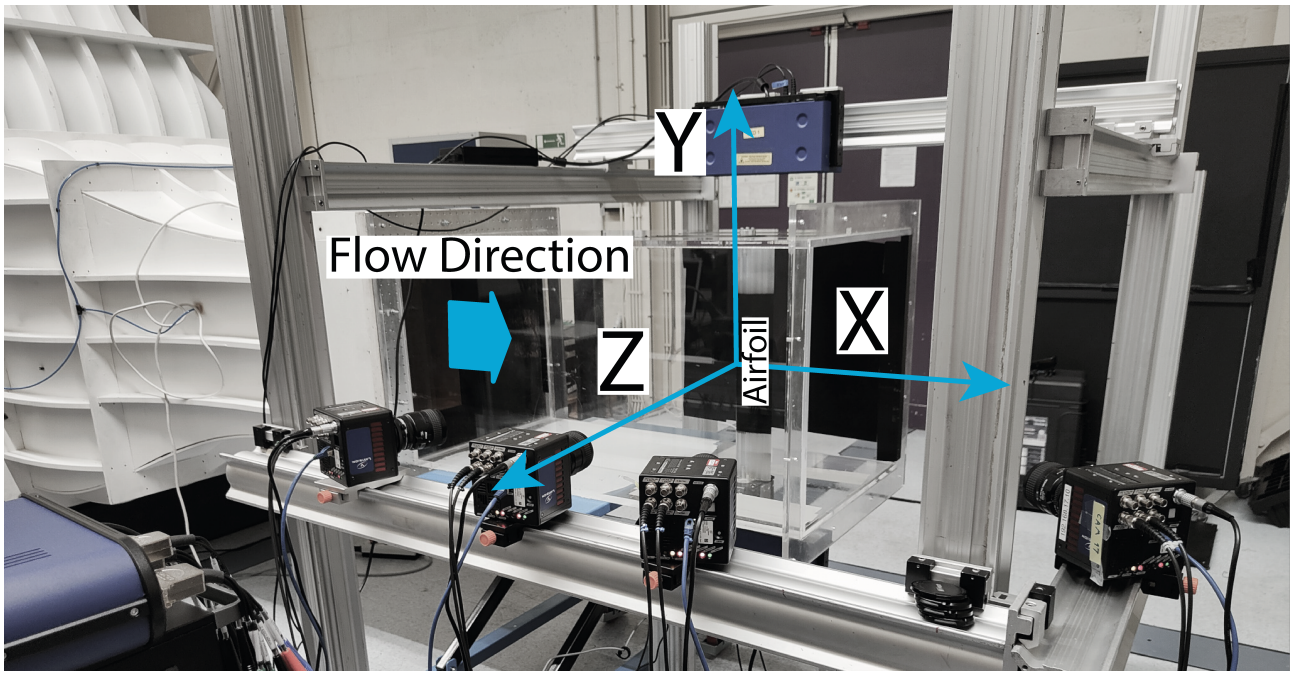

Figure 3.3: Coordinate system definition

3.3. Test Matrix & Cases

In order to guarantee an efficient use of the available wind tunnel time, a plan is made in which the cases chosen to gather data for are defined. The PIV cases are divided in two types of measurements, time-resolved and cyclic acquisition (phase-locked) measurements. First, the time-resolved measurements are taken for a particular case. Then, the phases at which relevant phenomena occurs is searched by processing some cycles and analysing the data, and they are then chosen as the phases at which the cyclic acquisition data is gathered. Further discussion on this process is given in Section 4.1. The number of cases is mainly limited by the time necessary to save the data from the RAM of the PIV cameras to the acquisition PC and the limited processing time for the project, while the amount of data gathered in each case is limited by the internal memory of the cameras (16 GB) [41].

3.3.1. Time-Resolved Measurements

The chosen time-resolved cases are given in Table 3.1, where the airfoil geometry, reduced frequency, and amplitude of the motion are the parameters that are modified.

	$\Delta\alpha = 10°$	$\Delta\alpha = 15°$
NACA 0012	$k = \frac{\pi}{50}$	$k = \frac{\pi}{50}$
	$k = \frac{\pi}{10}$	$k = \frac{\pi}{10}$
NACA 0021	$k = \frac{\pi}{50}$	$k = \frac{\pi}{50}$
	$k = \frac{\pi}{10}$	$k = \frac{\pi}{10}$

Table 3.1: Time-resolved test matrix.

In Table 3.1, the reduced frequency of $\frac{\pi}{50}$ or 0.06 corresponds to an oscillation of 1 Hz, while the reduced frequency of $\frac{\pi}{10}$ or 0.3 corresponds to a frequency of 5 Hz. These reduced frequencies give a case in the domain of highly unsteady aerodynamics (5 Hz), and another one close to the quasi-steady aerodynamics domain [47], providing two distinctive set-points for analysis. The two airfoils used have largely different thicknesses in order to study the effect of this parameter on cycle-to-cycle variations. Finally, the oscillation amplitude is also changed to study its effect on cycle-to-cycle variations.

The effect of other parameters is not studied in this project as it is out of its scope, either due to the amount of cases that can be tested within the available wind tunnel time, or due to the limitations of the facilities. One of the parameters of the later type is the airspeed V_∞. As explained in Section 3.1.1, PTV with HFSB provides less resolution than standard PIV does, and the particle density in the flow actually decreases with increasing airspeed [38]. Therefore, the campaign is limited to a freestream velocity of 5 m/s to allow for an optimal seeding in this facility. This corresponds to a low Reynolds number of around 3.4×10^4 for the experiment. Furthermore, another parameter that is not changed is the mean angle of attack α_m. This one on the other hand, remains constant through the cases due to the limited wind tunnel availability. The chosen value for α_m is 15°. This value was chosen for two reasons. Firstly, there are studies done with similar airfoils, such as the NACA 0012 [48], in which this α_m is used, allowing for comparison. Secondly, this α_m leads to deep dynamic stall on the airfoil. Deep dynamic stall is preferred over light dynamic stall as its aerodynamic effects are stronger, and therefore lead to more pronounced cycle-to-cycle variations.

3.3.2. Phase-Locked Measurements

Once the time-resolved measurements have been taken, some cycles of each frequency and airfoil can be processed in order to figure out at which phases the relevant phenomena are taking place, as it has been shown in the past that the variations only take place at the specific parts of the cycle in which the flow is separated [26]. Note that this is an approximation, since due to the cycle-to-cycle variations, the phenomena that will be described next does not always take place at the exact same phase. However, this is not a problem, since the main goal of this phase selection is only to avoid picking uninteresting cases in which the flow is fully attached and the cycle-to-cycle variations are not present. The chosen set-points are the following:

- Dynamic stall vortex begins to detach: Table 3.2.
- Dynamic stall vortex is developed: Table 3.3.
- Dynamic stall vortex breakdown: Table 3.4.

These events take place at slightly different phases when the airfoil is different, and widely different phases when the reduced frequency is different. The chosen phases for the DSV formation are shown in Table 3.2, while the ones showing the developed DSV are shown in Table 3.3, and the vortex breakdown phases are in Table 3.4. The tables give the phase in radians, as well as the image in the cycle that the acquisition of pictures

starts. For the frequency of 1 Hz, with the cameras capturing at 2000 images per second, one full cycle takes 2000 images, while for the frequency of 5 Hz, one full cycle takes 400 images. Note that, while all the specified set-points were measured, only the most relevant ones for the study are shown for the sake of conciseness.

	1 Hz	5 Hz
NACA 0012	$\frac{\pi}{10}$: Image 100 of 2000	$\frac{\pi}{2}$: Image 100 of 400
NACA 0021	$\frac{\pi}{10}$: Image 100 of 2000	$\frac{\pi}{2}$: Image 100 of 400

Table 3.2: Chosen phases for capturing DSV formation.

	1 Hz	5 Hz
NACA 0012	$\frac{3\pi}{20}$: Image 150 of 2000	$\frac{3\pi}{5}$: Image 120 of 400
NACA 0021	$\frac{7\pi}{50}$: Image 140 of 2000	$\frac{4\pi}{5}$: Image 160 of 400

Table 3.3: Chosen phases for capturing developed DSV.

	1 Hz	5 Hz
NACA 0012	$\frac{19\pi}{100}$: Image 190 of 2000 and $\frac{3\pi}{10}$: Image 300 of 2000	$\frac{17\pi}{20}$: Image 170 of 400
NACA 0021	$\frac{11\pi}{50}$: Image 220 of 2000 and $\frac{3\pi}{10}$: Image 300 of 2000	$\frac{21\pi}{20}$ Image 210 of 400

Table 3.4: Chosen phases for capturing DSV breakdown.

3.4. Post-Processing

After the experimental campaign has been completed and the data has been gathered, it is to be processed using the commercial software DaVis. DaVis includes a collection of tools for PIV processing, and can export the velocity field to a visualization software such as Paraview, Tecplot, or a MATLAB script. In this section the operations performed using DaVis in order to process the images from the camera are explained. In this project, a MATLAB script is used in which all the different figures are created from the matrices that are extracted from the DaVis product files. These matrices are obtained using a piece of code provided by fellow student Pere Valls Badia.

3.4.1. Background Subtraction

The first process to be ran on the raw camera images is the so called background subtraction. This is done to remove any undesired object from behind the scene that superimposes the desired signal [49]. In the context of the experiment, the background subtraction operation removes shinning objects that may be behind the tunnel, reflections of the airfoil model, foam from the HFSB on the surface of the airfoil, etc. The operation works as a filter in which the number of images to be used for it is specified. In this case, 5 images were used. The specified number of images is taken around a certain image to filter it. The algorithm works by subtracting the minimum value of each pixel in these 5 images, filtering out the background, and leaving only the particles.

3.4.2. Shake-the-Box

This operation uses the algorithm explained in Section 3.1.4 to obtain the trajectories followed by the particles (HFSB) during the measurements. These trajectories are called tracks, and represent the path that each particle follows in both time and space. Is this close relationship with time that leads to the algorithm be considered a 4D-PTV method [42], but in this report it is referred to as shake-the-box.

In order to perform this operation, the main parameters to be controlled are the size of the domain volume, the particle detection parameters, and the tracking velocities. The size of the volume needs to be big enough to encapsulate the whole study domain, with the only limitation being the computational time increase that may come when processing a larger volume. The particle detection has some measures to control how easy it is to detect a particle. Here, the threshold for 2D particle detection was set between 350 and 450 counts, depending on the quality of the specific data set being processed, and the triangulation error was set to 0.5. A lower threshold and a larger error would result in a larger number of tracks detected, but it could introduce too many ghost particles, so a balance is to be found. Finally, the tracking velocities should provide the range of velocities that the particles can take for u, v, and w. For u, a velocity of 2 ± 15 voxel is given, for v of 0 ± 8 voxel is set, and for w 0 ± 9 voxel (in DaVis, the velocity range can also be given in meters per second, but in this case, the aforementioned ranges were given in voxels).

3.4.3. Binning

Once the particle tracks are obtained, in order to be able to perform operations on them, it is useful to convert them to a matrix of values instead of an array of trajectories. This is done trough the binning operation, that takes a certain number of images, for this study 20, and combines them into an averaged flow field. Since the images are sampled at a high rate of 2 kHz, combining 20 of these images, which corresponds to $\frac{1}{100}$ or $\frac{1}{20}$ of a cycle, for 1 Hz and 5 Hz respectively, leaves enough temporal accuracy for this study, but the number of images could be reduced for applications that would benefit from it. The results are arrays of three dimensions containing the value of a certain quantity at each point in space. For example, the resulting array for u contains the value that the u velocity takes at each point of the domain. Some points may be left blank as the experimental data may have regions of a lower particle density, or at the limit of the domain where the particles start to become out of focus, or in the region shadowed by the airfoil, where the particles are covered by the wind tunnel model and there is no optical access.

In order to perform the binning, a sub-volume size is to be chosen, that gives the resolution of the resulting data. 56 voxel is the chosen size, which corresponds to 1.3 mm^3, and allows to study the vortical structures of the flow. Other applications that require the investigation of small-scale structures or turbulence may require a smaller sub-volume size, although in those cases, the PTV with HFSB may not be the best technique to be chosen due to its lower resolution with respect to standard PIV. The overlap is also to be chosen. While in standard PIV, the overlap refers to the percentage of an interrogation window that is combined with the adjacent one, in this case it refers to the percentage of each sub-volume instead. Overlap is used to increase the amount of data points, creating smoother data visualization, and to average out the noise from the results [36]. An overlap of 75% is chosen for the binning.

4. Results & Discussion

4.1. Time-Resolved Results

In this section, time-resolved measurements are presented for the main cases being studied. These allow to analyze the flow evolution within a cycle, and to choose the phases of the cyclic acquisition measurements presented in Section 4.2. The limited memory of the PTV cameras only allowed for a few seconds of time-resolved footage to be captured for each measurement, and therefore not enough cycles could be acquired for statistical analysis of cycle-to-cycle variations using time-resolved data. Taking this into account, this section focuses on giving an overview of the dynamic stall cycle, specially of the cases being studied as part of the research. Figure 4.1 shows the flow evolution along the phase. The images are shown in a more clear format in Figure 4.2, representing slices of the u velocity at the mid-span of the measurement domain. On the other hand, slices of the vorticity ω_y are shown in Figure 4.3. These clearly show a conventional dynamic stall cycle, following the stages explained in Section 2.1 [22]. Figure 4.2 **a)** and **b)** for u, and Figure 4.3 **a)** and **b)** for ω_y show the attached stage of the flow, with a flow field close to what is expected in a static case, including a peak of velocity on the suction surface near the leading edge, followed by what corresponds to an adverse pressure gradient, and a trailing edge wake that can be seen easily from a trace of negative vorticity. The onset of dynamic stall occurs at $\theta = \frac{\pi}{2}$ (see Figure 4.2 **c)** for $u(x, z)$ and Figure 4.3 **c)** for ω_y), or slightly before. Since these images correspond to a phase of $\frac{\pi}{2}$ and in deep dynamic stall conditions, like the present, the onset of dynamic stall takes place before the maximum angle of attack, it can be expected that dynamic stall has already started. This is further supported by Figure 4.3 **c)**, which clearly shows the DSV, visible through a long region of high vorticity, detaching from the surface. Figure 4.2 **d)** to **f)** for u and Figure 4.3 **d)** to **f)** for ω_y correspond to the stalled stage. For the images corresponding to a phase of $\frac{\pi}{2}$, it is likely that the lift is overshooting the maximum lift for the static stall case, as the DSV is over the surface of the airfoil, and as a low pressure region, it can be increasing suction locally. On the other hand, the other images in the stalled stage are probably experiencing a drop in load. Re-attachment is taking place in Figure 4.2 **g)** and **h)** for u, and Figure 4.3 **g)** and **h)** for ω_y, right before the cycle ends.

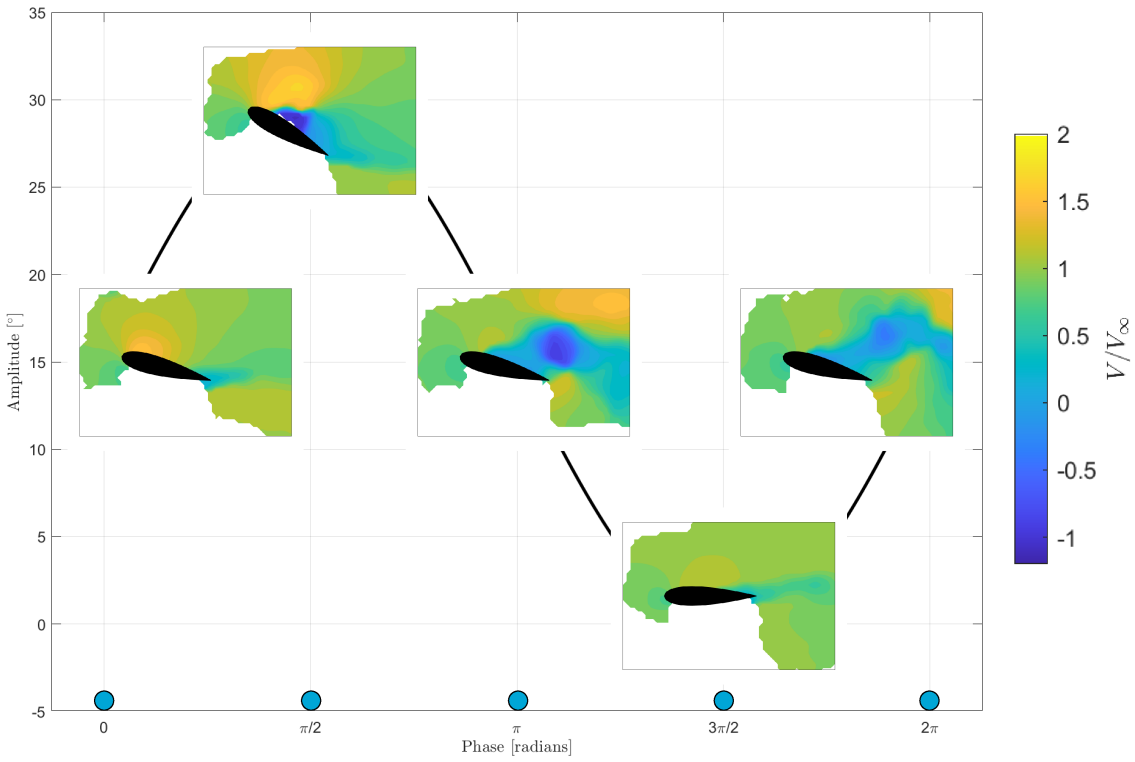

Figure 4.1: Slices of $u(x, z)$ at the mid-span along a cycle for the NACA 0021, 5 Hz, 15° amplitude case

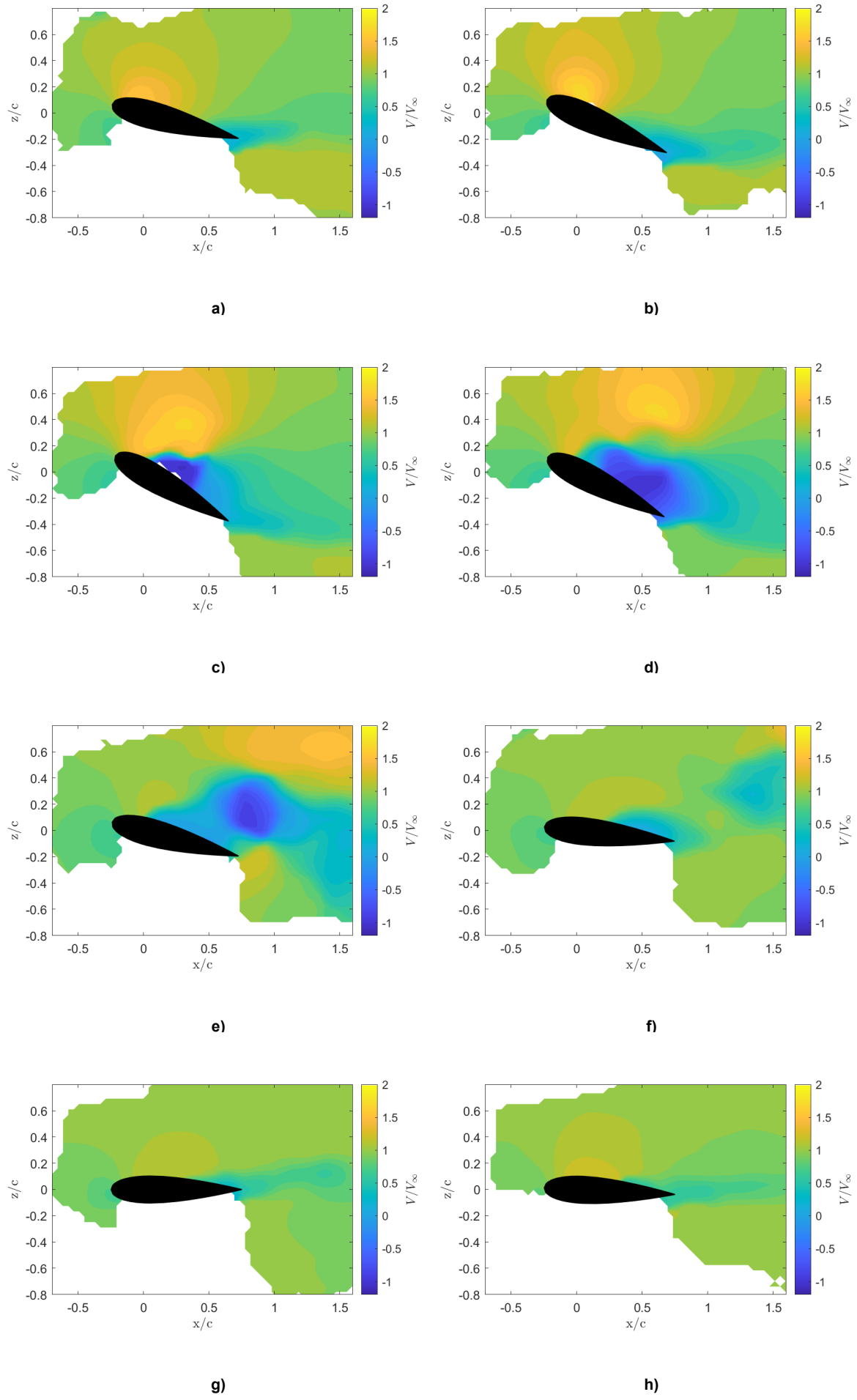

Figure 4.2: Slice of $u(x, z)$ at the mid-span for **a)**: $\theta = 0$, **b)**: $\theta = \frac{\pi}{5}$, **c)**: $\theta = \frac{\pi}{2}$, **d)**: $\theta = \frac{7\pi}{10}$, **e)**: $\theta = \pi$, **f)**: $\theta = \frac{6\pi}{5}$, **g)**: $\theta = \frac{3\pi}{2}$, and **h)**: $\theta = \frac{17\pi}{10}$.

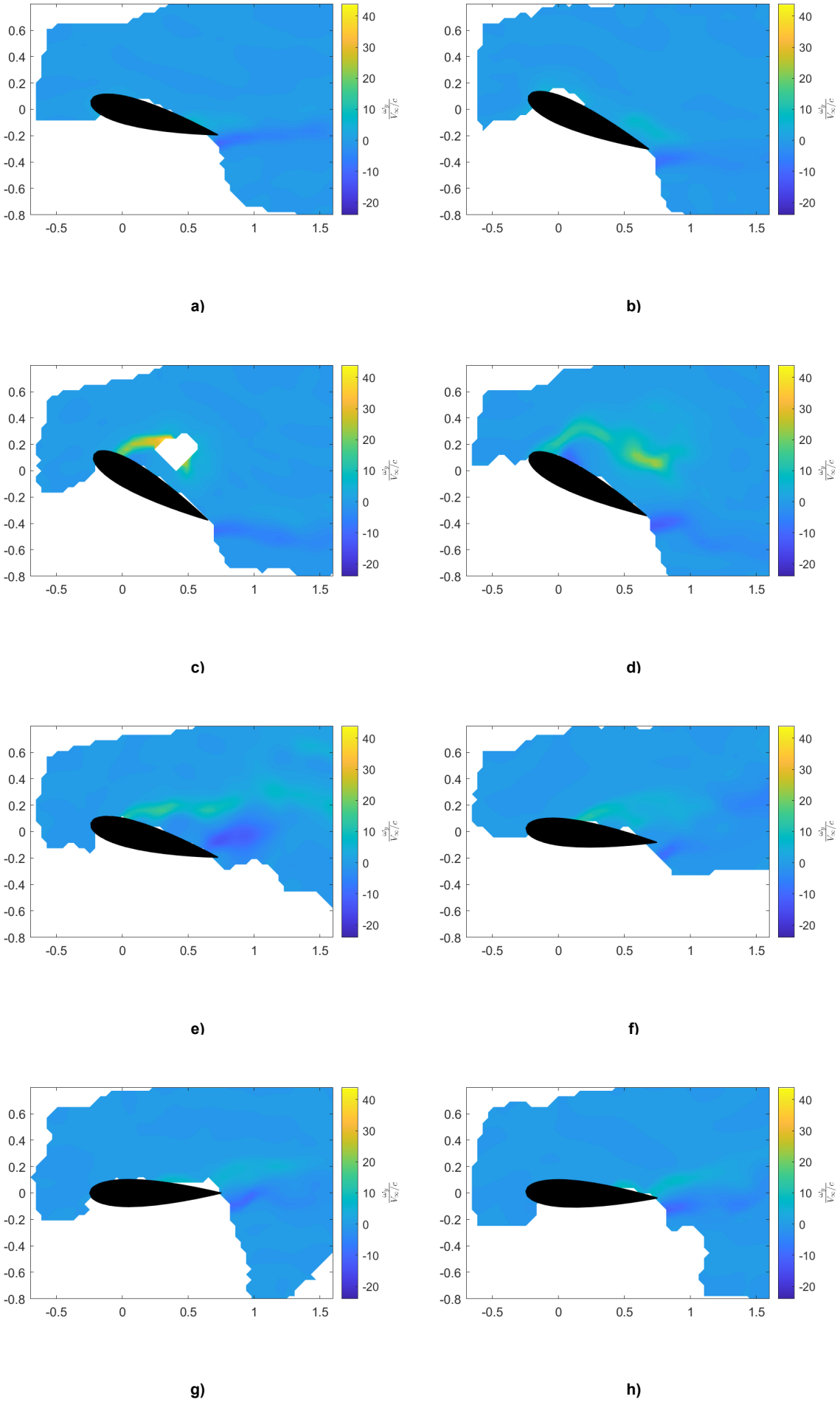

Figure 4.3: Slice of $\omega_y(x,z)$ at the mid-span for **a)**: $\theta = 0$, **b)**: $\theta = \frac{\pi}{5}$, **c)**: $\theta = \frac{\pi}{2}$, **d)**: $\theta = \frac{7\pi}{10}$, **e)**: $\theta = \pi$, **f)**: $\theta = \frac{6\pi}{5}$, **g)**: $\theta = \frac{3\pi}{2}$, and **h)**: $\theta = \frac{17\pi}{10}$.

Other case studies are presented in Figure 4.4, Figure 4.5, and Figure 4.6, corresponding to the NACA 0021 5 Hz 10° amplitude case, the NACA 0021 1 Hz 15° amplitude case, and the NACA 0012 5 Hz 15° amplitude case respectively. The measurements show the trends expected from dynamic stall [1, 22] and airfoil theory [7]. First, the comparison of Figure 4.1 and Figure 4.4 shows what happens in the dynamic stall cycle when reducing the amplitude of the motion. The lower amplitude leads to separation occurring earlier than $\frac{\pi}{2}$, due to the earlier deceleration of the airfoil. However, the subsequent separated stage is more violent for a larger amplitude. This is a consequence of the faster pitching rate, which while it helps the flow stay attached for a bit longer due to the faster relative motion with respect to the flow, it also leads to a more dramatic stalled state.

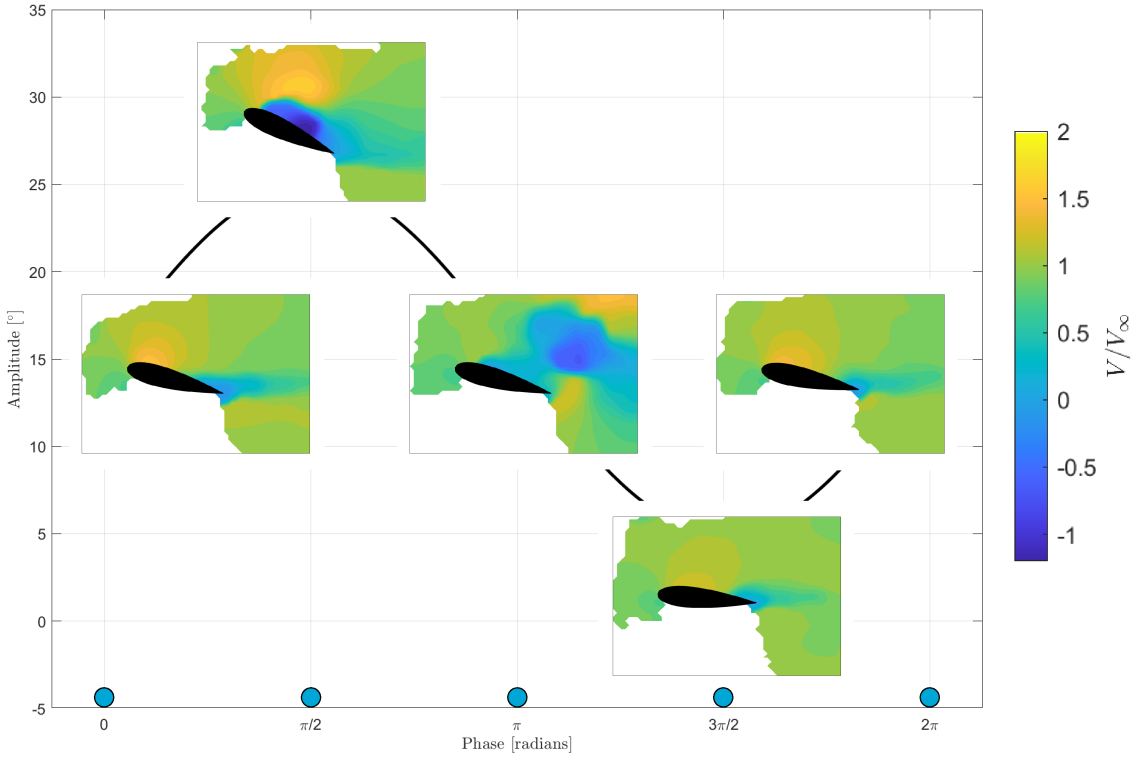

Figure 4.4: Slices of $u(x, z)$ at the mid-span along a cycle for the NACA 0021, 5 Hz, 10° amplitude case.

A similar comparison can be made for the case of the airfoil pitching at 1 Hz. The lower frequency leaves the airfoil closer to a quasi-steady aerodynamic state, as opposed to the highly unsteady 5 Hz frequency. Consequently, the separation process at 1 Hz is closer to what it would be expected to happen in the static case [7], with a lower lift overshoot expected and a seemingly weaker DSV. The separation bubble is still present, but the stall intensity and load fluctuations is expected to be lower. On the other hand, the thinner airfoil cycle in Figure 4.6 behaves as expected from airfoil theory [7], separating earlier and with a more violent stalled state, because the flow finds more difficulty staying attached to a thinner airfoil.

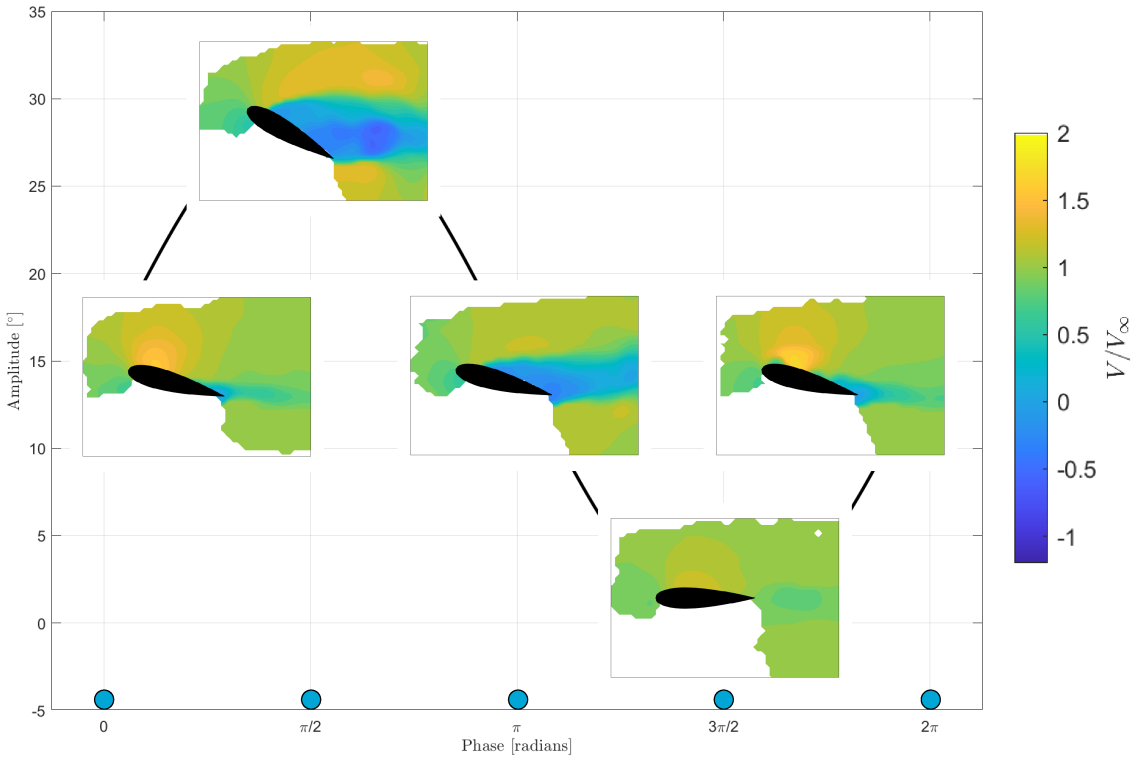

Figure 4.5: Slices of $u(x, z)$ at the mid-span along a cycle for the NACA 0021, 1 Hz, 15° amplitude case.

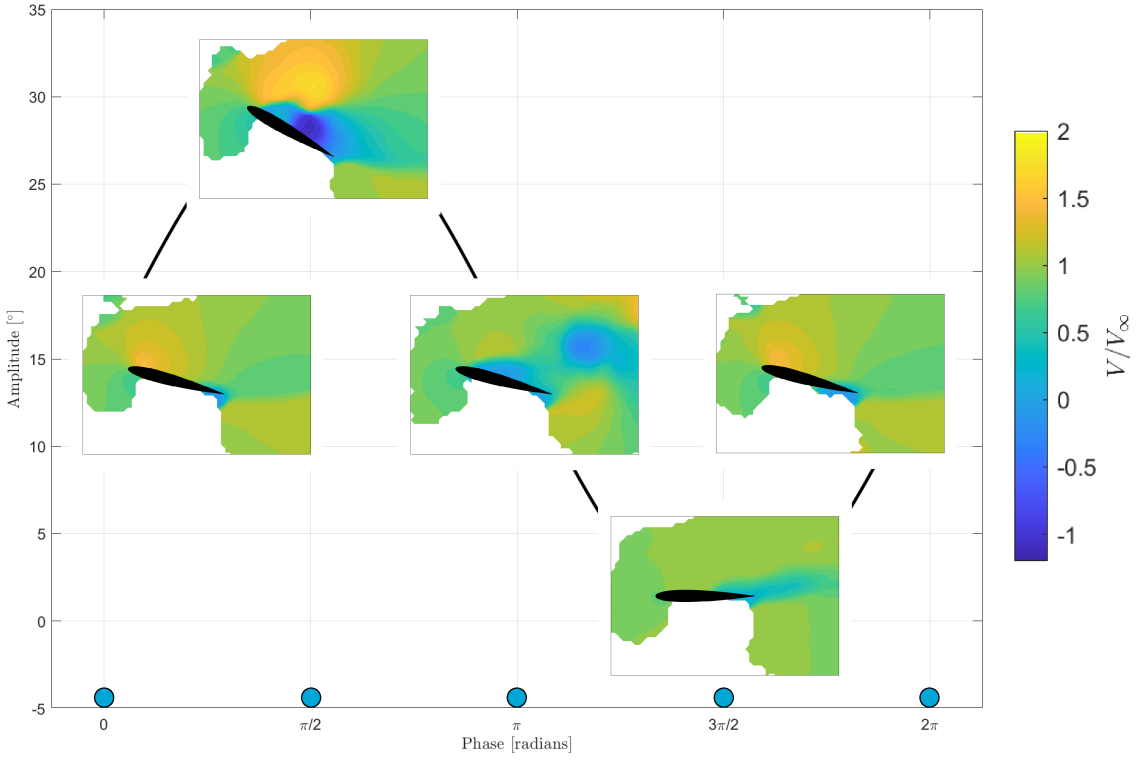

Figure 4.6: Slices of $u(x, z)$ at the mid-span along a cycle for the NACA 0012, 5 Hz, 15° amplitude case.

4.2. Phase-Locked Results

In this section, phase-locked measurement results are presented, together with some of the main outcomes of the research. For the sake of simplicity and organisation, only the results from the NACA 0021 airfoil at 5 Hz, with an amplitude of 15° are presented, captured at a phase of $\frac{\pi}{2}$ in the cycle, unless it is specified that the conditions are different. Further cases will be presented and compared in Section 4.3. The choice of this case comes from the airfoil pitching at 5 Hz and an amplitude of 15° being the most unsteady of the measured cases, leading to the most prominent stall structures in the flow. The phase chosen corresponds to an angle at which the flow is starting to separate, but since it is not fully stalled, it allows for better analysis. This section is focused on the study of the cycle-to-cycle variations.

4.2.1. Definitions

In order to perform the analysis, some definitions are first to be established. These will be used to study the averaged flow, and later in Section 4.2.2 to look into the flow variations statistically. Equation 4.1 breaks down the measured u velocity into different quantities for its analysis, and provides their notation. Variables x, z, and θ are omitted from the expression because they do not vary in the averaging process and are present in all the terms. The meaning of each of the terms is the following:

$$u(x, y, z, i, \theta) = u(y, i) = U + \bar{U}(y) + \tilde{U}(i) + u'(y, i) \tag{4.1}$$

- $u(y, i)$: Measured quantity at a specific point in space and time.
- U: Double average of the u velocity, along the span (y) and in phase (i).
- $\bar{U}(y)$: Variation in the phase-averaged values at a specific spanwise location. The average in span of $\bar{U}$ is 0.
- $\tilde{U}(i)$: Variation in the span-averaged values for a specific cycle. The average of $\tilde{U}$ for all cycles is 0.
- $u'(y, i)$: Residual, 'clean' fluctuations, dependent on both y and i (and the rest of the parameters). Both the phase and span averages of u' should be 0.

These definitions are further clarified using Figure 4.7. The contour plot shows y-aligned lines of u at point $x = -8.26$ mm and $z = 18.28$ mm, shown in Figure 4.8, for all of the 250 measured cycles. The existence of time-dependent chord-scale modes can already be seen, with the areas of low/high velocity being preserved over the cycles. The left plot shows the values that $\bar{U}$ takes along the span, while the bottom plot shows the values that $\tilde{U}$ takes as cycles progress. $\bar{U}$ is the average of u along each horizontal slice of the contour plot, while $\tilde{U}$ is the average along each vertical slice.

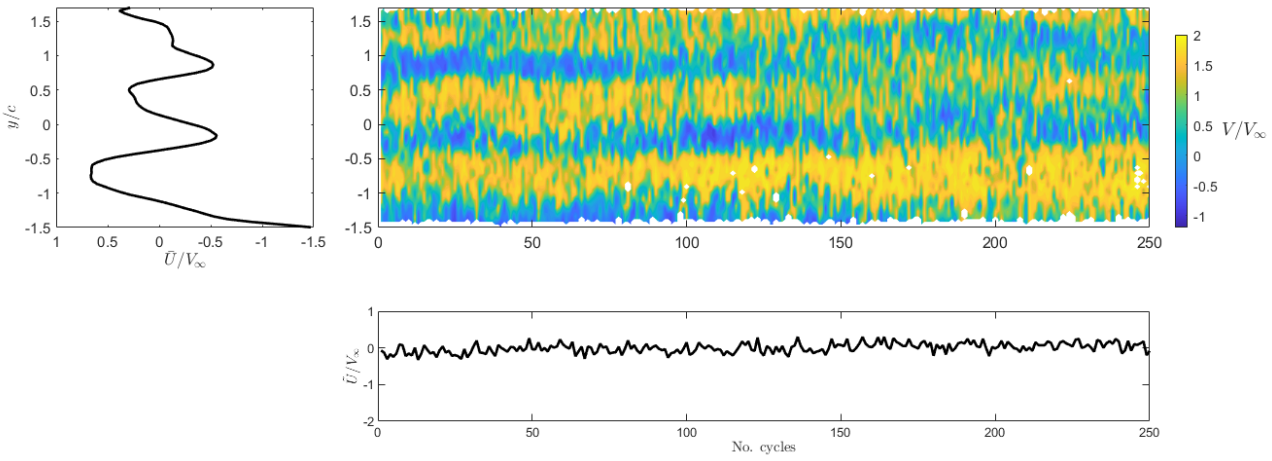

Figure 4.7: Representation of $\bar{U}$ and $\tilde{U}$ for the NACA 0021, 5 Hz, 15° amplitude case.

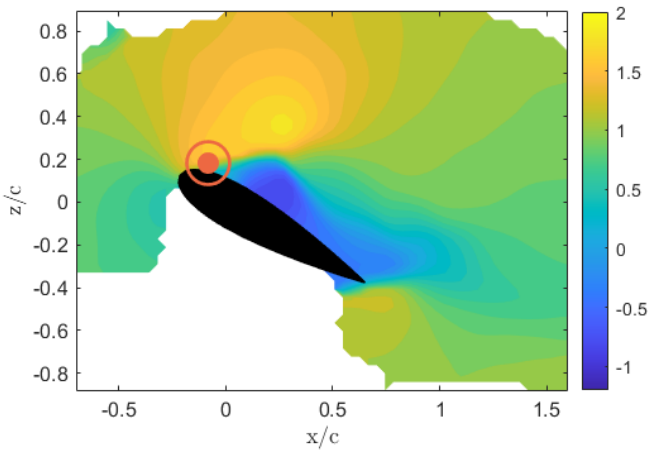

Figure 4.8: Location of the line shown in Figure 4.7, where x=-8.26 mm and z=18.28 mm.

To start the analysis, shown below there are different representations of the phase-average over 250 cycles of the aforementioned case. While in Figure 4.9 **a)**, the double average U is shown, Figure 4.9 **b)**, **c)**, and **d)** represent y-aligned slices of the phase-averaged volume.

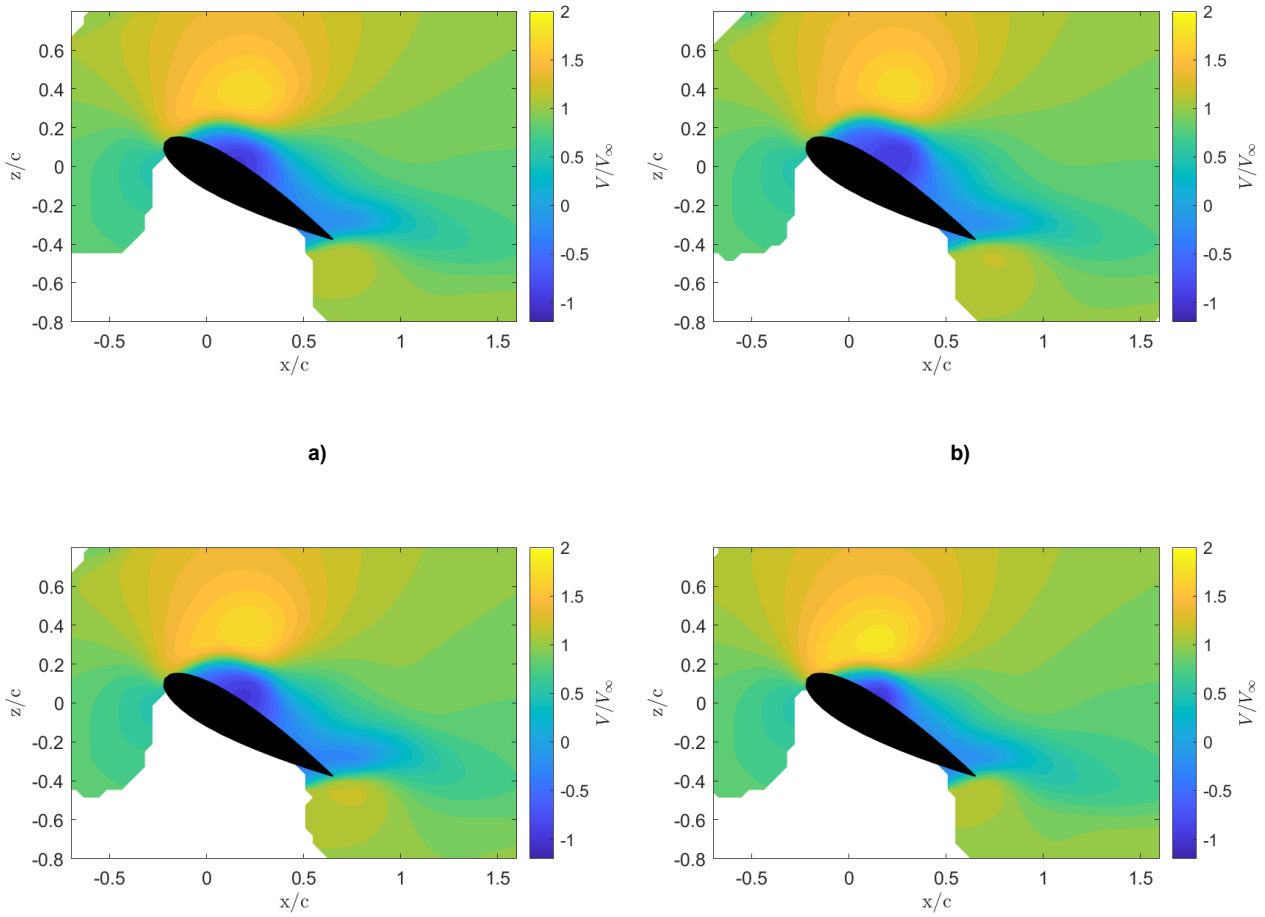

a) **b)**

c) **d)**

Figure 4.9: a): Phase and span averaged U velocity field, and phase averaged $(U + \bar{U})$ velocity field at **b)**: 25% of the span, **c)**: 50% of the span, and **d)**: 75% of the span.

It can be seen that the slices at different points of the span look relatively different, specially in terms of the shape of the separated region. In fact, in Figure 4.9 **d)** it can be seen that the separated region at the leading edge is noticeably smaller. Now, these slices can be compared with an average over the span of the flow for each cycle, shown in Figure 4.10 for cycles number 1, 25, 50, 75, and 100. These figures look similar between cycles, with some small differences in the values in the separated region close to the leading edge, and the values in the separation bubble of cycle 50, but keeping a very similar shape of the separation bubble. Not only that, but they are also very close to the slices of the phase-averaged results $(U + \bar{U})$, and specially of the double average U. Looking back to Figure 4.7, it was seen that $\bar{U}$ has a larger variation than $\tilde{U}$. Since the span average is expressed as $U + \tilde{U}$, and the phase average as $U + \bar{U}$, it makes sense that the span average barely changes from the double average U. The implications of this are important, as with the resulting flow-field being somewhat different between phase-averaged slices, while being similar to the averages along the span, further analysis is required to establish the relationship between cycle-to-cycle variations and spanwise flow variations.

Figure 4.9 **a)** and the individual cycles from Figure 4.10 being so similar starts hinting towards the spanwise variations influencing cycle-to-cycle variations, as when averaging the phase average in span, the results look very similar to individual cycles, while individual slices of the phase average look quite different between each other. This can be further explored by visualizing the spanwise vorticity (ω_y). While Figure 4.11 **a)** shows the span averaged, phase averaged vorticity flow field, Figure 4.11 **b)** to **f)** shows the span average of the vorticity for cycles 1, 25, 50, 75, and 100 respectively. Again, the plot with the phase average shows a similar pattern as those in which the span average is dominating, indicating the relationship between cycle-to-cycle variations and spanwise variations, also for the vorticity. The flow is shown to have a high vorticity region over the airfoil, corresponding to the DSV. At the current phase, the DSV is formed right at the leading edge of the airfoil, with only a smaller region of lower vorticity slightly downstream that can be a separation bubble. Furthermore, all the cycles show a region of negative vorticity behind the airfoil, corresponding to a trailing edge vortex. The shape of these regions is remarkably similar between the span averages of each cycle. Note how the core of the DSV contains the highest vorticity consistently through the cycles, followed by a thin region with slightly lower vorticity than the core that traces a curve from the core of the DSV to the leading edge of the airfoil.

A similar figure to the contour plot in Figure 4.7 can be done for u' instead of u. Shown in Figure 4.12, this contour represents the evolution of the fluctuations in the measured velocity over time for $(x, z) = (-8.26, 18.28)$. In Figure 4.12, the modes are still present, just like in Figure 4.7. The fact that the residual spanwise modes remain suggests that the existence of these states is independent of the span and phase averages, pointing towards an external factor, like the HFSB foam accumulation (Section 4.2.3) being the cause. While this being the dominating explanation, it is also feasible that the intensity of the u' fluctuations is different between each of the spanwise modes, so that u' experiences more variation in the separated patches than on the attached ones. However, from Figure 4.12 this seems less impactful.

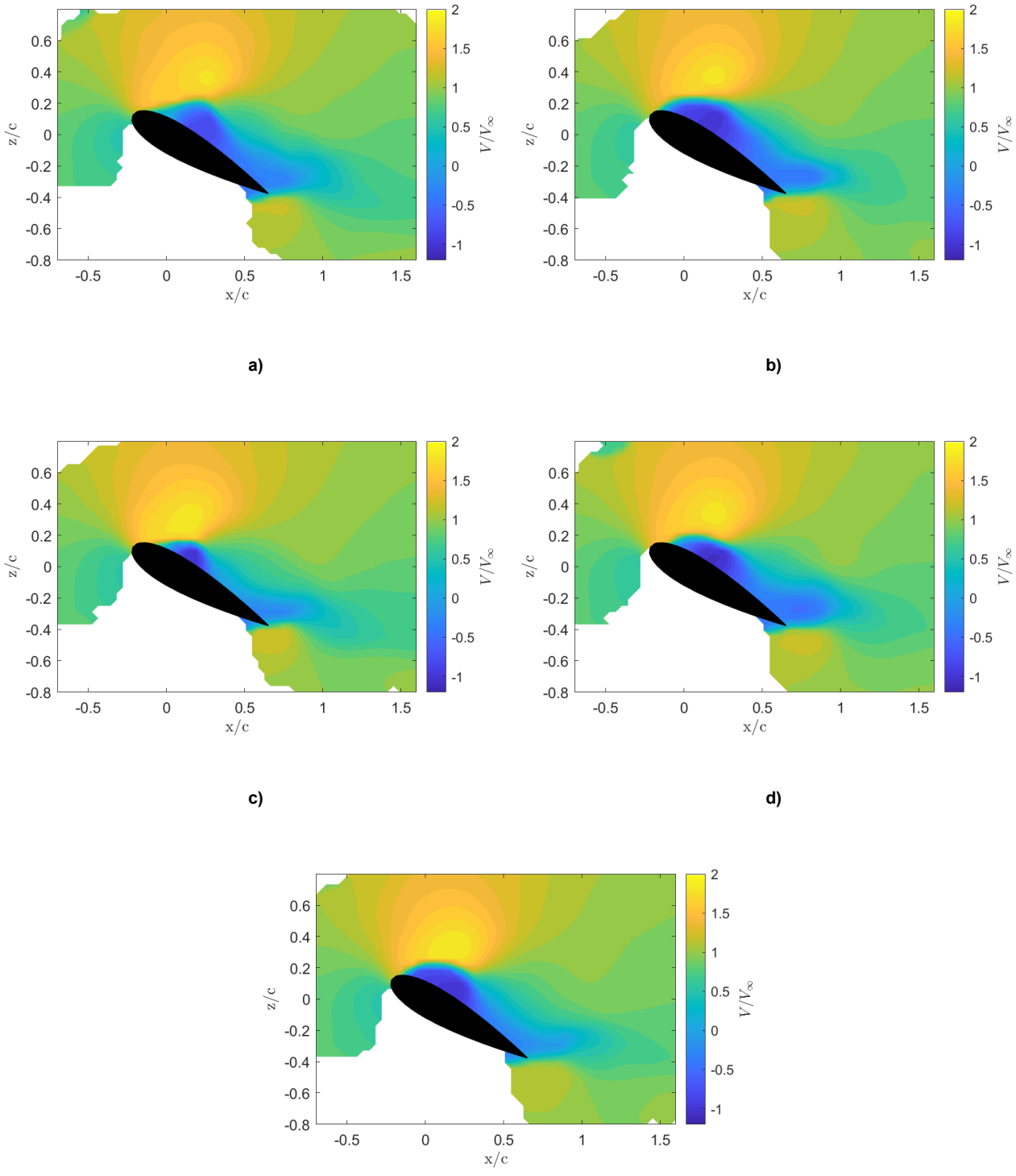

Figure 4.10: Span averaged $(U + \bar{U})$ velocity field for cycles **a)**: 1, **b)**: 25, **c)**: 50, **d)**: 75, and **e)**: 100.

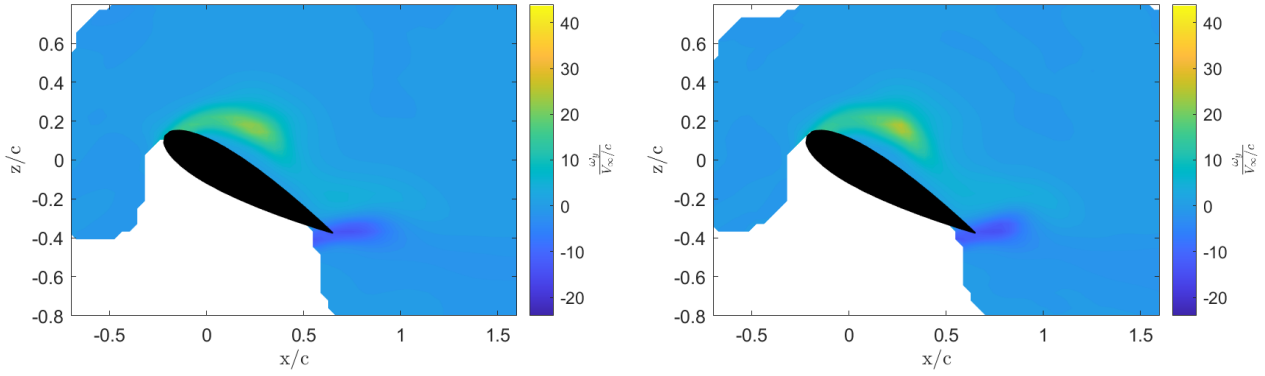

a) **b)**

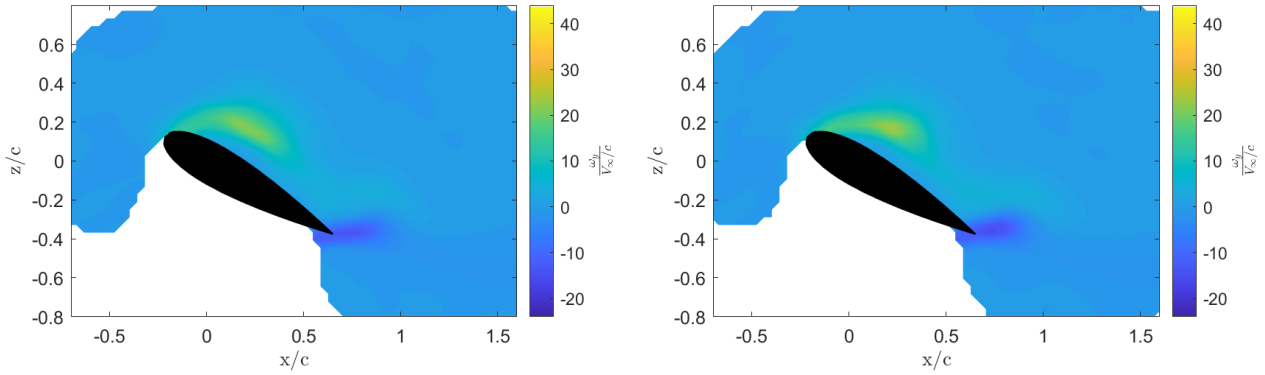

c) **d)**

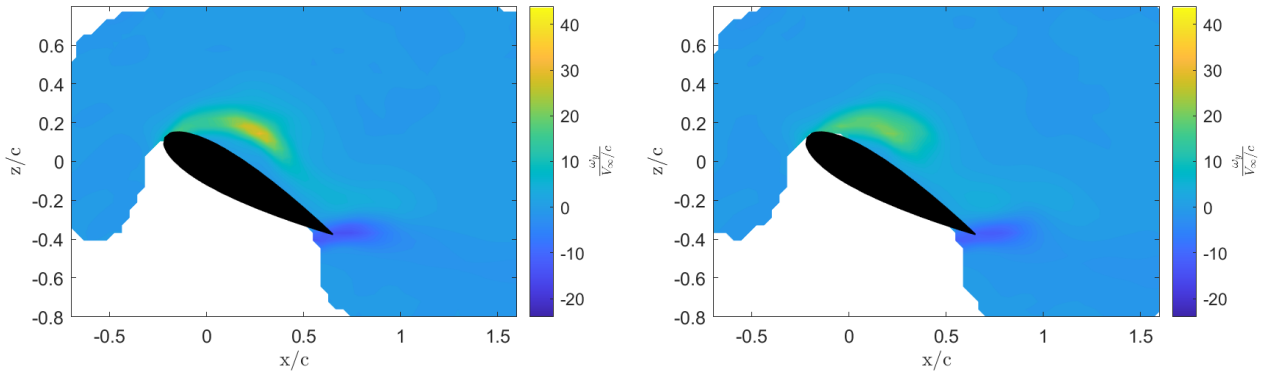

e) **f)**

Figure 4.11: a): Phase and span averaged vorticity field, and span averaged vorticity field for cycles **b)**: 1, **c)**: 25, **d)**: 50, **e)**: 75, **f)**: 100.

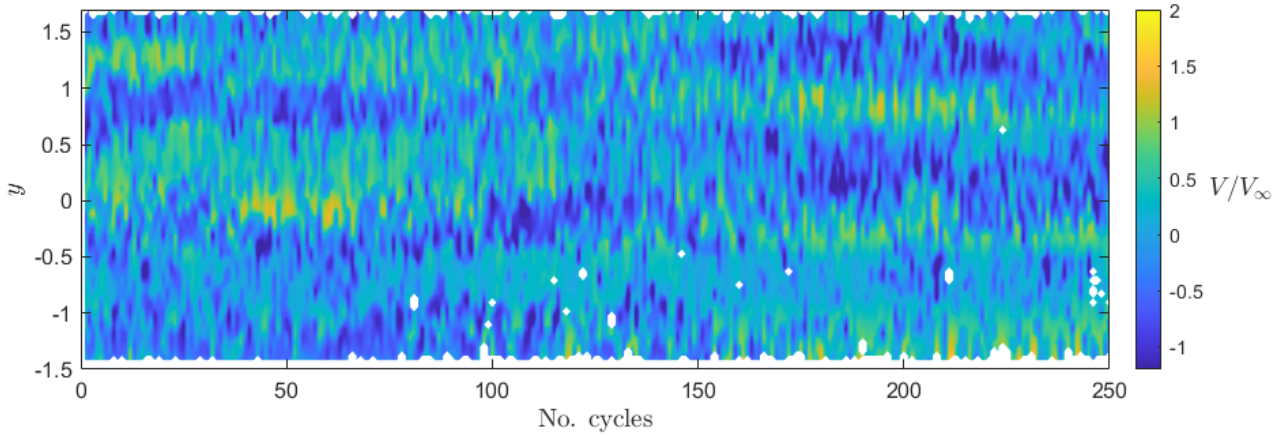

Figure 4.12: Representation of the time evolution of u' at $(x, z) = (-8.26, 18.28)$ for the NACA 0021, 5 Hz, 15° amplitude case.

4.2.2. Variances

With a relationship between cycle-to-cycle variations and spanwise variations established, next, the extent of these variations is to be studied. In order to do this, the following variance definitions are given. Equation 4.2 is the variance (σ^2) at a certain spanwise location y of the measured values with respect to the phase average (at that location). It is therefore a measure of the cycle-to-cycle variations. On the other hand Equation 4.3 is the variance at a certain cycle i of the measured values with respect to the span average (of that cycle). This is therefore a measure of the spanwise variations.

$$\sigma^2(u'(y,i) + \tilde{U}(i)) = \frac{1}{N_i} \sum_{i=i_0}^{i=i_{max}} \left(u(y,i) - (U + \bar{U}(y))\right)^2 \tag{4.2}$$

$$\sigma^2(u'(y,i) + \bar{U}(y)) = \frac{1}{N_y} \sum_{y=y_0}^{y=y_{max}} \left(u(y,i) - (U + \tilde{U}(i))\right)^2 \tag{4.3}$$

Analysing these parameters allows to quantify the cycle-to-cycle variations and the spanwise variations. In order to do this, the averages of Equation 4.2 and Equation 4.3 are plotted following their definitions. Starting with the comparison of the variance in phase with the variance in span, from Figure 4.13 and Figure 4.14 it can be seen that the results show a similar pattern. The variance at the leading edge is the highest due to the presence of the DSV, which causes the largest changes in the velocity field, both in span and in phase. The trailing edge vortex also creates a region of high variance at the trailing edge, having again the same shape both for the span and phase variances. However, the value of these variances is remarkably different. Figure 4.14 shows a region with higher values, which reaches variances as high as four times larger than those in the average of the variance with respect to the phase average.

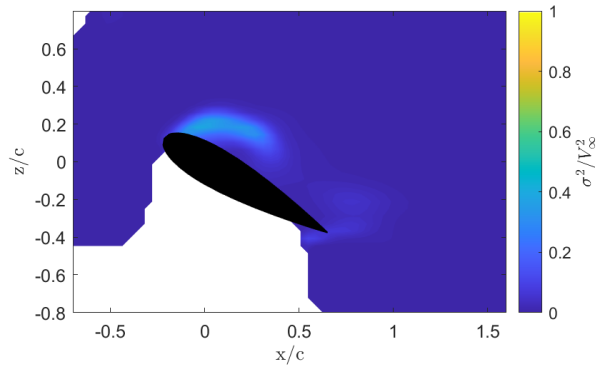

Figure 4.13: Span average of $\sigma^2(u'(y,i) + \tilde{U}(i))$.

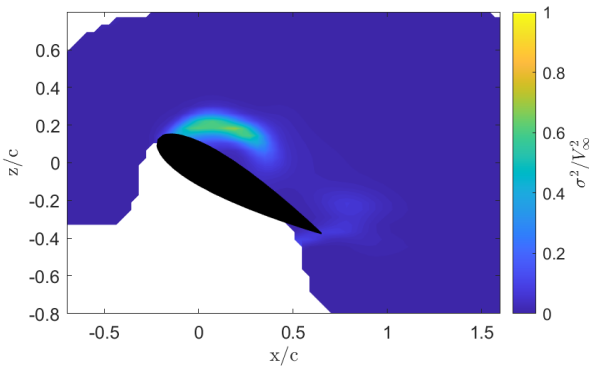

Figure 4.14: Average between cycles of $\sigma^2(u'(y,i) + \bar{U}(y))$.

Despite a specific slice of the variance in phase, as the ones in Figure 4.15, having different variance values from those of the mean shown in Figure 4.13, specific points along the span can reach variances as high as the values from the variances in span (Figure 4.14). The fact that Figure 4.13 and Figure 4.14 present similar patterns, despite the possible differences in magnitude, implies that cycle-to-cycle variations are mainly the manifestation of spanwise in-homogeneity within a cycle. Figure 4.15 shows the variance in u with regards to the phase-averaged mean value $(U + \tilde{U})$ at a given $(x,\ z)$ slice. They could be taken as representations of the 2D PIV that has been used in the past to study cycle-to-cycle variations, and the images presenting similar values to Figure 4.13 confirm that cycle-to-cycle variations are a result of structures shuffling along the span. The spanwise variations being significantly larger on average than the cycle-to-cycle variations, implies that the use of 2D PIV is not sufficient for a complete characterization of dynamic stall. This matches the results from Snortland et al [33], as they observed that in a 2D PIV slice, the cycle-to-cycle variations were significant. However, when measuring the aerodynamic load distributed along the whole wing, these variations seemed to fade. If cycle-to-cycle variations are explained as the shuffling of aerodynamic structures along the span, then over a long enough wing, the load distribution throughout the whole span will not experience cycle-to-cycle variations, as the variations in a 2D plane will be taken out along the span.

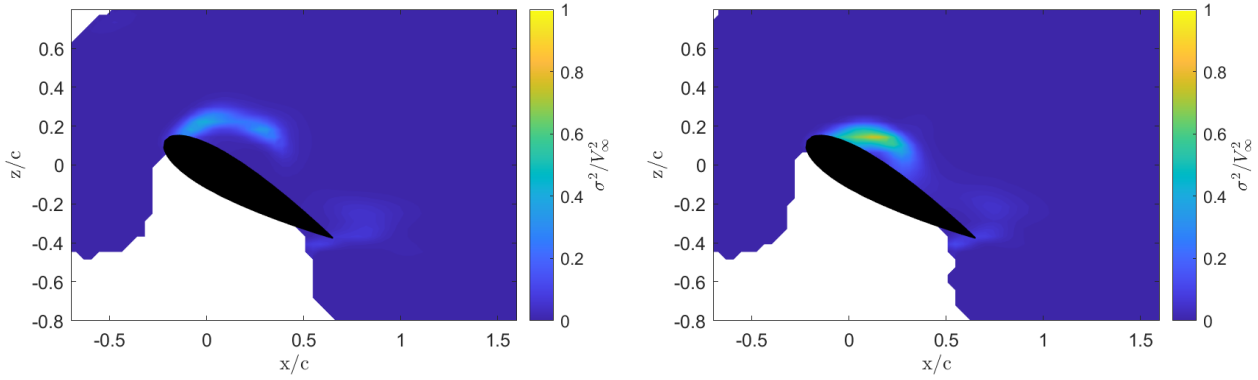

a) **b)**

Figure 4.15: $\sigma^2(u'(y,i) + \tilde{U}(i))$ at **a)**: 25% of the span and **b)**: 75% of the span.

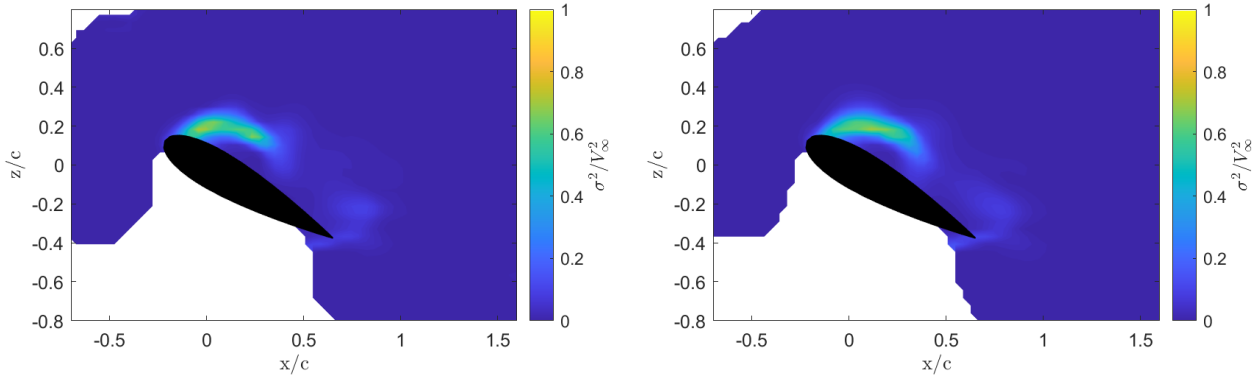

a) **b)**

Figure 4.16: $\sigma^2(u'(y,i) + \bar{U}(y))$ for **a)**: cycle number 1 and **b)**: cycle number 50.

Looking at the variance in span of individual cycles, like those in Figure 4.16, it can be seen that the regions of high variance are very similar between cycles, both in terms of value, size, and shape. This shows again the relationship between spanwise and phase variations, with the differences in value between the span variances and the phase variances clearly showing that the variations along the span are larger than the cycle-to-cycle variations.

With this in mind, the following definitions are given in order to study the homogeneity of the cycle-to-cycle variations and the spanwise variations. Equation 4.4 gives an expression for the variances of $\bar{U}$ from the definition of variance itself, while Equation 4.5 does the same for $\tilde{U}$. In these μ_{phase} and μ_{span} are the phase and span averages of the quantity in brackets, respectively.

$$\sigma^2(\bar{U}(y)) = \frac{1}{N_y}\sum_{y=y_0}^{y=y_{max}}[\bar{U}(y) - \mu_{span}(\bar{U}(y))]^2 = \frac{1}{N_y}\sum_{y=y_0}^{y=y_{max}}\bar{U}(y)^2 \tag{4.4}$$

$$\sigma^2(\tilde{U}(i)) = \frac{1}{N_i}\sum_{i=1}^{i=N_i}[\tilde{U}(i) - \mu_{phase}(\tilde{U}(i))]^2 = \frac{1}{N_i}\sum_{i=1}^{i=N_i}\tilde{U}(i)^2 \tag{4.5}$$

Since the the averages of $\bar{U}$ and $\tilde{U}$ are always 0, the variance is just the sum of the squared values of $\bar{U}$ and $\tilde{U}$ respectively, divided by the number of elements. Using the definitions for $\bar{U}$ and $\tilde{U}$, these variances can be computed as follows:

$$\frac{1}{N_y}\sum_{y=y_0}^{y=y_{max}}\bar{U}(y)^2 = \frac{1}{N_y}\sum_{y=y_0}^{y=y_{max}}[\mu_{phase}(u(y,i)) - U]^2 \tag{4.6}$$

$$\frac{1}{N_i}\sum_{i=1}^{i=N_i}\tilde{U}(i)^2 = \frac{1}{N_i}\sum_{i=i}^{i=N_i}[\mu_{span}\left(u(i)\right) - U]^2 \tag{4.7}$$

Equation 4.6 therefore represents the mean variation of the phase average of u along the span. In other words, it is how much, on average, the phase average varies along the span. On the other hand, Equation 4.7 is the mean variation of the span average of u between cycles. This means how much, on average, the span average (of each cycle) varies between cycles. These can therefore be used as measures of homogeneity, as if the phase average ($\mu_{phase}(u(y,i))$) does not remove variations along the span, then the spanwise variations are not homogeneous, while if the span average ($\mu_{span}(u(y,i))$) does not remove the cycle-to-cycle variations, then the cycle-to-cycle variations are not homogeneous. Figure 4.17 **a)** represents Equation 4.6. Since its values remain in the order of V_∞ for the areas of high vorticity around the DSV, it can be said that the spanwise variations are not homogeneous, since there are non-negligible variations along the span in the phase average. On the other hand, the cycle-to-cycle variations are in fact homogeneous. Figure 4.17 **b)** shows a peak value of the mean variance defined in Equation 4.7 that is an order of magnitude smaller than V_∞, and is in fact barely noticeable in the image. This means that after performing the span average, this one remains quite similar between cycles, with the relatively higher peaks of variance being negligible and only in the DSV region.

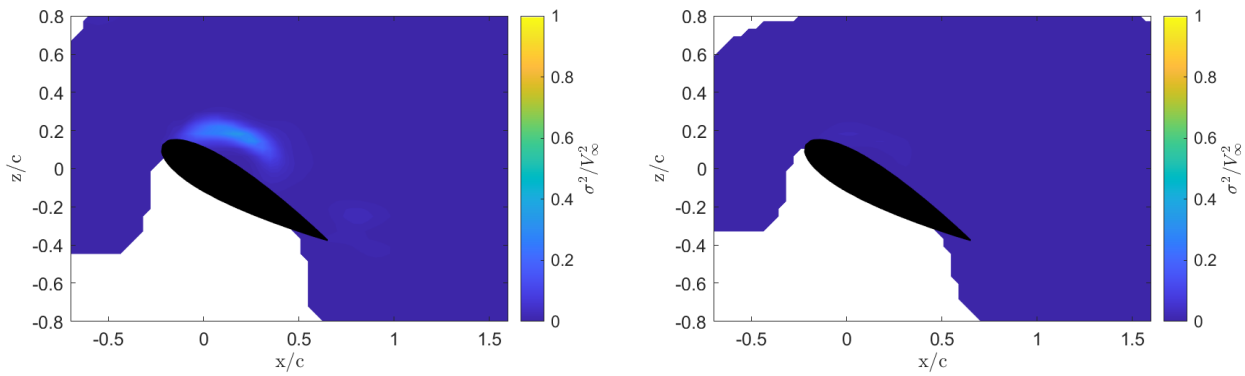

Figure 4.17: Representation of **a)**: Equation 4.6 and **b)**: Equation 4.7 for 250 cycles.

4.2.3. Airfoil Surface Analysis

Now the surface of the airfoil can be looked at in order to further characterize the cycle-to-cycle variations, and in particular its relationship to spanwise variations again, as well as to highlight a practical issue of foam accumulation with the measurement technique. Figure 4.18 shows the flow over the suction side of the airfoil. In order to do this, the u velocity is taken for the points sitting just above the surface of the airfoil. The first and second detected points right above the airfoil are discarded, as they are expected to contain higher levels of noise.

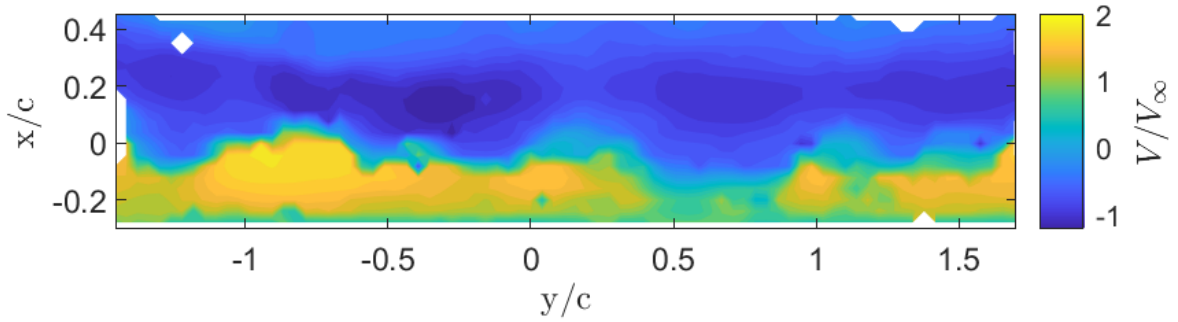

Figure 4.18: U velocity over the surface of the airfoil for cycle 1.

Once these points are extracted, the resulting surface points can be divided in those attached and separated. This is done by considering the points where $u > 0$ belonging to attached flow, while those with $u < 0$ are separated flow. Figure 4.19 shows the regions of attached flow for cycles number 1 and 250, while Figure 4.20 shows the regions of separated flow for those same cycles. Note how both cases, being a few seconds apart, present a different separation line between the cycles. Furthermore, along the span the separation point changes, showing the spanwise variations that have been mentioned before.

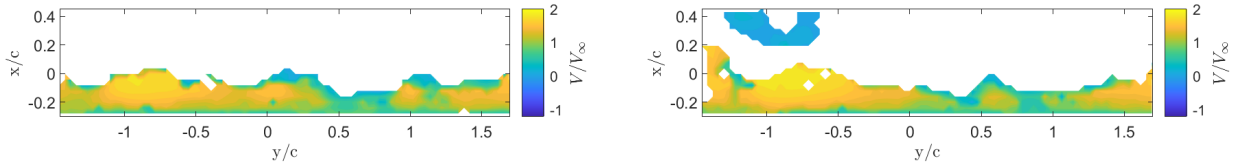

a) **b)**

Figure 4.19: Attached flow over the surface of the airfoil for **a)**: cycle 1 and **b)**: cycle 250.

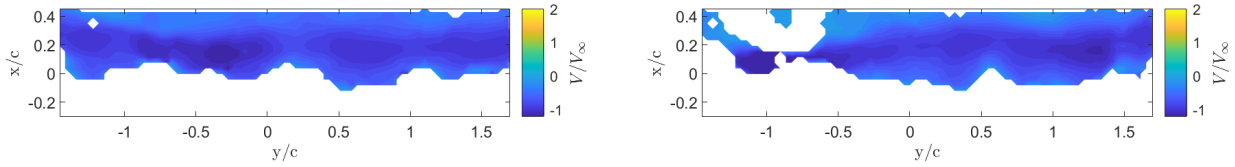

a) **b)**

Figure 4.20: Separated flow over the surface of the airfoil for **a)**: cycle 1 and **b)**: cycle 250.

It is telling to look at how the size of the region of separated flow evolves as cycles progresses. Initially, it was expected that the percentage of separated area over the airfoil would vary from cycle to cycle, somewhat independently of how much separation there was in the previous cycle, albeit within some bounds dictated by the state of attachment corresponding to the specific phase being studied. However, Figure 4.21 shows that this is not the case. While the separated area does vary from cycle to cycle, a clear trend in which the separated area decreases as time progresses can be observed. This could have different explanations. First, it could mean that there is in fact a hysteresis effect in the flow. The hypothesis of dynamic stall experiencing hysteresis is not new [22, 26], and is in fact likely to be present in dynamic stall, possibly contributing to cycle-to-cycle and spanwise variations.

However, this can be further looked into within the context of this experiment. As explained in Chapter 3, for these measurements, PTV using HFSB was used. During the experimental campaign, it was observed in-situ that the soap bubbles would stick to the surface of the airfoil more and more as long as the seeding in the tunnel was on. In particular, the leading edge of the tunnel model was accumulating a layer of foam over it, meaning that while the airfoil was clean during the first cycle, by cycle 250 the surface was quite foamy. This is the foam accumulation effect that has been briefly mentioned before. It can be seen below, with Figure 4.22 **a)**, representing cycle 1, which has noticeably less foam than Figure 4.22 **b)**, depicting cycle 250. This is appreciated at the left of the image, where the leading edge of the airfoil can be seen. The red and white line of dots, indicating the intensity of scattered light, is thinner for cycle 1 since it has less foam than cycle 250.

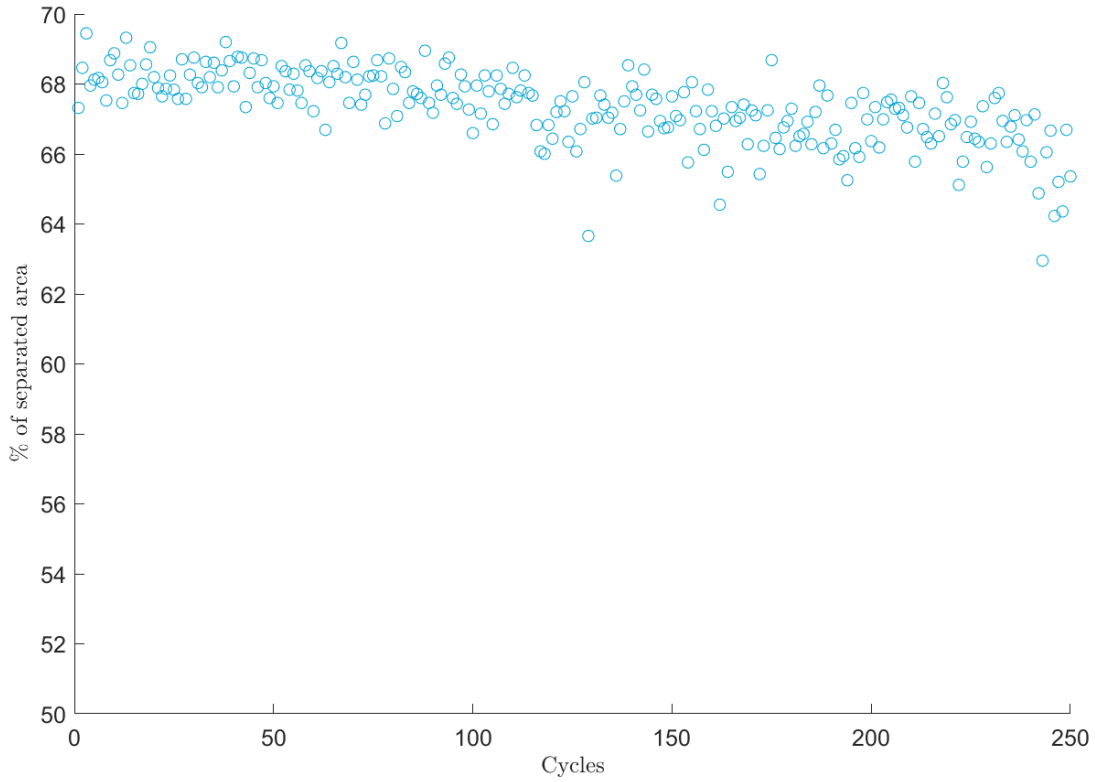

Figure 4.21: Percentage of separated flow over the airfoil for each cycle.

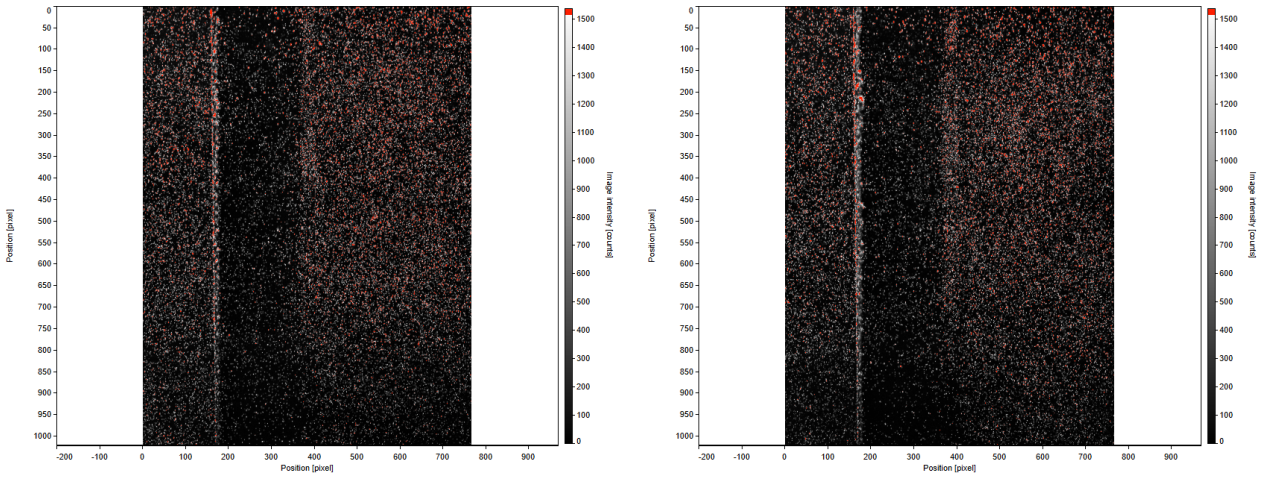

a) **b)**

Figure 4.22: Picture of the foam over the airfoil for **a)**: cycle 1 and **b)**: cycle 250.

In fact, this effect is even more extreme for the 1 Hz cases, as during these, the airfoil is exposed to the seeding for a longer time over the 250 cycles acquired, and therefore more foam accumulates on the surface. The effects of this longer exposure are shown in Figure 4.23, where it can be seen how the separated area decreases rapidly, to then slowly increase again. The line of foam at the leading edge is likely to be tripping the boundary layer, improving attachment to the surface by promoting transition. From Figure 4.23 it can be inferred that at some point around cycle 100, the foam becomes so much that instead of tripping the boundary layer and improve attachment, the shape is modified so much that the separation is increased. The foam accumulation can be checked through Figure 4.24 **a)**, **b)**, and **c)**, corresponding to cycles 1, 100, and 250 respectively, for the NACA0021, 1 Hz, 10 deg amplitude, $\frac{\pi}{10}$ case. It can be seen how, at a 100 cycles, which is one of the lowest separations points, shown in Figure 4.23, there is slightly more foam than in cycle 1, but it is still way less than in cycle 250. The 1 Hz cases end up with way more foam, since while the 250 cycles for this case lead to the airfoil being immersed in seeding for 250 seconds, for the 5 Hz cases the 250 cycles only require 50 seconds for the acquisition. The accumulation of foam is a limitation of the experimental technique, that could not be avoided during the experimental campaign in the current state of development of the technique. While during acquisition there was an effort to minimize this effect by operating the seeder so that it would produce the smoothest bubbles possible, and regularly cleaning the airfoil after every measurement taken, it was unavoidable to some extent.

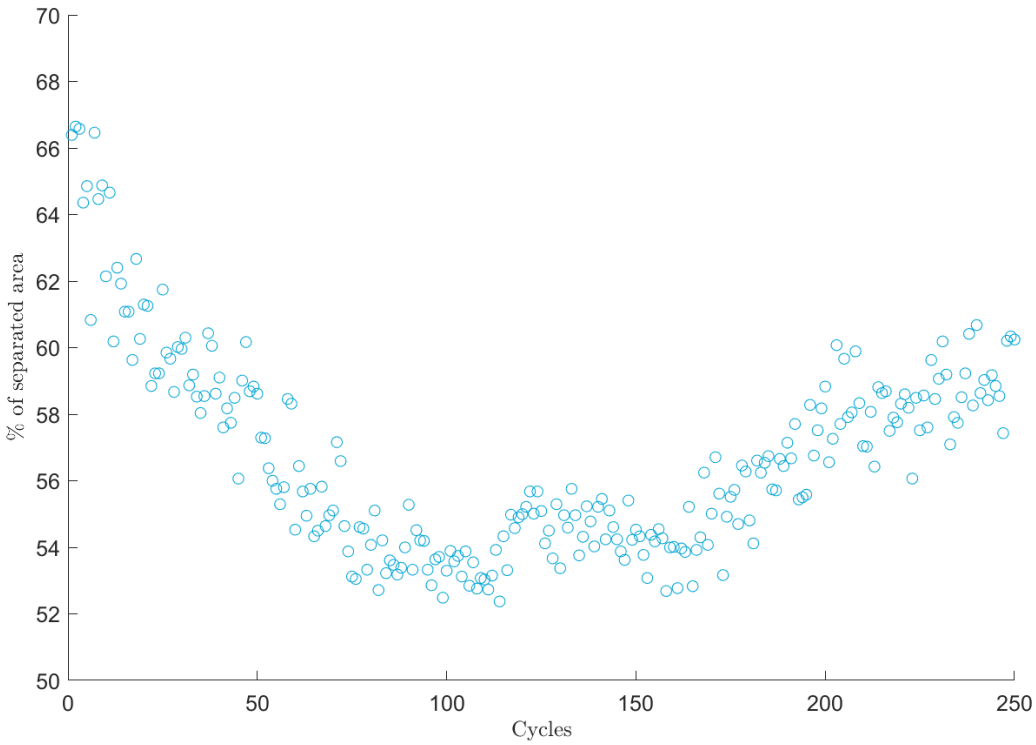

Figure 4.23: Percentage of separated flow over the airfoil for each cycle for the NACA0021, 1 Hz, 10 deg amplitude, $\frac{\pi}{10}$ case.

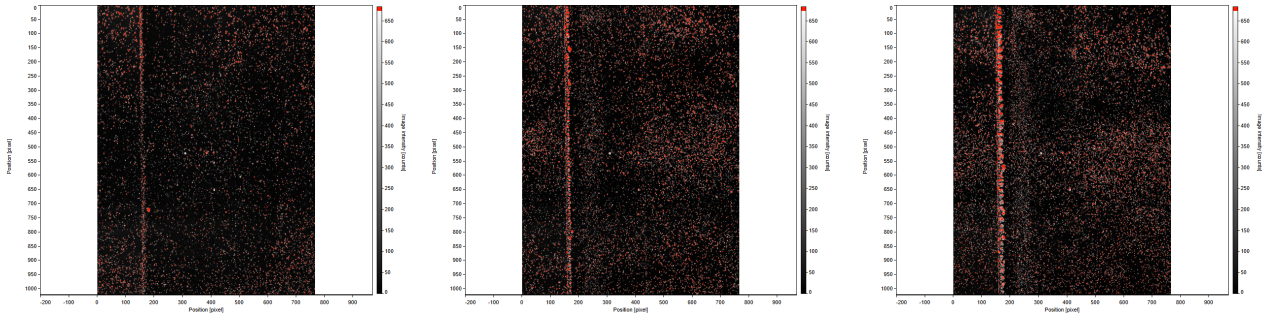

a) **b)** **c)**

Figure 4.24: Picture of the foam over the airfoil for the NACA0021, 1 Hz, 10 deg amplitude, $\frac{\pi}{10}$ case for **a)**: cycle 1, **b)**: cycle 100, and **c)**: cycle 250.

4.2.4. Isosurfaces

The in-homogeneity of the spanwise variations can be further proved using Figure 4.25, which shows isosurfaces of the phase averaged Q-criterion. These clearly depict the DSV as well as some stall cells, and their uneven distribution along the span is clear. While some locations have a thicker vortex, others have a thinner one, and also the location of the vortex core along the x-axis changes in span, as well as the separation location. The Q-criterion is a measure of the vorticity defined in Equation 4.8, following the definition by Hunt [50], in the notation of Banko [51]. It is a quantity commonly used to show vortical structures in the flow. In Equation 4.8, **V** is the velocity vector, **S** is the strain rate tensor, and Ω is the rotation rate tensor.

$$Q = \frac{1}{2}\left((\nabla \cdot \mathbf{V})^2 - \nabla\mathbf{V} : \nabla\mathbf{V}^{\mathbf{T}}\right) = \frac{1}{2}\left((\nabla \cdot \mathbf{V})^2 + ||\Omega||_2^2 - ||\mathbf{S}||_2^2\right) \tag{4.8}$$

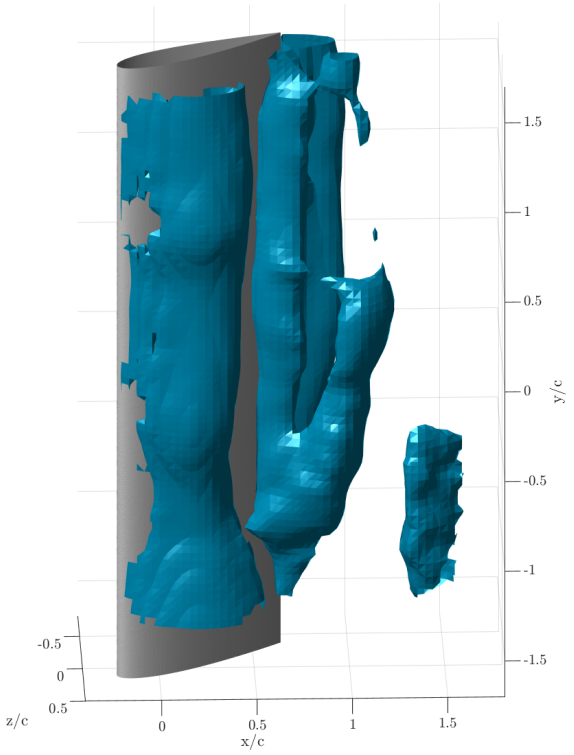

Figure 4.25: Isosurfaces of the Q-criterion for Q = 5 for the phase-averaged results.

The fact that the spanwise variations remain, even after performing the phase average of all the cycles, brings up the question of whether or not the flow tends towards a specific state/mode. Comparing the vortical structures for several cycles can give some information on this. Figure 4.26 represents isosurfaces of Q=5 for cycles 1, 25, 50 and 75. All the cycles show a region with a thicker DSV on the lower region of the domain, while cycles 1, 25 and 50 clearly show a thick DSV on the upper part of the image, that can also be seen in cycle 75 but is less defined. While cycles 25 and 50 show a dip in vortex thickness around the middle of the domain, this decrease is located slightly lower in cycle 1, and is more gradual, but existing, in cycle 75. Furthermore, the separation location seems to move quite forward for the lower part of the domain in cycles 25, 50, and 75. In cycle 1 this also seems to be the case, although the domain finishes right when the separation location moves slightly forward.

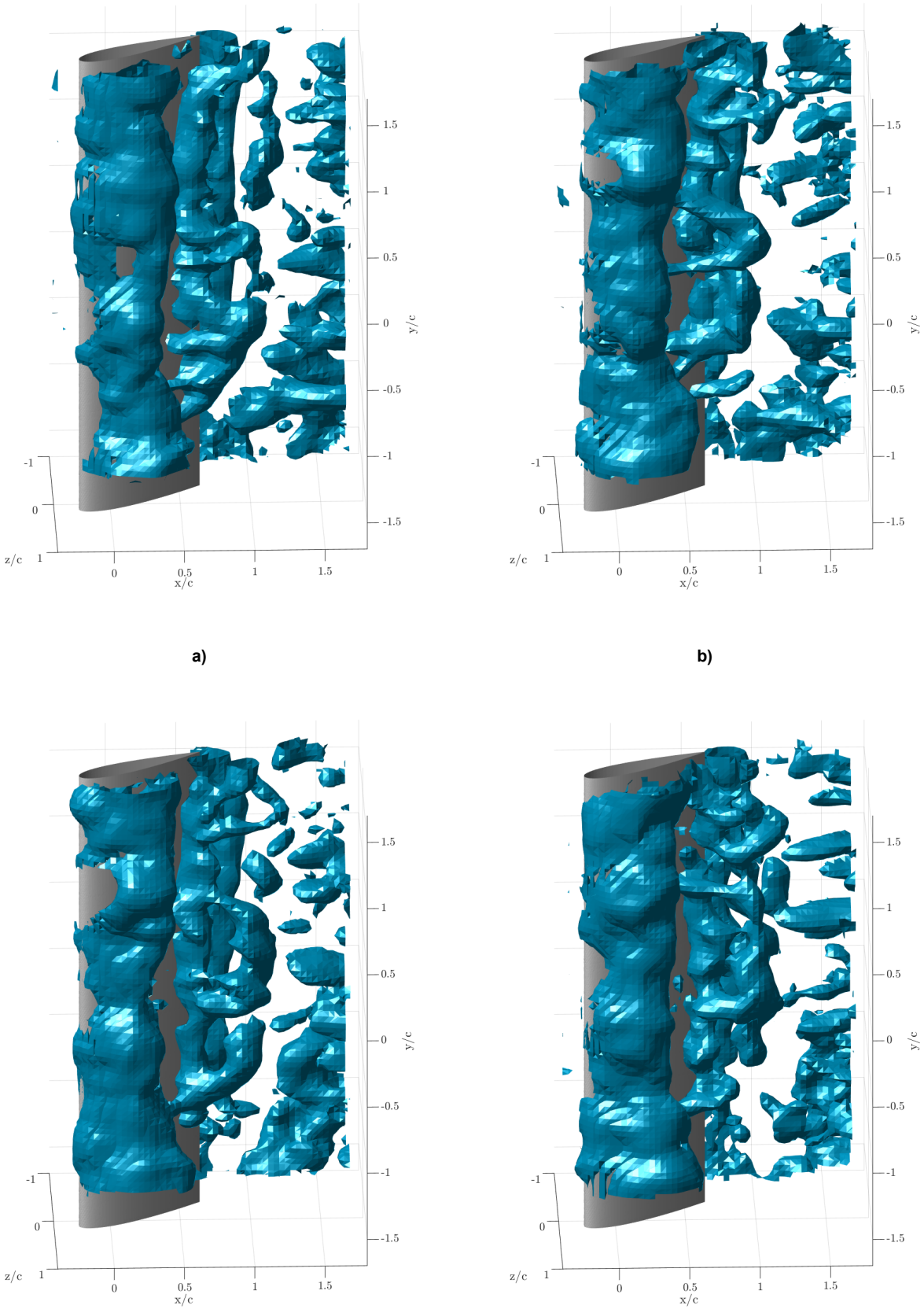

Figure 4.26: Isosurfaces of the Q-criterion for Q = 5 of **a)**: cycle 1, **b)**: cycle 25, **c)**: cycle 50, and **d)**: cycle 75.

Since looking at the small differences between individual cycles does not tell much, another method that could be used to determine the existence of flow states, would be to perform the phase average, but using different sets of cycles. Figure 4.27 **a)** and Figure 4.27 **b)** show Q-isosurfaces for Q = 5 for the phase average of cycles 1 to 125 and for cycles 126 to 250 respectively. While these already show similarities, it is important to note that the foam accumulation, an issue described in Section 4.2.3, and for which the consequences can be seen in Figure 4.21, can cause differences. Foam accumulation would make the later cycles be measured on a slightly different airfoil shape than the earlier ones, and therefore explain the change in shape of the DSV. Still, the DSV shows again a similar thicker shape at the upper and lower regions of the domain, while the middle region is thinner, in both images.

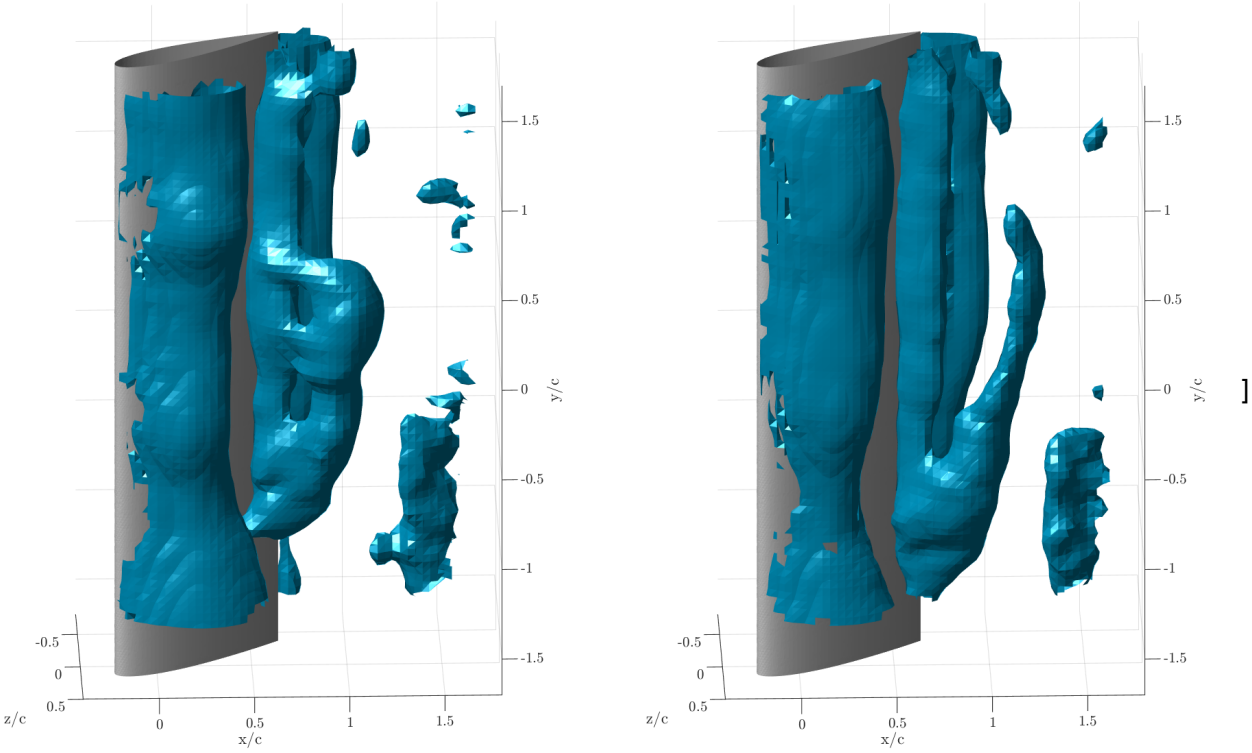

a) **b)**

Figure 4.27: Isosurfaces of the Q-criterion for Q = 5 for the phase average of **a)**: cycles 1-125 and **b)**: cycles 126-250.

The effect of foam accumulation can be removed when taking the phase average of cycles whose acquisition is evenly distributed in time. This is done by taking the phase average of cycles with an even index for Figure 4.28 **a)**, and the phase average of cycles with an odd index for Figure 4.28 **b)**. This gives an extremely similar shape for the DSV in both cases. The fact that using completely different cycles, very similar structures are obtained, that show very similar spanwise variations, implies that there are indeed states that the flow is likely to acquire.

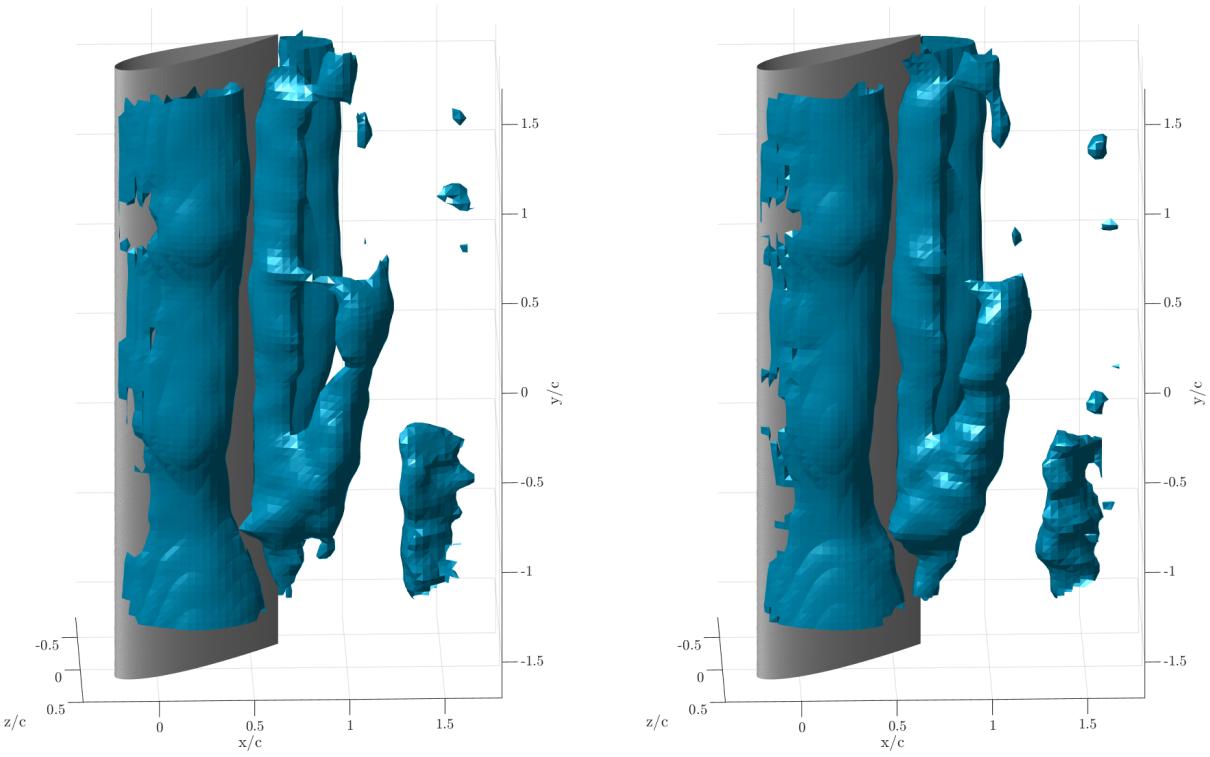

a) **b)**

Figure 4.28: Isosurfaces of the Q-criterion for Q = 5 for the phase average of **a)**: even cycles and **b)**: odd cycles.

There could be several reasons for the existence of these states. Firstly, it could be due to the tunnel conditions or the effects of the walls in the tunnel. The inflow conditions in the tunnel may not be perfect, and a spanwise velocity gradient could be present. However, since monitoring the inflow conditions was outside the scope of the experimental campaign, it is difficult to assess whether this is the case or not. Secondly, the foam accumulation, explained in Section 4.2.3, can also induce modes on the flow. Finally, there is the possibility that there are underlying physics in the dynamic stall phenomenon that lead the flow to have a tendency to certain states. Out of these options, it is likely that foam accumulation plays the biggest role, since when comparing the phase averaged flow structures for two completely different foam-accumulation states in Figure 4.27, the flow structures remain quite similar. The evolution of u' over time further supports this hypothesis, as it was mentioned in Section 4.2.1. However, while the foam accumulation seems to be a reason why the flow is acquiring certain states in the spanwise direction, as it was proved before, it is not the reason why the spanwise variations exist in the first place. Therefore, it can be said that there is no evidence to believe that the spanwise variations would disappear when the airfoil is completely clean and there is no foam accumulation.

4.2.5. Probability Density Functions

Past studies on cycle-to-cycle variations have shown bifurcation of the flow's pressure coefficient at a specific point over the airfoil, such as the experiments by Harms et al [26] shown in Figure 2.10, and Figure 2.11, in Section 2.2.2. A similar analysis can be done in this case using Probability Density Functions (PDFs), which will give the probability of the velocity u of taking a certain value at a certain point. This analysis will be performed entirely at the middle of the domain (mid-span). Figure 4.29 shows the PDFs for u at different points in a line within the mid-span, starting from outside of the separation bubble, and going progressively further into it, as it can be seen from the location of the selected points represented in Figure 4.30. In Figure 4.30, u is shown for cycle number 250 at the mid-span. The color of the PDF graph in Figure 4.29 matches that of the correspondent point from Figure 4.30. The black lines in Figure 4.29 show the kernel density estimate function of the PDF, an approximation solution that smooths out the PDF [52]. Figure 4.29 **b)** and Figure 4.29 **c)** are specially relevant as they illustrate points that experience reverse flow in some cycles, while in others they do not. This can be seen from the PDFs having two peaks in the probability density. In particular, Figure 4.29 **c)** shows one peak being clearly in the negative u, therefore experiencing reverse flow, and another (lower peak) on the positive u. This means that depending on the cycle, the selected point may take a negative value and

experience reverse flow, or take a positive value and experience forward flow. The peaks in Figure 4.29 **b)** are even clearer. However, in this case, both peaks are on the positive side of U. The reason why two peaks still appear despite the point being always under forward flow, is because when the flow is reversed in the point from Figure 4.29 **b)**, this state will induce a velocity gradient on the point forward, presumably reducing its velocity and causing a peak in the probability in Figure 4.29 **b)**. Similarly, when in Figure 4.29 **c)** the point experiences forward flow, the induced velocity will cause the other peak that appears in Figure 4.29 **b)**. On the other hand, Figure 4.29 **a)** and Figure 4.29 **d)** only show one main peak. This is because at their correspondent points, the flow is forward for most/all cycles in Figure 4.29 **a)**, while it is reversed for most/all cycles in Figure 4.29 **d)**. Figure 4.29 **d)** shows a small region of non-negligible probability that is under forward flow. As it can be seen in Figure 4.30, the corresponding point is relatively close to the limit of the separation bubble, and therefore, despite having a very clear peak under reverse flow, in some cycles the point is under forward flow. This is interesting as it accurately matches what was observed by Harms et al [26] using pressure measurements. In this case velocity measurements are used, but the outcome is the same, since the two peaks in the PDF distribution correspond to the two possible paths that the pressure can take in a cycle, one corresponding to a separated state, and the other to an attached state.

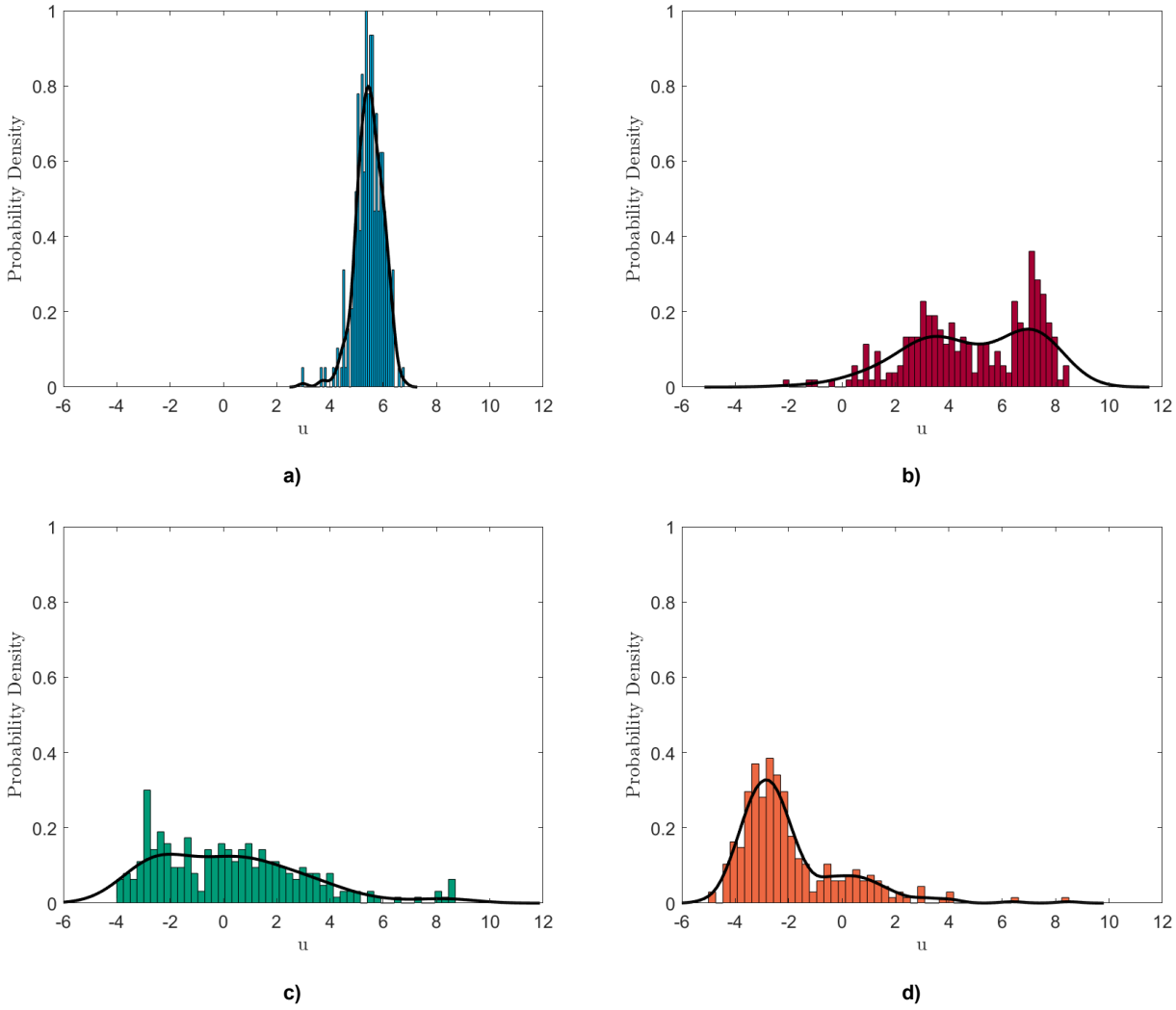

Figure 4.29: PDF for u at **a)**: $(x, z) = (-24.00, 14.34)$ mm, **b)**: $(x, z) = (-16.13, 14.34)$ mm, **c)**: $(x, z) = (-8.26, 14.34)$ mm, and **d)**: $(x, z) = (-0.38, 14.34)$ mm at 50% of the span.

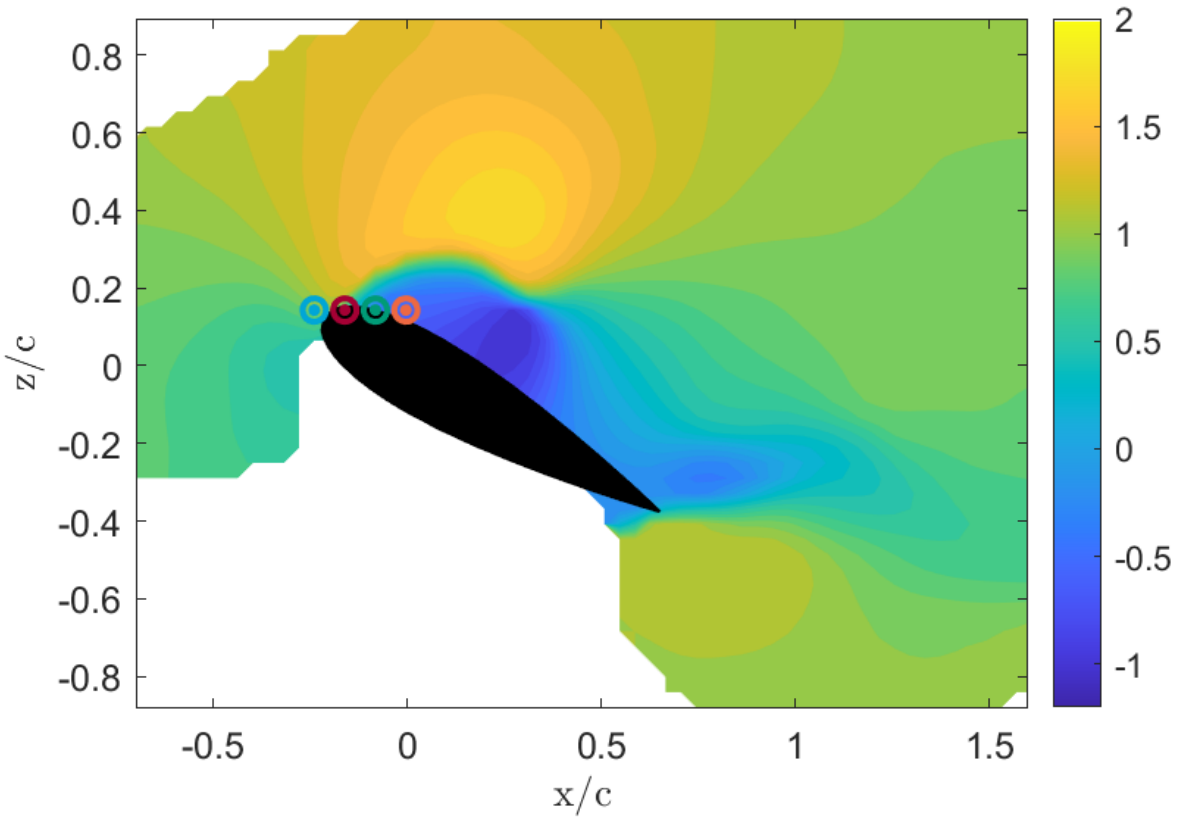

Figure 4.30: Locations of the points from Figure 4.29 (left to right) **a)**: $(x, z) = (-24.00, 14.34)$ mm, **b)**: $(x, z) = (-16.13, 14.34)$ mm, **c)**: $(x, z) = (-8.26, 14.34)$ mm, and **d)**: $(x, z) = (-0.38, 14.34)$ mm in a u slice at 50% of the span.

Performing a conditional average, it is feasible to observe how the velocity field looks at the mid-span for different conditions. It is possible to take only the cycles in which the velocity at one of the points in Figure 4.30 falls within a certain interval of velocities. With this in mind, Figure 4.31 **a)** represents the averaged mid-span velocity fields for when the velocity at $(x, z) = (-16.13, 14.34)$ is between 2 and 5 m/s, corresponding to the left peak in Figure 4.29 **b)**. Figure 4.31 **b)** represents the averaged mid-span velocity fields for when the velocity at $(x, z) = (-16.13, 14.34)$ is between 5 and 8 m/s, corresponding to the right peak in Figure 4.29 **b)**. On the other hand, Figure 4.31 **c)** represents the averaged mid-span velocity fields for when the velocity at $(x, z) = (-8.26, 14.34)$ is between -4 and 0 m/s, corresponding to the left peak in Figure 4.29 **c)**. Finally, Figure 4.31 **d)** represents the averaged mid-span velocity fields for when the velocity at $(x, z) = (-8.26, 14.34)$ is between 0 and 4 m/s, corresponding to the right peak in Figure 4.29 **c)**. Two interesting conclusions can be extracted from these images. Firstly, It is clear that in both points, the separation bubble corresponding to the interval of higher velocities, is significantly smaller than the one for the interval of lower velocities. Not only that, but the separation point is also further downstream for the interval of higher velocities, and this average features a higher velocity peak on top of the separation bubble. Secondly, it seems like the same cycles are taken to do the conditional averages in Figure 4.31 **a)** and **c)**, as well as in Figure 4.31 **b)** and **d)**. This can be stated because the images within each of these pairs look extremely similar to each other, implying that the same cycles were used to form the averages. This means that the same reason that makes one of the points take a lower interval of velocities, is what makes the other point take a lower interval as well, and the same holds for the higher velocity intervals. This bifurcation taking place between cycles, is now known to be in reality (also) along the span, with the same (x, z) location adopting a more separated or attached state depending on its spanwise location. Only the cycle-to-cycle bifurcation is shown here due to the larger available dataset, but the same is expected to take place along the span, and with more spanwise resolution it would be a feasible analysis.

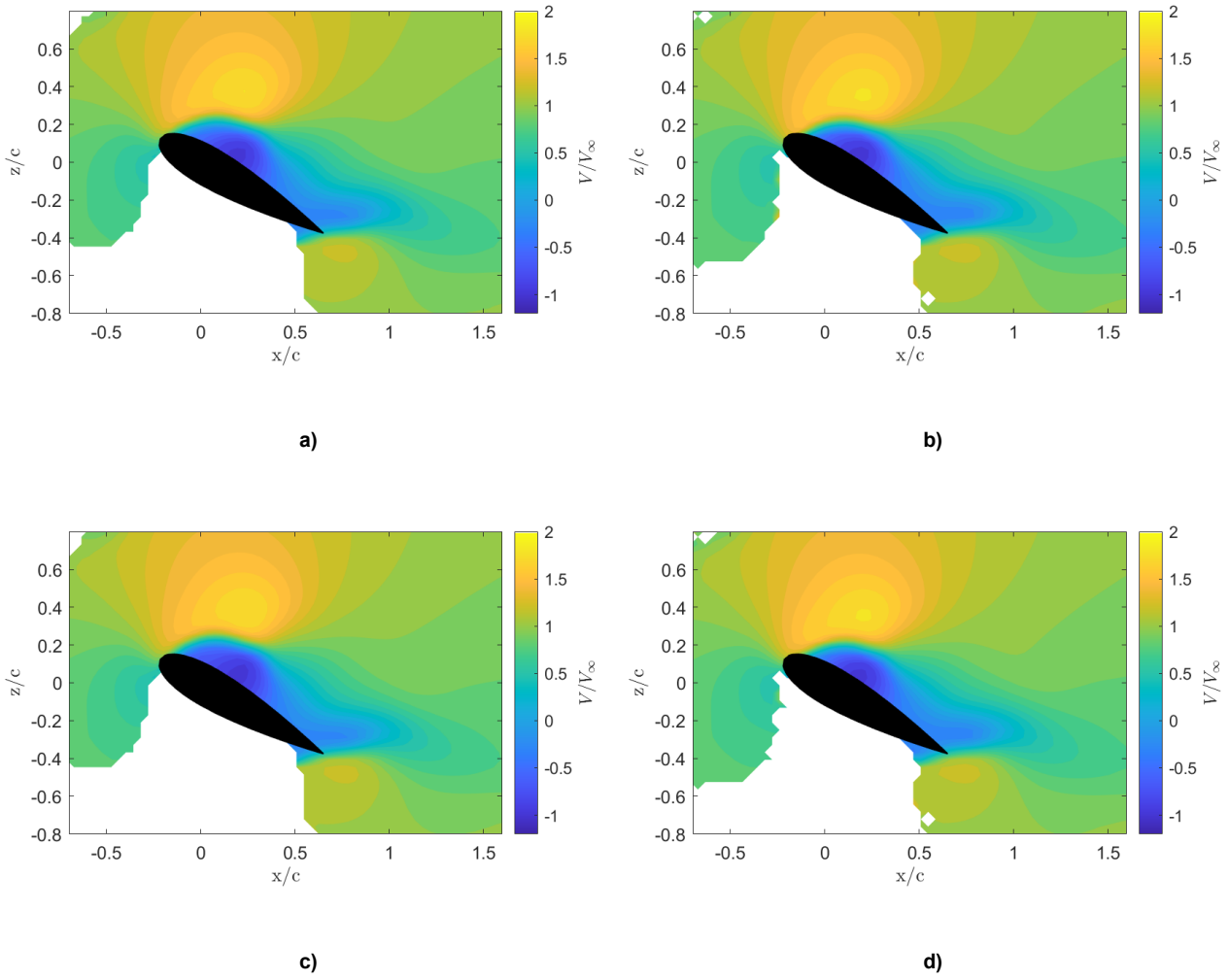

Figure 4.31: Conditionally averaged u at the mid-span for **a)**: u at $(x, z) = (-16.13, 14.34)$ mm: 2<u<5 m/s, **b)**: u at $(x, z) = (-16.13, 14.34)$ mm: 5<u<8 m/s, **c)**: u at $(x, z) = (-8.26, 14.34)$ mm: -4<u<0 m/s, and **d)**: u at $(x, z) = (-8.26, 14.34)$ mm: 0<u<4 m/s.

4.3. Effect of Various Parameters

This section compares the measurements on the NACA 0021 5 Hz 15° amplitude case with some of the other measured cases, changing one parameter at a time. First, different phases of the NACA 0021 5 Hz 15° amplitude case are studied in Section 4.3.1, looking into the time evolution of the case. Next, the effect of amplitude, of reduced frequency, and of the airfoil thickness are looked into in Section 4.3.2, Section 4.3.3, and Section 4.3.4 respectively.

4.3.1. Cycle-to-cycle variations at different phases

In order to study the changes in the flow within a cycle, as the phase progresses, the dynamic stall conditions from Section 3.3.2 will be used, and different points in phase will be taken from this case. Therefore, the NACA 0021 airfoil is analysed in this section under a motion of 5 Hz of frequency, which corresponds to a reduced frequency of 0.3, and for an amplitude of 15°. The phases of the dynamic stall cycle that will be studied here are $\frac{\pi}{2}$, $\frac{4\pi}{5}$, and $\frac{21\pi}{20}$. The first one corresponds to the part of the cycle where the angle of attack is the highest, at a quarter of the cycle, while the second phase takes place after the airfoil has reached its maximum angle of attack. The last phase chosen takes place well after the airfoil started pitching down.

Starting with phase averaged results, Figure 4.32, shows the mid-span y-slice of the phase averaged flow-field for the different phases. These allow to observe the general flow dynamics that are taking place. As it can be seen in Figure 4.33, at phase $\frac{\pi}{2}$, when the separation is just starting, the dynamic stall vortex remains close to the leading edge of the airfoil, and therefore it is expected to be increasing the suction over the airfoil, as it is creating a low pressure region. As the maximum angle of attack is approached, the DSV has detached from the leading edge of the airfoil, and is now located closer to the trailing edge of the airfoil. Since the flow

conditions correspond to a deep stall regime, and the airfoil is at its maximum angle of attack, it is expected that at this phase, the airfoil has started stalling. Further research including data on the pressure distribution or the loads over the airfoil could help on fully characterizing these states, as it is not possible to obtain reliable information on the lift of the airfoil with the available data. However, for the last phase being studied, it is clear that the airfoil has gone under deep stall and the flow is now re-attaching. Not only the vortex is now located far from the airfoil and breaking down, as it can be seen in Figure 4.32 **c)** and Figure 4.33 **c)**, and is therefore not able to cause any suction on the airfoil, but also, for both deep and light dynamic stall, it is known that due to the relative motion of the airfoil, a downward pitching motion always promotes further flow separation, and afterwards the re-attachment phase starts. Therefore, in Figure 4.32 **c)** a region of re-attaching flow can be seen all over the surface of the airfoil, and in Figure 4.33 **c)** no DSV vorticity can be seen.

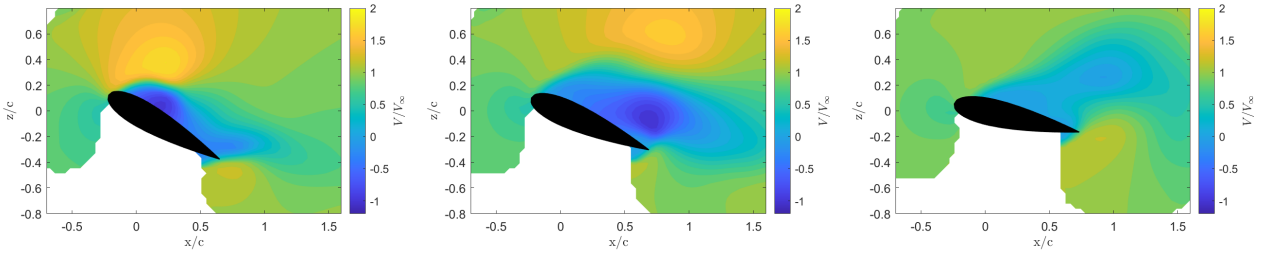

a) **b)** **c)**

Figure 4.32: $U + \tilde{U}$ velocity field at 50% of the span for a phase of **a)** $\frac{\pi}{2}$, **b)** $\frac{4\pi}{5}$, and **c)** $\frac{21\pi}{20}$.

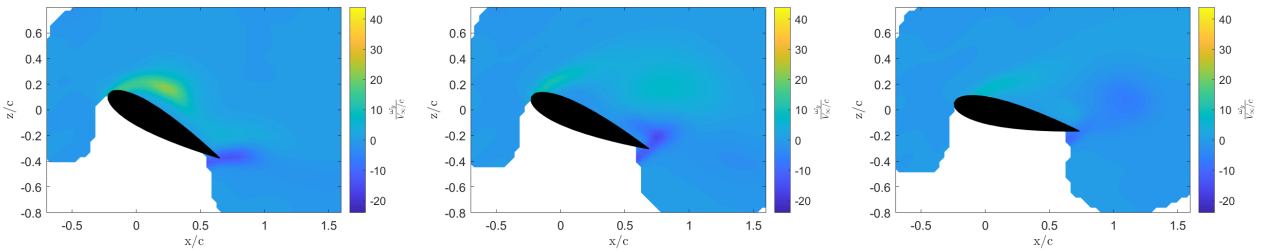

a) **b)** **c)**

Figure 4.33: Phase and span averaged vorticity field for a phase of **a)** $\frac{\pi}{2}$, **b)** $\frac{4\pi}{5}$, and **c)** $\frac{21\pi}{20}$.

Looking into the main topic of the research, as it was established in Section 4.2, cycle-to-cycle variations are a consequence of spanwise variations, and therefore in this section it is relevant to look into how the spanwise variations change with the phase. The metric to be used for this, is the average over 250 cycles of the variance in span with respect to the span average of each cycle. These averages are represented in Figure 4.34, for the phases chosen under the aforementioned conditions. For all the phases, the largest variance can be found where the vortex core is expected to be for each case. This means that the spanwise variations are mostly dictated by the location of the vortex core, as the peak in spanwise variations follows this core within the cycle. Plot **b)** from Figure 4.34 is remarkably similar to Figure 9 in Snortland's [33] research in dynamic stall, showing cycle-to-cycle variations being similar to spanwise variations even for different applications. Comparing the intensity of these variations, it can be seen that it is highest for a phase of $\frac{\pi}{2}$. Out of the available phases, this is the phase at which the vortex has a more coherent core, and its location shifts along the span, while at the phases of $\frac{4\pi}{5}$ and $\frac{21\pi}{20}$ the structure is diffused in space. Because of this, the region of non-zero variance around the vortex is larger for Figure 4.34 **b)**, and Figure 4.34 **c)**, but the variance is way lower. Therefore it can be said that the spanwise variations are largest when the DSV is forming/just formed and is more coherent, while when the vortex breaks down, the spanwise variations are lower, but they occupy a larger region.

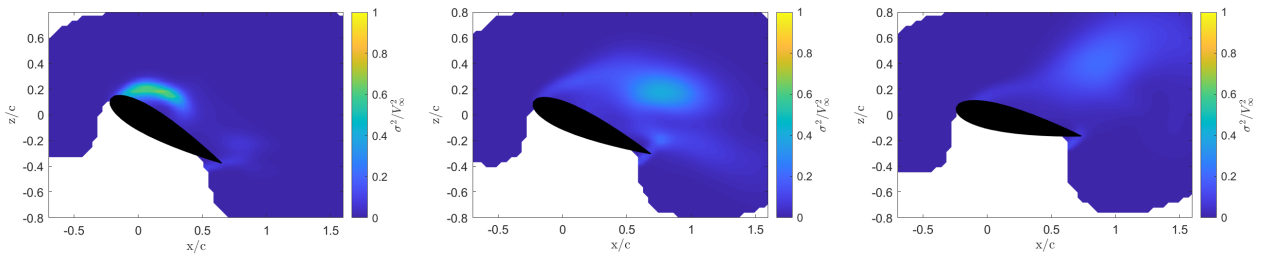

a) **b)** **c)**

Figure 4.34: $\mu_{phase}(\sigma^2_{span}(u))$ for a phase of **a)** $\frac{\pi}{2}$, **b)** $\frac{4\pi}{5}$, and **c)** $\frac{21\pi}{20}$.

As explained in Section 4.2.3, the evolution of separation percentages is to be given, as due to foam accumulation, the airfoil shape is changing slightly, and seeing how the amount of separated surface evolves over time will give an idea of how impactful the foam accumulation has been for a certain measurement. Figure 4.35 shows this evolution for the studied phases. While at $\frac{21\pi}{20}$ there is not a strong trend in the flow, possibly due to the fact that the airfoil is attaching, both at $\frac{\pi}{2}$ and $\frac{4\pi}{5}$ there is a trend that is likely caused by foam accumulation. However, the trends are reversed, as while for a phase of $\frac{\pi}{2}$ the separated area reduces over time, for $\frac{4\pi}{5}$ this area is increasing. While the exact consequences of the foam accumulation are hard to predict, it is possible that in Figure 4.35 **a)** the foam is tripping the boundary layer and improvement attachment slightly over the few seconds that are being measured, while at the higher angle of attack corresponding to Figure 4.35 **b)**, the angle of attack may be already so high that a layer of foam may only be increasing the separation. Note that the levels of separation for Figure 4.35 **c)** are significantly lower than in Figure 4.35 **a)** and in Figure 4.35 **b)**. Since at a phase of $\frac{21\pi}{20}$ the airfoil is already pitching down, it is possible that the flow is starting to attach back to the surface, and therefore Figure 4.35 **c)** takes place at the re-attachment phase of the cycle. This can be further proved looking at the velocity u over the surface of the airfoil. Figure 4.36 **c)**, corresponding to a phase of $\frac{21\pi}{20}$, shows higher velocity overall than Figure 4.36 **a)** and Figure 4.36 **b)**, which further strengthens the idea that the airfoil is in the re-attachment phase.

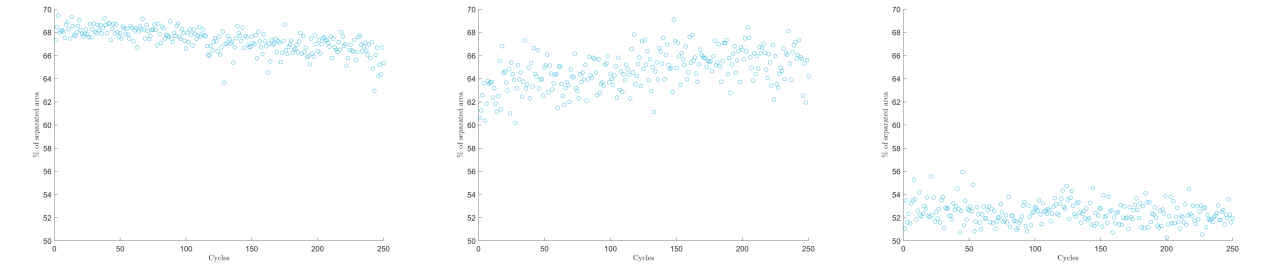

a) **b)** **c)**

Figure 4.35: Separation percentage evolution for a phase of **a)** $\frac{\pi}{2}$, **b)** $\frac{4\pi}{5}$, and **c)** $\frac{21\pi}{20}$.

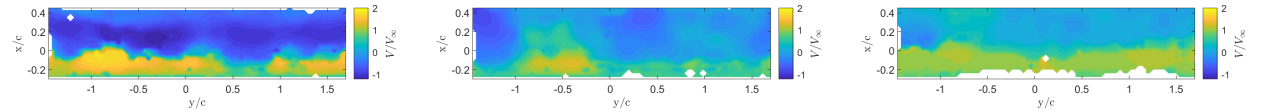

a) **b)** **c)**

Figure 4.36: U at the surface at cycle 1 for a phase of **a)** $\frac{\pi}{2}$, **b)** $\frac{4\pi}{5}$, and **c)** $\frac{21\pi}{20}$.

4.3.2. Effect of Amplitude

Once the evolution within a cycle has been looked into, it is interesting to study the effect of changing different parameters on the cycle-to-cycle and spanwise variations. Starting with changing the amplitude, $\Delta\alpha$ values of 10° and 15° are chosen. First, the phase and span average can be looked into in Figure 4.37. As the airfoil pitching at an amplitude of 10° reaches a lower maximum inclination, for the same phase, as it is the case for

these two plots, the angle at which the measurement of 10° amplitude is taken is slightly lower. The phase comparison was considered more relevant than the geometric, as the angle difference is not too large between phases, but the flow can be. Looking at U, Figure 4.37 **b)** has a larger separated region than Figure 4.37 **a)**. This may result contradictory, as the geometrical amplitude of Figure 4.37 **b)** is lower (10°) than in Figure 4.37 **a)**, but in the context of dynamic stall, it makes sense, since the pitching rate for an amplitude of 15° is larger than for an amplitude of 10°. A faster relative motion can lead to more attached flow before the onset of dynamic stall. However, after the onset takes place, the opposite happens, and a more violent stalled stage occurs for the 15° amplitude, as it can be seen in Figure 4.38 **a)** and in Figure 4.39 **a)**, while Figure 4.38 **b)** and Figure 4.39 **b)** shows a lower degree of separation for a 10° amplitude.

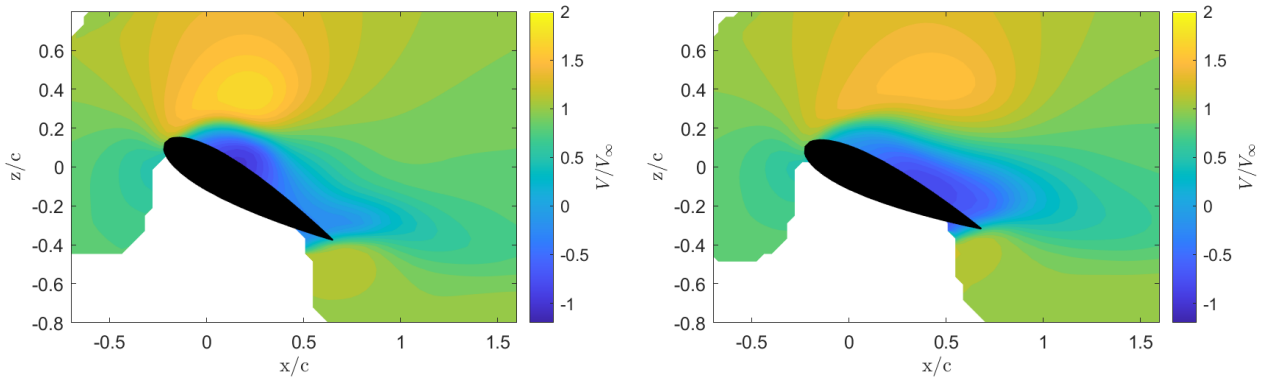

a) **b)**

Figure 4.37: U velocity field at $\theta = \frac{\pi}{2}$ for an amplitude of **a)**: 15° and **b)**: 10°.

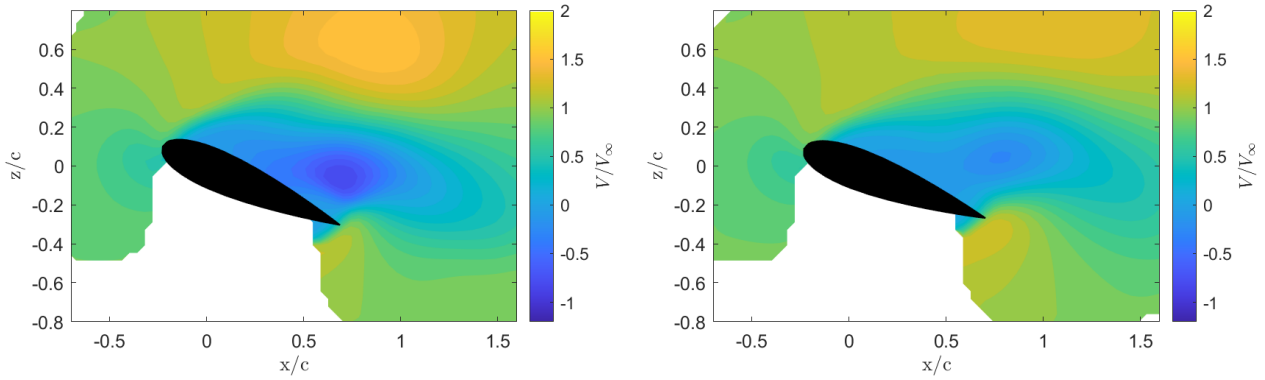

a) **b)**

Figure 4.38: U velocity field at $\theta = \frac{4\pi}{5}$ for an amplitude of **a)**: 15° and **b)**: 10°.

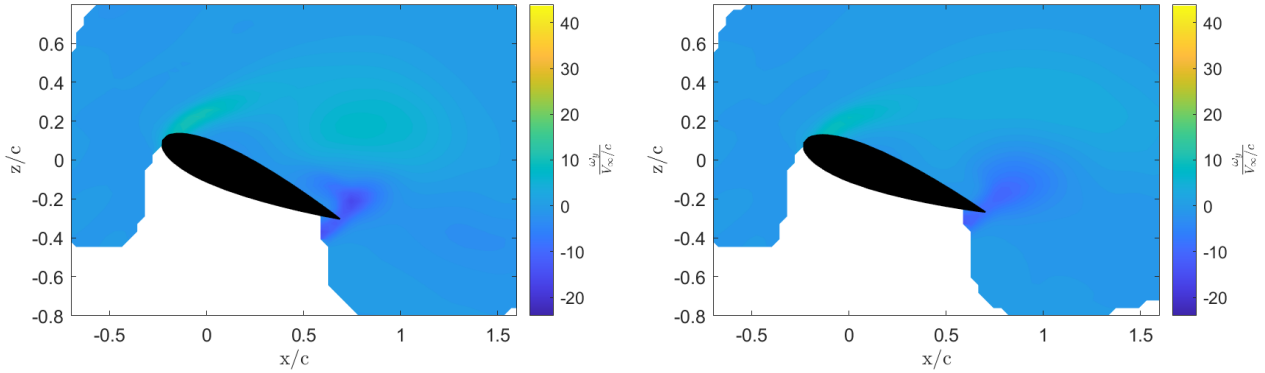

a) **b)**

Figure 4.39: Phase and span averaged vorticity field at $\theta = \frac{4\pi}{5}$ for an amplitude of **a)**: 15° and **b)**: 10°.

Looking into the spanwise variations, Figure 4.40 shows important differences. Firstly, there is an important distinction in where the variations are peaking. While for the larger amplitude the variance peaks are concentrated at the DSV area, for the lower amplitude the region of high variance distributes along the limit of the separation bubble, as it is the region of higher unsteadiness. In addition, also the peaks for the higher amplitude are higher, possibly due to a higher velocity gradient.

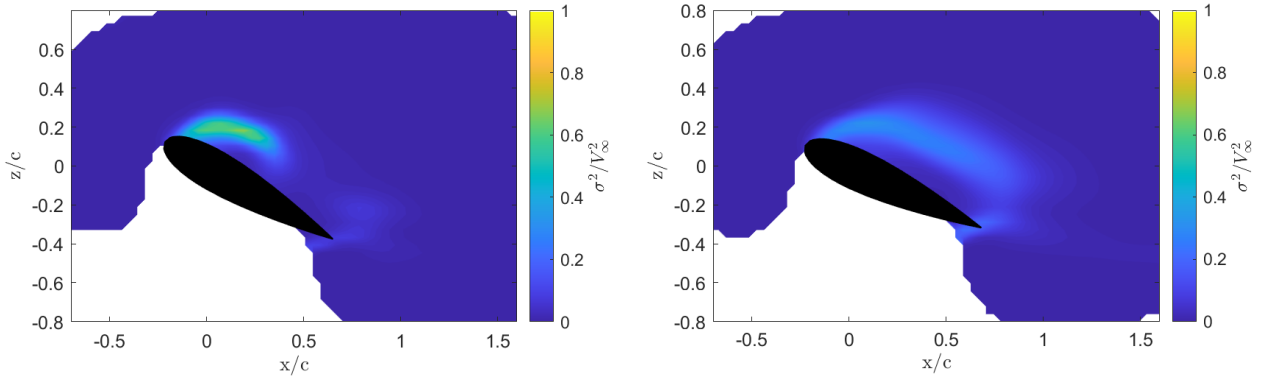

a) **b)**

Figure 4.40: $\mu_{phase}(\sigma^2_{span}(u))$ at $\theta = \frac{\pi}{2}$ for an amplitude of **a)**: 15° and **b)**: 10°.

4.3.3. Effect of Reduced Frequency

During the experimental campaign, two different frequencies were measured, being 1 Hz and 5 Hz, which correspond to a reduced frequency (k) of 0.06 and 0.3 respectively. In this section, the NACA 0021 cases for an amplitude of 15° will be discussed for both frequencies. Figure 4.41 shows U for 5 Hz and 1 Hz respectively. Two different phases were taken for the comparison. This is because the difference in the flow was too large between cases at the same phases, and instead of taking the measurement at the same phase, the aim was to take the measurement at a similar flow state within the dynamic stall cycle. In this case, it was expected to capture the initial DSV formation, before the dynamic stall onset, and the phases at which this happened were $\theta = \frac{\pi}{2}$ for the 5 Hz case, and $\theta = \frac{\pi}{10}$ for the 1 Hz case. As opposed to what was observed in Section 4.3.2 for the lower amplitude case, the 1 Hz case has a significantly thinner separation region. However, in this case this is reasonable, because the angle of inclination is also significantly lower. Furthermore, in Figure 4.42 it can be seen how for a lower angle of attack, the DSV is in a similar state of formation, albeit, with a lower strength. This difference in vorticity can be due to the 1 Hz case being closer to the quasi-steady aerodynamics domain, while the 5 Hz is in the highly unsteady aerodynamics domain.

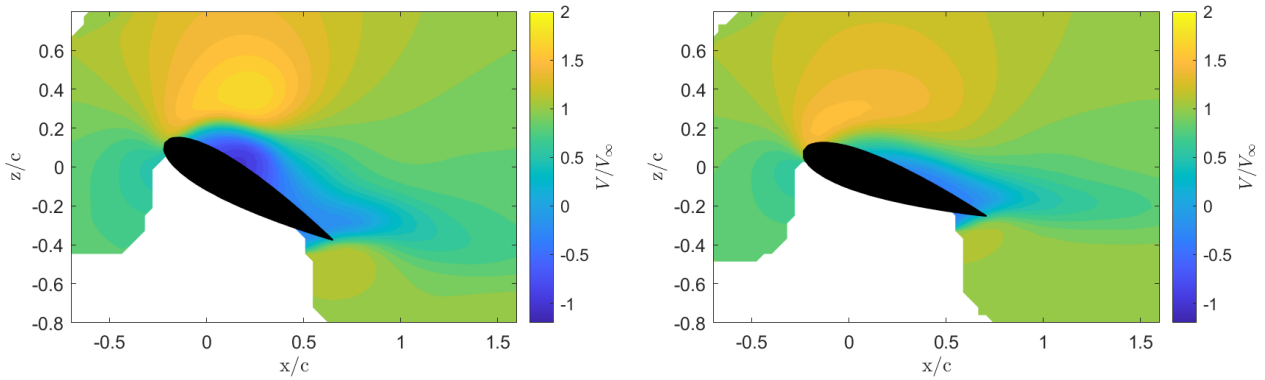

a) **b)**

Figure 4.41: U velocity field at **a)**: $\theta = \frac{\pi}{2}$ for $k = 0.3$ and **b)**: $\theta = \frac{\pi}{10}$ for $k = 0.06$.

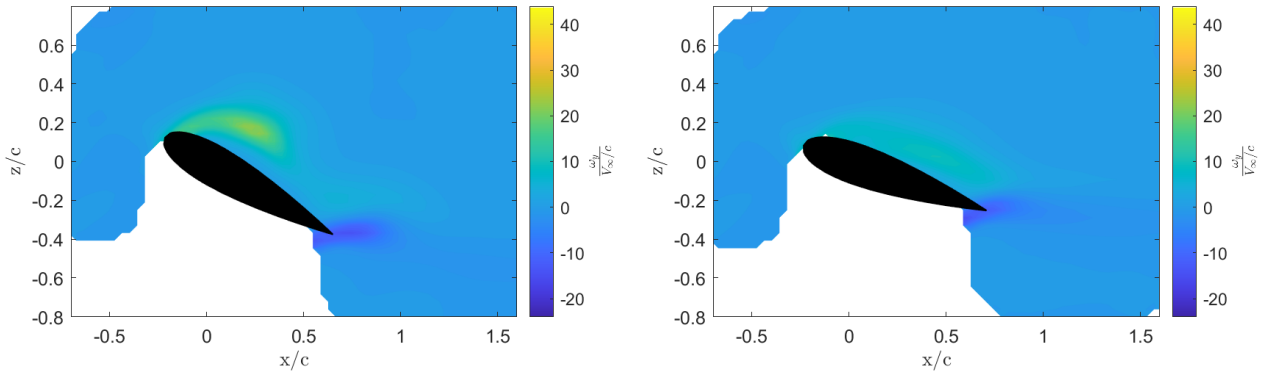

a) **b)**

Figure 4.42: Phase and span averaged vorticity field at **a)**: $\theta = \frac{\pi}{2}$ for $k = 0.3$ and **b)**: $\theta = \frac{\pi}{10}$ for $k = 0.06$.

The spanwise variations in Figure 4.43 provide further insight. While the regions of high variance are quite different between the 1 Hz and the 5 Hz cases, which is due to the angles being significantly different, the peaks in variance remain similar, with the 1 Hz case having a larger region of high variance. This matches with the results shown in Section 2.2.3, where it was concluded that the cycle-to-cycle variations, now known to be a manifestation of spanwise variations, are larger for the lower reduced frequencies [26]. This is important, as while in both cases, the largest spanwise variations are at the vortex core, the extent of the variations does not seem to depend on how large the vorticity is, but on the vortex core shifting its location along the span. This can be seen in Figure 4.44, where multiple vorticity plots are shown at different spanwise locations. While the intensity of the vorticity remains in the same order of magnitude for all three plots, the shape and location of the vortex core changes.

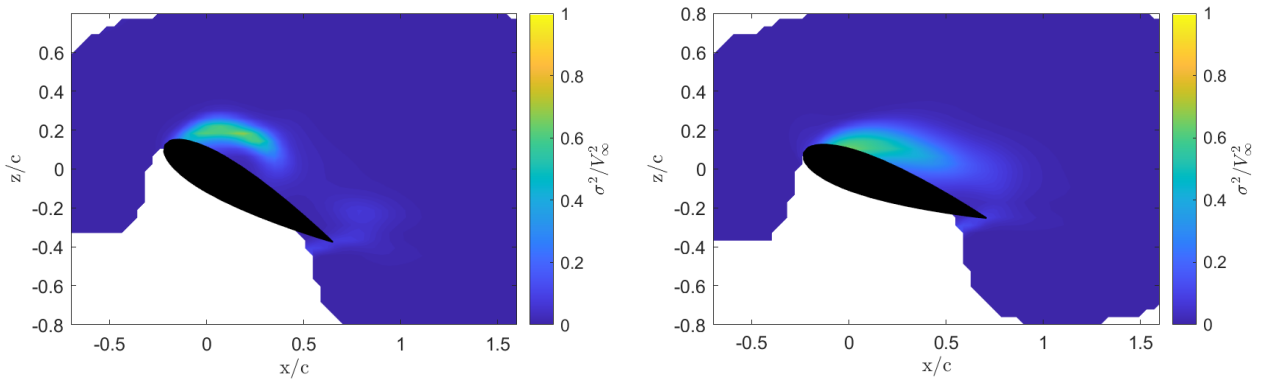

a) **b)**

Figure 4.43: $\mu_{phase}(\sigma^2_{span}(u))$ at **a)**: $\theta = \frac{\pi}{2}$ for $k = \frac{\pi}{10}$ and **b)**: $\theta = \frac{\pi}{10}$ for $k = \frac{\pi}{50}$.

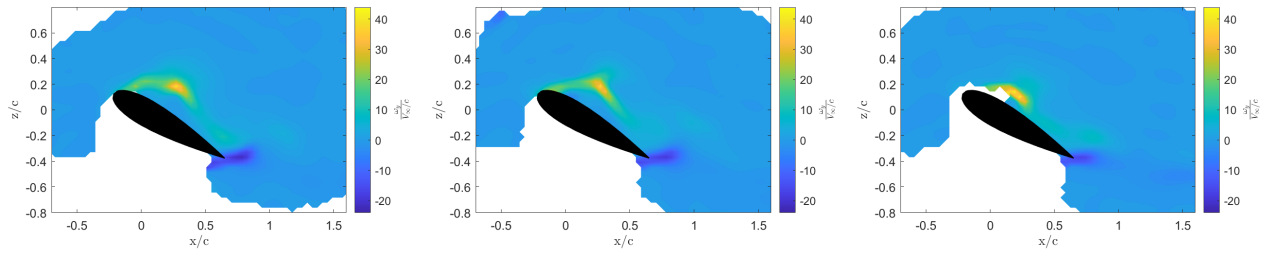

a) **b)** **c)**

Figure 4.44: Vorticity slices of the NACA 0021, 5 Hz, 15° amplitude case for a spanwise location of **a)** 25%, **b)** 50%, and **c)** 75% of the span.

4.3.4. Effect of Airfoil Thickness

The final parameter to be compared is the airfoil thickness. This was done by measuring two different airfoils for which only the thickness was different, the NACA 0021, which is the airfoil that has been analysed until this point, and the NACA 0012. Figure 4.45 shows U for the NACA 0021 and the 0012 respectively, both at the same phase of $\frac{\pi}{2}$, a frequency of 5 Hz, and an amplitude of 15°. It is clear that for the thinner airfoil in Figure 4.45 **b)** the stall is way more advanced, with a larger separation region that is also further away from the leading edge (where dynamic stall is onset). Having a thinner airfoil usually implies earlier separation and leading edge stall also for the static case [7], so for the same conditions, at the same point in phase, it makes sense that the thinner airfoil is under more severe stall. When looking at the vorticity in Figure 4.46, a vortex with a stronger core is found for the NACA 0021, while for the NACA 0012 the region. This is similar to what was observed when analysing the effect of phase in Section 4.3.1, meaning that a thinner airfoil will be expected to go through the dynamic stall onset and subsequent stages earlier in phase.

Looking at the spanwise variations in Figure 4.47 for the NACA 0021 and NACA 0012, once again it can be seen how the largest variations are concentrated in the vortex core of the DSV in Figure 4.47 **a)**. A larger region of vorticity does not translate into a higher variance, or a larger region of higher variance. In fact, in the more stalled case of the NACA 0012, the variance is lower. This could be the consequence of the DSV starting to lose strength and break down, which reduces the variations in spanwise direction due to its less defined core.

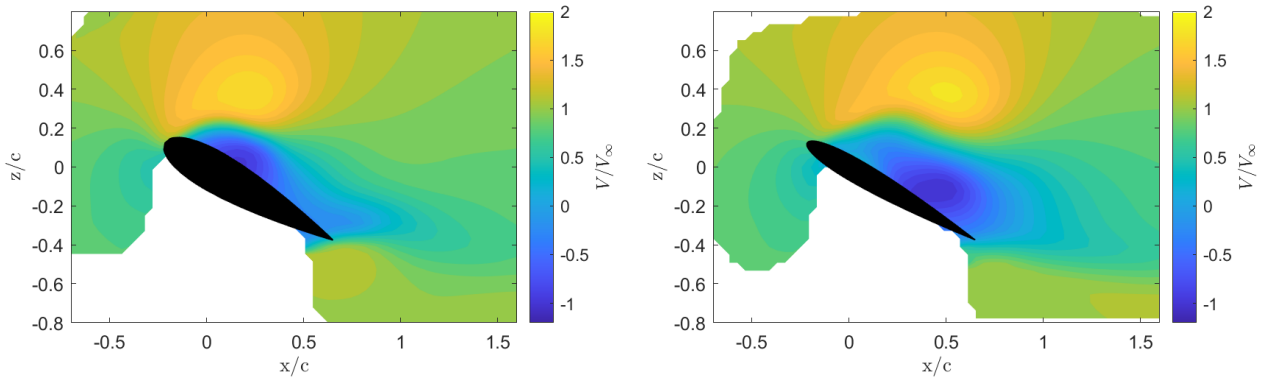

a) **b)**

Figure 4.45: U velocity field at $\theta = \frac{\pi}{10}$ for the **a)**: NACA 0021 and **b)**: NACA 0012.

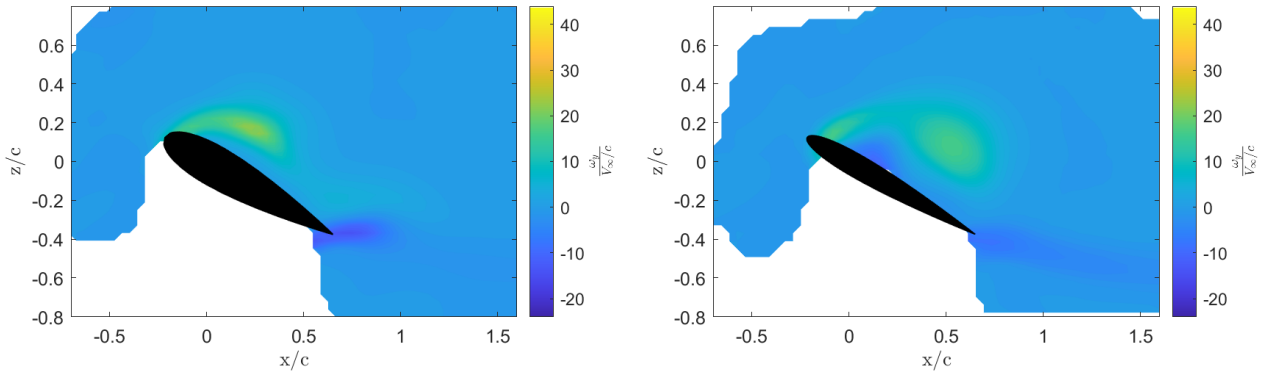

a) **b)**

Figure 4.46: $\mu_{span}(\mu_{phase}(\omega_y))$ vorticity field at $\theta = \frac{\pi}{2}$ for the **a)**: NACA 0021 and **b)**: NACA 0012.

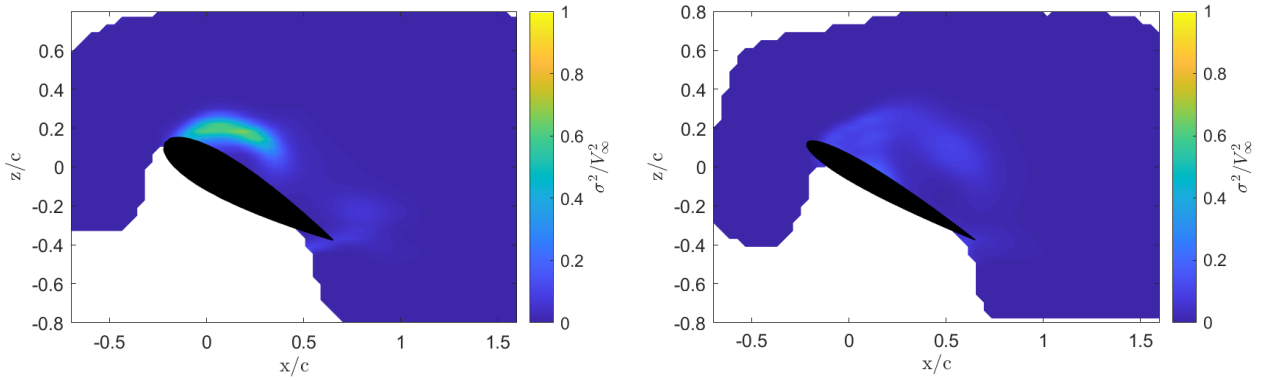

a) **b)**

Figure 4.47: $\mu_{phase}(\sigma^2_{span}(u))$ at $\theta = \frac{\pi}{2}$ for the **a)**: NACA 0021 and **b)**: NACA 0012.

5. Recommendations and Future Works

The research project, while enlightening, did not provide all the answers to cycle-to-cycle variations. Firstly, the physics behind the modes that the flow acquires are not fully characterized. It is clear that there are effects from the tunnel walls, the airfoil joint to the wall, and the inflow conditions, that may be causing the flow to tend to a certain state. Therefore, further experiments on dynamic stall could include monitoring of the inflow conditions, to observe if there is a velocity gradient around the test section inlet that appears to be creating a certain mode in the flow. Moreover, a larger measurement domain that can capture wall effects could also be useful, although the accuracy of PTV may be compromised near the walls, and therefore it could be interesting to explore other measurement techniques to monitor it. In addition to this, the foam accumulation from the HFSB explained in Section 4.2.3 could also increase the spanwise variations, or at the very least, dictate the modes, and reducing it should be an effort in further research. On another note, the resolution offered by HFSB PTV is not high enough to measure the smaller scales of vorticity. There could be small-scale vortical structures that trigger spanwise modes. Other measurement techniques that offer higher resolution, such as tomographic PIV, or further improvements on HFSB technology and PTV algorithms, could provide a higher resolution that would give further insight on the impact of small structures on the spanwise variations and the modes. With a higher resolution, more spanwise points could be measured, and therefore the analysis on conditional averages and bifurcation could also be done along the span. Finally, while the focus of this research was on a statistical analysis of the cycles and the spanwise variations, a more fundamental approach on the time-resolved data could be taken. With the available data, a careful study on the evolution of the flow over time, and the possibility of hysteresis having an impact on the spanwise variations, the flow states, or just on dynamic stall as a phenomenon, could be further explored.

Dynamic stall is an exciting and rich research topic within unsteady, subsonic, vortex-dominated flows, which can have a bright future for improving on the development of moving wings in the long run. The contributions to the physical understanding of the phenomenon, can make an improvement on the CFD simulations, making for quicker and more efficient engineering development for a more sustainable design.

6. Conclusion

Looking at the results of the experimental campaign, the use of HFSB as a measurement technique allowed to provide insight on the origin of cycle-to-cycle variations. Getting data over a volume, being time-resolved, or using phase locked measurements for a more statistical analysis, brought to light certain qualities of a dynamically stalling flow that were never observed before.

The main outcome of the project, obtained thanks to the HFSB PTV, was that **the cycle-to-cycle variations are a manifestation of the spanwise in-homogeneity, caused by the flow structures shuffling along the span**. This is crucial, since it shifts the problem from a study on cycle-to-cycle variations, to a study on spanwise variations. Furthermore, this finding deems the use of planar PIV for dynamic stall studies somewhat obsolete, since it is unable to capture the spanwise variations along the span. Volumetric measurements are then concluded to be the best technique to characterize dynamic stall experiments. Not only the relationship between cycle-to-cycle and spanwise variations was established, but it was also concluded that **the flow structures tend to acquire a specific state along the span**, meaning that the separation line and the DSV tend towards a specific shape, and therefore each point is more likely to take certain values than others. It can be stated that dynamic stall causes modes or states to appear on the flow. These modes follow bifurcation [26], in which the points in the limit of the separation bubble take a more separated or attached state depending on the cycle and location, and therefore the spanwise location.

On the topic of the effect of amplitude, this was deemed to be dominated by the pitch rate of the airfoil and therefore the effect of the relative motion of the airfoil with respect to the air. While for a lower pitching rate, corresponding to a motion amplitude of 10°, the flow separates earlier, as the pitch-up motion is less favourable for attachment, for the higher pitching rate, with an amplitude of 15°, the stalled stage is more violent, as the faster pitch-down movement promotes separation. The largest spanwise variations are concentrated in the DSV core, and therefore the larger amplitude, having a more defined DSV, experiences larger spanwise variations. However, looking at the reduced frequency comparison, it can be said that the vorticity strength of the DSV does not necessarily increase the spanwise variations. This is concluded from the fact that the variance values for a reduced frequency close to the quasi-steady state are very similar or higher than the variance of a highly unsteady case, while simultaneously, the DSV strength is significantly larger for the highly unsteady frequency than the lower one. Regarding the effect of the airfoil thickness on the spanwise variations, a thinner airfoil presents a larger separation region, with a weaker and less coherent DSV. Therefore, despite the NACA 0012 being more separated, the spanwise variations are larger for the thicker NACA 0021.

References

[1] W. J. McCroskey. *The phenomenon of dynamic stall*. 1981.

[2] Manikandan Ramasamy et al. “Characterizing cycle-to-cycle variations in dynamic stall measurements”. In: *Journal of the American Helicopter Society* 63.2 (Apr. 2018). ISSN: 00028711. DOI: 10.4050/JAHS.63.022002.

[3] Manikandan Ramasamy et al. “Data-driven optimal basis clustering to characterize cycle-to-cycle variations in dynamic stall measurements”. In: *The Vertical Flight Society - Forum 75: The Future of Vertical Flight - Proceedings of the 75th Annual Forum and Technology Display* (2019). DOI: 10.4050/F-0075-2019-14534.

[4] Prandtl L. “Über flüssigkeitsbewegung bei sehr kleiner reibung”. In: (1904).

[5] Osborne Reynolds. “An experimental investigation of the circumstances which determine whether the motion of water shall be direct or sinuous, and of the law of resistance in parallel channels”. In: *Philosophical Transactions of the Royal Society of London* 174 (Dec. 1883), pp. 935–982. ISSN: 0261-0523. DOI: 10.1098/rstl.1883.0029.

[6] Hermann Schlichting and Klaus Gersten. “Fundamentals of boundary layer theory”. In: *Boundary-Layer Theory* (2017), pp. 29–49. DOI: 10.1007/978-3-662-52919-5.

[7] John D. Anderson and Mary L. Bowden. *Introduction to flight*. McGraw Hill. ISBN: 1260226743.

[8] Julien Weiss, Abdelouahab Mohammed-Taifour, and Quentin Schwaab. “Unsteady behavior of a pressure-induced turbulent separation bubble”. In: *AIAA Journal* 53.9 (Apr. 2015), pp. 2634–2645. ISSN: 00011452. DOI: 10.2514/1.J053778.

[9] Elena Vagnoni. “The reaction turbines used in PHES units and related problems”. In: *Encyclopedia of Energy Storage: Volume 1-4* 1-4 (Jan. 2022), pp. 123–135. DOI: 10.1016/B978-0-12-819723-3.00140-2.

[10] Paul K. Chang. “Characteristics of separated flows”. In: *Separation of Flow* (Jan. 1970), pp. 272–335. DOI: 10.1016/B978-0-08-013441-3.50011-3.

[11] Snorri Gudmundsson. “General aviation aircraft design: applied methods and procedures”. In: *General Aviation Aircraft Design: Applied Methods and Procedures* (2013), pp. 1–1034. DOI: 10.1016/C2011-0-06824-2.

[12] Laura M Hudy, Ahmed M Naguib, and William M Humphreys. “Wall-pressure-array measurements beneath a separating/reattaching flow region”. In: (2003). DOI: 10.1063/1.1540633.

[13] Masaru Kiya and Kyuro Sasaki. “Structure of a turbulent separation bubble”. In: *Journal of Fluid Mechanics* 137 (1983), pp. 83–113. ISSN: 1469-7645. DOI: 10.1017/S002211208300230X.

[14] Zhiyin Yang and Peter R. Voke. “Large-eddy simulation of boundary-layer separation and transition at a change of surface curvature”. In: *Journal of Fluid Mechanics* 439 (July 2001), pp. 305–333. ISSN: 1469-7645. DOI: 10.1017/S0022112001004633.

[15] N. J. Cherry, R. Hillier, and M. E. Latour. “Unsteady measurements in a separated and reattaching flow”. In: *Journal of Fluid Mechanics* 144 (1984), pp. 13–46. ISSN: 1469-7645. DOI: 10.1017/S002211208400149X.

[16] John K. Eaton and James P. Johnston. “Low frequency unsteadiness of a reattaching turbulent shear layer”. In: *Turbulent Shear Flows 3* (1982), pp. 162–170.

[17] Masaru Kiya and Kyuro Sasaki. “Structure of large-scale vortices and unsteady reverse flow in the reattaching zone of a turbulent separation bubble”. In: *Journal of Fluid Mechanics* 154 (1985), pp. 463–491. ISSN: 1469-7645. DOI: 10.1017/S0022112085001628.

[18] L. W. Sigurdson. “The structure and control of a turbulent reattaching flow”. In: *Journal of Fluid Mechanics* 298 (1995), pp. 139–165. ISSN: 1469-7645. DOI: 10.1017/S0022112095003259.

[19] Daehyun Wee et al. “Self-sustained oscillations and vortex shedding in backward-facing step flows: Simulation and linear instability analysis”. In: *Physics of Fluids* 16.9 (Sept. 2004), pp. 3361–3373. ISSN: 1070-6631. DOI: 10.1063/1.1773091.

[20] Laura M Hudy, Ahmed Naguib, and William M Humphreys. “Stochastic estimation of a separated-flow field using wall-pressure-array measurements”. In: *Physics of Fluids* 19 (2007), p. 24103. DOI: 10.1063/1.2472507.

[21] W. Sheng, R. A.Mc D. Galbraith, and F. N. Coton. “A new stall-onset criterion for low speed dynamic-stall”. In: *Journal of Solar Energy Engineering* 128.4 (Nov. 2006), pp. 461–471. ISSN: 0199-6231. DOI: 10.1115/1.2346703.

[22] Karen Mulleners and Markus Raffel. “The onset of dynamic stall revisited”. In: *Experiments in Fluids* 52.3 (Mar. 2012), pp. 779–793. ISSN: 07234864. DOI: 10.1007/S00348-011-1118-Y.

[23] Vallorie J. Peridier, F. T. Smith, and J. D.A. Walker. “Vortex-induced boundary-layer separation. Part 1. The unsteady limit problem of Reynolds number to infinity”. In: *Journal of Fluid Mechanics* 232 (1991), pp. 99–131. ISSN: 1469-7645. DOI: 10.1017/S0022112091003646.

[24] Aleksandr V. Obabko and Kevin W. Cassel. “Detachment of the dynamic-stall vortex above a moving surface”. In: *https://doi.org/10.2514/2.1858* 40.9 (May 2012), pp. 1811–1822. ISSN: 00011452. DOI: 10.2514/2.1858.

[25] W. J. McCroskey and S. L. Pucci. “Viscous-inviscid interaction on oscillating airfoils in subsonic flow”. In: *https://doi.org/10.2514/3.51063* 20.2 (May 1982), pp. 167–174. ISSN: 00011452. DOI: 10.2514/3.51063.

[26] Tanner Harms, Pourya Nikoueeyan, and Jonathan Naughton. “Experimental evaluation of the cycle-to-cycle variation of dynamic stall on the SC1094R8 airfoil”. In: *AIAA Aerospace Sciences Meeting, 2018* (2018). DOI: 10.2514/6.2018-1267.

[27] Franklin O. Carta. “An analysis of the stall flutter instability of helicopter rotor blades”. In: *Journal of the American Helicopter Society* 12.4 (Sept. 2019), pp. 1–18. ISSN: 2161-6027. DOI: 10.4050/JAHS.12.4.1.

[28] J. G. Holierhoek et al. “Comparing different dynamic stall models”. In: *Wind Energy* 16.1 (2013), pp. 139–158. ISSN: 10991824. DOI: 10.1002/WE.548.

[29] Khanh Nguyen. “Evaluation of dynamic stall models with UH-60A airloads flight test data”. In: (1998).

[30] Montgomery Douglas C and George C. Runger. *Applied statistics and probability for engineers*. 6th. 2014, p. 813. ISBN: 9781118539712.

[31] Manikandan Ramasamy et al. *Measured characteristics of cycle-to-cycle variations in dynamic stall*. Jan. 2016.

[32] C. B. Merz et al. “Spanwise differences in static and dynamic stall on a pitching rotor blade tip model”. In: *Journal of the American Helicopter Society* 62.1 (Jan. 2017). ISSN: 00028711. DOI: 10.4050/JAHS.62.012002.

[33] Abigale Snortland et al. “Cycle-to-cycle variations in cross-flow turbine performance and flow fields”. In: (Feb. 2023). DOI: 10.48550/arXiv.2302.03218.

[34] P. Wernert et al. “Demonstration by PIV of the non-reproducibility of the flow field around an airfoil pitching under deep dynamic stall conditions and consequences thereof”. In: *Aerospace Science and Technology* 1.2 (Feb. 1997), pp. 125–135. ISSN: 1270-9638. DOI: 10.1016/S1270-9638(97)90042-0.

[35] Fulvio Scarano and Andrea Sciacchitano. *AE4180 2022 Flow Measurement Techniques: PIV*. Delft, 2022.

[36] Markus Raffel et al. *Particle Image Velocimetry*. Cham: Springer International Publishing, 2018. ISBN: 978-3-319-68851-0. DOI: 10.1007/978-3-319-68852-7.

[37] F. Durst et al. “Principles and practice of laser-Doppler anemometry”. In: *STIA* 76 (1976), p. 47019.

[38] Fulvio Scarano et al. “On the use of helium-filled soap bubbles for large-scale tomographic PIV in wind tunnel experiments”. In: *Experiments in Fluids* 56.2 (Feb. 2015), pp. 1–12. ISSN: 14321114. DOI: 10.1007/S00348-015-1909-7.

[39] Rainer Hain, Christian J. Kähler, and Cam Tropea. “Comparison of CCD, CMOS and intensified cameras”. In: *Experiments in Fluids* 42.3 (Mar. 2007), pp. 403–411. ISSN: 07234864. DOI: 10.1007/S00348-006-0247-1.

[40] Mohammed El-Adawy et al. “Stereoscopic particle image velocimetry for engine flow measurements: Principles and applications”. In: *Alexandria Engineering Journal* 60.3 (June 2021), pp. 3327–3344. ISSN: 11100168. DOI: 10.1016/J.AEJ.2021.01.060.

[41] Photron. *Photron Technical Datasheet Mini AX*. Tech. rep. URL: https://photron.com/wp-content/uploads/2015/11/Mini-AX-REV16.9.29.pdf.

[42] Daniel Schanz, Sebastian Gesemann, and Andreas Schröder. “Shake-The-Box: Lagrangian particle tracking at high particle image densities”. In: *Experiments in Fluids* 57.5 (May 2016), pp. 1–27. ISSN: 07234864. DOI: 10.1007/S00348-016-2157-1.

[43] Norbert Wiener. “Extrapolation, interpolation, and smoothing of stationary time series”. In: *Extrapolation, Interpolation, and Smoothing of Stationary Time Series* (Aug. 1949). DOI: 10.7551/MITPRESS/2946.001.0001.

[44] Bernhard Wieneke. “Iterative reconstruction of volumetric particle distribution”. In: *Measurement Science and Technology* 24.2 (Dec. 2012), p. 024008. ISSN: 0957-0233. DOI: 10.1088/0957-0233/24/2/024008.

[45] Floris Blok. *W-Tunnel AeroWiki*. Tech. rep. Delft: Delft University of Technology, Nov. 2023.

[46] Zaber. *Zaber X-RSB120AT-E08 Datasheet*. Tech. rep. Vancouver: Zaber. URL: https://www.zaber.comproducts/rotary-stages/X-RSB-E.

[47] Gordon J Leishman. *Principles of helicopter aerodynamics, 2nd Ed.* The Vertical Flight Society, 2006. Chap. 6. ISBN: 978-0-521-85860-1.

[48] Philippe Wernert et al. “Experimental and numerical investigations of dynamic stall on a pitching airfoil”. In: *https://doi.org/10.2514/3.13177* 34.5 (May 2012), pp. 982–989. ISSN: 00011452. DOI: 10.2514/3.13177.

[49] LaVision. *DaVis 10.2 Software. Product Manual.* Nov. 2022.

[50] J. C. R. Hunt, A. A. Wray, and P. Moin. “Eddies, streams, and convergence zones in turbulent flows”. In: *Studying Turbulence Using Numerical Simulation Databases, 2. Proceedings of the 1988 Summer Program* (1988).

[51] A J Banko and D J K Eaton. “A frame-invariant definition of the Q-criterion”. In: (2019).

[52] Z. I. Botev, J. F. Grotowski, and D. P. Kroese. “Kernel density estimation via diffusion”. In: *https://doi.org/10.1214/10-AOS799* 38.5 (Oct. 2010), pp. 2916–2957. ISSN: 0090-5364. DOI: 10.1214/10-AOS799.

A. Zaber Stage Control Script

```
import time

import numpy as np
from zaber_motion import Units, Library
from zaber_motion.ascii import Connection
from zaber_motion.gcode import axis_definition



Library.enable_device_db_store()


with Connection.open_serial_port("COM7") as connection:  # confirm that this is the right serial port
    device_list = connection.detect_devices()

    print("Found {} devices".format(len(device_list)))

    device = device_list[0]

    axis = device.get_axis(1)

    microstep_size = 0.005625  # [deg]

    Uinf = 5  # [m/s]
    chord = 0.1  # [m]
    angle_home = 268  # [deg]
    angle_mean =15   # [deg]

    # angle_input_home = angle_home / microstep_size
    # axis.move_absolute(angle_input_home)

    # Sinusoidal motion parameters
    max_angle_amplitude = 0  # [deg] needs to be half the angle of the max desired
    frequency = 1  # [Hz]
    oscillation_centre = angle_home + angle_mean #+ max_angle_amplitude  # [deg]
    numberPeriods = 1

    # Calculations for sin function inputs  variables
    amplitude_input = round(max_angle_amplitude / microstep_size)
    oscillation_centre_input = round(oscillation_centre / microstep_size)
    period = (1 / frequency) * 1000  # period in milliseconds

    axis.move_absolute(oscillation_centre_input - amplitude_input)

    cmd = f"move sin {str(amplitude_input)} {str(period)} {str(numberPeriods)}"
    # example: cmd = "move sin 5000 3000 5"
    print(cmd)
    axis.generic_command(cmd)
```